UNIVERSIDADE ESTADUAL DE CAMPINAS
Faculdade de Engenharia Elétrica e de Computação

Jesus Flores Huaman

Modeling and Dynamic Analysis of Microgrid using Typhoon HIL, Case Study : CAMPUSGRID

Modelagem e Análise Dinâmica de Microrrede usando Typhoon HIL, Estudo de Caso: CAMPUSGRID.

Campinas

2022

Jesus Flores Huaman

Modeling and Dynamic Analysis of Microgrid using Typhoon HIL, Case Study : CAMPUSGRID

Modelagem e Análise Dinâmica de Microrrede usando Typhoon HIL, Estudo de Caso: CAMPUSGRID.

Dissertation presented to the School of Electrical and Computer Engineering of the University of Campinas in partial fulfillment of the requirements for the degree of Master in Electric Engineering in the area of Electrical Energy.

Dissertação apresentada à Faculdade de Engenharia Elétrica e de Computação da Universidade Estadual de Campinas como parte dos requisitos exigidos para a obtenção do título de Mestre em Engenharia Elétrica, na área de Energia Elétrica

Supervisor: Prof. Dr. Daniel Dotta

Este exemplar corresponde à versão final da tese defendida pelo aluno Jesus Flores Huaman, e orientada pelo Prof. Dr. Daniel Dotta.

Campinas

2022

Ficha catalográfica
Universidade Estadual de Campinas
Biblioteca da Área de Engenharia e Arquitetura
Rose Meire da Silva - CRB 8/5974

F663m Flores Huaman, Jesus, 1993-
Modeling and dynamic analysis of microgrid using Typhoon HIL, case study: CAMPUSGRID / Jesus Flores Huaman. – Campinas, SP : [s.n.], 2022.

Orientador: Daniel Dotta.
Dissertação (mestrado) – Universidade Estadual de Campinas, Faculdade de Engenharia Elétrica e de Computação.

1. Modelagem e simulação. 2. Eletrônica de potência. 3. Geração distribuída de eletricidade. 4. Sistemas de energia elétrica - Estabilidade. I. Dotta, Daniel, 1978-. II. Universidade Estadual de Campinas. Faculdade de Engenharia Elétrica e de Computação. III. Título.

Informações Complementares

Título em outro idioma: Modelagem e análise dinâmica de microrrede usando Typhoon HIL, estudo de caso: CAMPUSGRID
Palavras-chave em inglês:
Modeling and simulation
Power electronics
Distributed electricity generation
Electric power systems - Stability
Área de concentração: Energia Elétrica
Titulação: Mestre em Engenharia Elétrica
Banca examinadora:
Daniel Dotta [Orientador]
Reinaldo Tonkoski Junior
Silvangela Lilian da Silva Lima Barcelos.
Data de defesa: 01-09-2022
Programa de Pós-Graduação: Engenharia Elétrica

Identificação e informações acadêmicas do(a) aluno(a)
- ORCID do autor: https://orcid.org/0000-0001-9021-2661
- Currículo Lattes do autor: http://lattes.cnpq.br/9684066097152182

COMISSÃO JULGADORA - TESE DE MESTRADO

Candidato(a): Jesus Flores Huaman RA: 264534
Data de defensa: 01 de Setembro de 2022
Titulo da Dissertação: "Modeling and Dynamic Analysis of Microgrid using Typhoon HIL, Case Study: CAMPUSGRID."

"Modelagem e Análise Dinâmica de Microrrede usando Typhoon HIL, Estudo de Caso: CAMPUSGRID."

Prof. Dr. Daniel Dotta (Presidente)
Profa. Dra. Silvangela Lilian da Silva Barcelos
Prof. Dr. Reinaldo Tonkoski Junior

A Ata de Defesa, com as respectivas assinaturas dos membros da Comissão Julgadora, encontra-se no SIGA (Sistema de Fluxo de Dissertação/Tese) e na Secretaria de Pós-Graduação da Faculdade de Engenharia Elétrica e de Computação.

... I dedicate my thesis with all my heart to my mother, because without her I would not have succeeded. Your blessing daily throughout my life protects me and leads me on the path of good. That's why I give you my work as an offering for your patience and love, my mother, I love you...(Higidia Huaman Centeno)

Acknowledgements

The conclusion of this master's degree is another important milestone in my life and for this reason, I want to thank the people who contributed to the completion of this work.

First of all, I thank God for giving me patience, wisdom, and perseverance during this journey. To my parents Higidia and Cristóbal for supporting me in this process, especially to my mother for the encouragement and effort she made to provide me with studies and conditions that she could not access. To my brothers for their love, support, and constant advice.

I would like to thank my advisor Dr. Daniel Dotta for the opportunity to allow me to be his master's student, and for his constant support and help in the process of my dissertation.

I would like to thank my friends from the FEEC LE19 laboratory, especially Dr. João Inácio Yutaka Ota for his constant help.

To my friend Dr. Elmer Lévano who helped me in moments of uncertainty in the master's process.

To my friend Leslie Vitorino, for her suggestions and unconditional support.

To my friend Ing. Pablo Apaza, who supported me and encouraged me to continue my studies abroad.

Finally, this work was carried out within the framework of the Research and Development Program for the Electricity Sector PD-00063-3058/2019 - PA3058: "MERGE - Microgrids for Efficient, Reliable and Greener Energy", regulated by the National Energy Agency. Electric power. Energy (ANEEL), in association with CPFL Energia (Local Electricity Distributor). This study was funded in part by the Brazilian research agency Coordination for the Improvement of Higher Education Personnel (CAPES), funding code 001, and the Fundação de Amparo à Pesquisa do Estado de São Paulo (FAPESP) with the numbers 2016/ 08645-9, 2018/07375-3 and 2019/10033-0.

" DON'T QUIT, SUFFER NOW, AND LIVE THE REST OF YOUR LIFE AS A CHAMPION "

(MUHAMMAD ALI)

Abstract

Electric Microgrid are seen as the new trend related to the future generation and consumption of electric energy. As they are mainly composed of renewable energy sources with high penetration of electronic power converters, high levels of automation and control are necessary to guarantee operational stability. Therefore, this work presents the dynamic modeling of the CAMPUSGRID, which corresponds to a microgrid that has been built at the State University of Campinas (UNICAMP), and presents the analysis of its respective dynamic behavior. Through these studies, using the Typhoon HIL Control Center simulation software, it can be concluded that the microgrid has operational flexibility, capable of keeping stable even after the occurrence of even such as : effects of renewable energy fluctuation, islanded mode transition, resynchronization and load variations.

Keywords: Electric microgrids, Distribution generation, Dynamic modeling, Control, Stability, CAMPUSGRID.

Resumo

As Microrredes elétricas são vistas como a nova tendência no que diz respeito a geração e consumo de energia elétrica do futuro. Por se tratarem de estruturas detentoras de fontes predominante renováveis com alta penetração de conversores eletrônicos de potência, altos níveis de controle e automação são necessários para a garantia da estabilidade operacional. Sendo assim, este trabalho apresenta a modelagem dinâmica da CAMPUSGRID, microrrede esta que vem sendo construída na Universidade Estadual de Campinas (UNICAMP), e também traz a respectiva análise do comportamento dinâmico da mesma. Através destes estudos, utilizando como software de simulação o Typhoon HIL Control Center, pode-se constatar que a microrrede apresenta flexibilidade operacional, capaz de se manter estável mesmo após a ocorrência de eventos como: efeitos da flutuação de energia renovável, transição ao modo ilhado, ressincronização e variações de carga.

Palavras-chaves: Microrredes elétricas, Geração distribuída, Modelagem dinâmica, Controle, Estabilidade, CAMPUSGRID.

List of Figures

List of Tables

List of abbreviations and acronyms

RES	Renewable Energy Source
DER	Distributed Energy Resources
GFL	Grid - Following
GFM	Grid - Forming
IBR	Inverter -based resource
IEEE	Institute of Electrical and Electronics Engineers
KV	kilo-volt
MVA	Mega-volt ampere
MVAr	Mega-volt ampere reactive
MW	Megawatt
PLL	Phase-locked loop
Hz	Hertz
POI	Point of interconnection
PV	Photovoltaic
BESS	Battery energy storage system
PCC	Point of Common Coupling

Contents

1 Introduction

1.1 Motivation

Facing the growing demand for electricity amid rising costs and environmental impacts related to the burning of fossil fuels, Renewable Energy Sources (RES) are being integrated into the main grid. The use of distributed generators that use RES integrated into the distribution networks is a promising solution to achieve a more sustainable electricity supply. The popularity of RES and the growing global demand for power has resulted in the emergence of microgrids formed by networks of distributed generation and consumption elements (CESPEDES; XING; SUN, 2011).

A microgrid is defined as a group of Distributed Energy Resources (DER), including RES and Battery Energy Storage System (BESS) and loads that operate locally as a single controllable entity (LASSETER, 2001), (OLIVARES et al., 2014a). In addition, they exist in various sizes, and setups and can be large and complex networks, with various generation resources and storage units that together serve a set of local loads (HIRSCH; PARAG; GUERRERO, 2018). Thus, the microgrid can operate connected to the main grid as an isolated mode depending on its functionality. The operation of the microgrid in mode connected to the main grid is through an interconnection point or common point of coupling (PCC) and should be capable of a seamless transition to island mode (KATIRAEI; IRAVANI; LEHN, 2005), (LISERRE et al., 2016). In both grid-connected and islanded/isolated modes of operation, microgrids should maintain a balance between generation and consumption, while meeting certain standards of reliability, and power quality. All controllable loads and distributed energy resources should be actively participated in keeping the system voltage and frequency stable and within acceptable ranges (KARIMI; NIKKHAJOEI; IRAVANI, 2007), (LISERRE et al., 2016). In grid-connected microgrids, islands can occur intentionally or unintentionally due to faults; in both cases, a microgrid must use adequate control techniques to continue its operation (KARIMI; YAZDANI; IRAVANI, 2008).

The balance between supply and demand is essential in microgrids and therefore, the intermittent nature of RES is particularly relevant in these systems (LI et al., 2016). The sizes of the microgrid systems are considerably smaller than conventional systems, thus the microgrid feeders are relatively short, with a lower ratio of reactance to resistance compared to conventional systems. Another consequence of the small size of the microgrid is greater uncertainty in the system, due to the reduced number of loads and the rapid and highly correlated variations of the available RES (OLIVARES et al., 2014a).

Another important feature of the microgrid is that it is made up of RES with an electronic interface and relatively small synchronous machines, consequently, the inertia in the microgrid is considerably lower compared to conventional power systems. In addition, one of the important concerns in microgrids in isolated operation is their relatively low short-circuit capacity, this can cause the inverter to shut down. Another features of microgrids are the loads that are typically unbalanced between the three phases (NASR-AZADANI et al., 2014), this can endanger the stability of the microgrid. To sum up, the aforementioned, important features of microgrids are the following: small system size, higher RES penetration, higher uncertainty, lower system inertia, higher R/X ratio of feeders, limited short-circuit capacity, and unbalanced loads.

In this context, the MERGE (Microgrids for Efficient, Reliable, and Greener Energy) research and development (R&D) project, which began in 2020, was proposed for the implementation of four microgrids with different purposes and features (LÓPEZ et al., 2020). Teams made up of researchers from the State University of Campinas (UNICAMP), The Federal University of Maranhao (UFMA), and the Advanced Institute of Technology and Innovation (IATI) are part of the project. Among them, CAMPUSGRID is a university microgrid within the State University of Campinas, Brazil, in which the installation of a Battery Energy Storage System, the extensive use of photovoltaic generation, and the implementation of an energy management system with extensive measurement of energy will be carried out demand and generation.

1.2 Literature Review

With the growing increase in distributed electricity generation promoted by residential and industrial consumers, a new scenario begins. This new situation is leading to the rupture of the vertical structure of the traditional electric systems. These systems are fundamentally based on synchronous machines, responsible for generating energy in a centralized and dispatchable way (SOULTANIS; PAPATHANASIOU; HATZIARGYRIOU, 2007). However, the integration of renewable energies in the grid has been increasing significantly, due to the reduction in the cost associated with photovoltaic and wind energy. This scenario implies the appearance of drawbacks since the general inertia decreases as the grid becomes weaker and less stable (TARRASÓ et al., 2019). In this context, there is great interest in reaching solutions capable of providing certain inertia, which makes the development of renewable energies compatible with the stability of the grid. As the levels of power electronics in the grid increase, problems related to large-scale integration into the grid, such as stability also increase. Due to this, various grid support functionalities have been added to such technologies, from a controller design perspective, inverter controls can be classified into grid following (GFL) and grid forming (GFM).

Several works have presented solutions that could improve a friendly interaction of RES, authors in (DU et al., 2020) proposed and discussed three-phase electromechanical models for inverters (GFM and GFL) that form and follow the grid. The inverter models proposed in (DU et al., 2020) were validated with electromechanical simulation, and simulated in a distribution system of 5252 isolated nodes, demonstrating the effectiveness of inverter models for the analysis of large-scale distributed systems.

GFM such as GFL will have a crucial role to play in frequency/voltage regulation and power-sharing maintenance through their support capabilities, in (DU et al., 2021),(SINGHAL; VU; DU, 2022), conducted studies of GFM-based microgrids and GFL inverters, demonstrating that phasor simulations can generate overly optimistic results and proposing a secondary control scheme to achieve frequency/voltage restoration.

BESS can be useful, particularly in a solution to the challenges faced by modern grids such as load switching, dynamic local voltage support, frequency smoothing, and grid contingency. Therefore, the increasing importance of BESS in microgrids, authors in (FARROKHABADI et al., 2017) investigate and compares the performance of the BESS model with different depths of detail. Considering the variety of BESS components, such as dc-dc and dc-ac converters. The average model is represented by a voltage source, an ideal DC source behind a voltage source converter, a buck/boost, and a bidirectional three-phase converter, with all models sharing the same control system and parameters. The models are developed and simulated in PSCAD. Through the simulation result, it is shown that the proposed model may show different performance, especially when the system is heavily loaded, highlighting the need for more accurate modeling under certain microgrid conditions.

1.3 Objectives

The objective of this research is to analyze the dynamic stability behavior of the CAMPUSGRID microgrid in islanded mode, with massive integration of inverters based on renewable sources. The detailed research objectives of this thesis are as follows:

- Evaluate the dynamic performance of the CAMPUSGRID microgrid in the face of different events such as transitions to isolated mode, re-synchronization, maximum load, and single-phase short circuit.
- To study the dynamic performance of the CAMPUSGRID microgrid, using BESS models with different depths of detail. i) DC-Link model ii) detailed model.
- To study the impact of maximum load on the dynamics of the DC link voltage of the detailed model of the BESS systems.

- Evaluate the grid following and grid forming controls of renewable generation sources based on inverters.

1.4 Contributions

The importance of BESS in microgrids is growing, and accurate modeling plays a key role in understanding their behavior. Therefore, in this work studies are carried out on the impact of the level of detail in the BESS model on stability and dynamic performance. In this context, this work compares the dynamic performance of CAMPUSGRID microgrids, using BESS models with different depths of detail. i) DC-link model and ii) detailed model. Thus, the main contributions of the work are the following:

- The impact of the detailed BESS model's DC Link voltage dynamics on the microgrid's stability was studied.
- The impact of the maximum load on the stability of microgrids was studied.

The models were developed at the Typhoon Hil Control Center, and their performance will be compared considering various voltage, current, and frequency variables at the point of common coupling (PCC).

1.5 Thesis Outline

This thesis is structured as follows:

In Chapter 1: Provides an overview and context of this research work and presents the objectives, contributions, and structure of the thesis.

In Chapter 2: This chapter defines microgrid concepts and identifies relevant issues related to stability. Likewise, the characteristics of microgrids are mentioned, such as a strong dependence on voltage and frequency, load imbalance, low inertia, and the intermittency of renewable generation. Finally, the control hierarchies are described along with analysis techniques and tools.

In Chapter 3: Microgrids are made up of inverter-based generators and distributed generators based on synchronous machines. Likewise, the elements that make up the microgrid can be divided into static and dynamic elements. In this context, this chapter presents the modeling and analysis of static and dynamic elements. Finally, the inverter is modeled in detail and is classified according to the mode of operation.

In Chapter 4: In this chapter, we present the implementation of a microgrid, called CAMPUSGRID. It will be a microgrid deployed at the State University of Campinas in

Brazil, which will serve a set of loads within it. The focus of this chapter is the location, the types of generation within the microgrid as well as their description and the specifications to carry out studies of them. Likewise, the computational tool for the implementation and simulation of this system is mentioned.

In Chapter 5: This chapter presents the results and simulations in the time domain, with the use of the computer program Typhoon HIL Control Center (Typhoon HIL, Typhoon HIL). These simulations aim to (i) verify the performance of the models proposed in the work, (BESS simplified DC Link) and (BESS detail model), and (ii) verify the dynamic behavior of the microgrid before, during, and after the islanded mode. Finally, simulations of six cases are performed:

- Case 1: Transition of the microgrid to islanded mode
- Case 2: Resynchronization.
- Case 3: Loss of generation in islanded mode.
- Case 4: Maximum load test in islanded mode.
- Case 5: Loss of BESS system in islanded mode.
- Case 6: Inverter behavior during a phase A to ground fault.

In Chapter 6: This chapter presents the conclusions and recommendation for futures works.

2 Microgrids

This chapter defines microgrid concepts and identifies relevant issues related to stability. Likewise, the characteristics of microgrids are mentioned, such as a strong dependence on voltage and frequency, load imbalance, low inertia, and the intermittency of renewable generation. Finally, the control hierarchies are described, as well as analysis techniques and tools.

2.1 Introduction

The conventional electric power system has dispatchable centralized generation, one-way power flow, and passive distribution, as shown in Figure 2.1. In these systems, large synchronous machines are responsible for generating power, these systems are robust in frequency and voltage, and they provide inertial rotation, which is indicative of the kinetic energy stored in the machine's rotors, which serve as a buffer in transients. The dynamics of these systems have been extensively studied and they can be distinguished between fast dynamics and slow dynamics. However, the dynamics of the conventional electrical power system were extremely slow because the inertia of synchronous machines dominated them and, at the same time, had an inherent self-synchronizing characteristic.

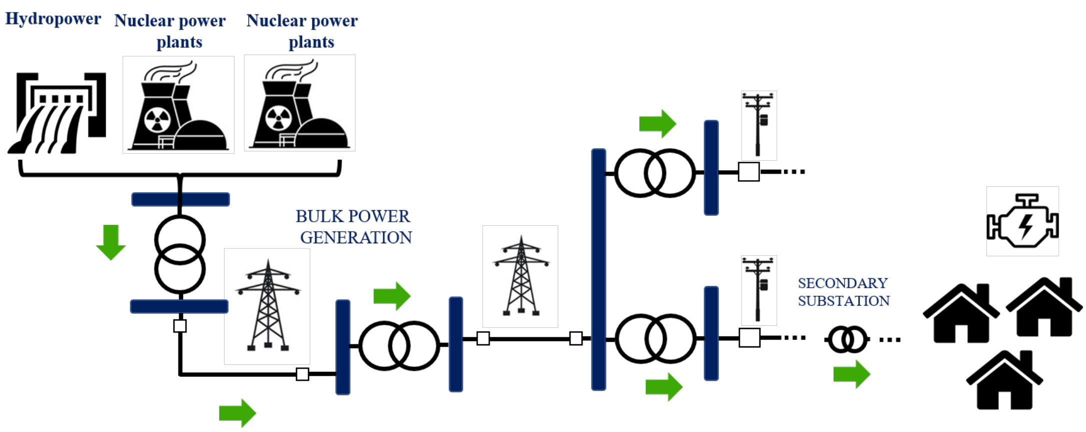

Figure 2.1 – Basic schematic of an electrical system

Likewise, due to the transition targets towards sustainable economies in different regions of the world, the large-scale incorporation of generation sources based on renewable energies (solar, wind...), in which new technologies based on power electronics, are increasingly incorporated into transition grids (GONZALEZ-LONGATT; RUEDA, 2014). The overcrowding of RES and the ever-increasing demand for energy have given rise to the appearance of microgrids made up of a group of DER's and loads with the ability to operate both in island mode and grid-connected mode and seamlessly isolate from the utility grid with little or no interruption to loads. However, emerging microgrids are expected to operate in isolation when the concessionaire's grid voltage source is lost due to events such as extreme weather and natural disasters.

Figure 2.2 shows a generic microgrid configuration, where the system is connected to the grid through a switch, or PCC, and consists of common components such as loads, and various dispatchable and non-dispatchable DER's. These systems can seamlessly transition to islanded mode, combined with its black starting capability, increasing the resilience of distribution systems in times of emergencies and blackouts (FARROKHABADI et al., 2020). Likewise, the dynamic of a microgrid is different than those of a conventional power system, due to the features it provides, the feeders are relatively short and operate at medium voltage levels, and they have strong mathematical relationships between voltages, angles, active power, and reactive power. In addition, the small size of the microgrid, the reduced number of loads, and the integration of RES based on inverters cause greater uncertainty in the system (FARROKHABADI et al., 2020).

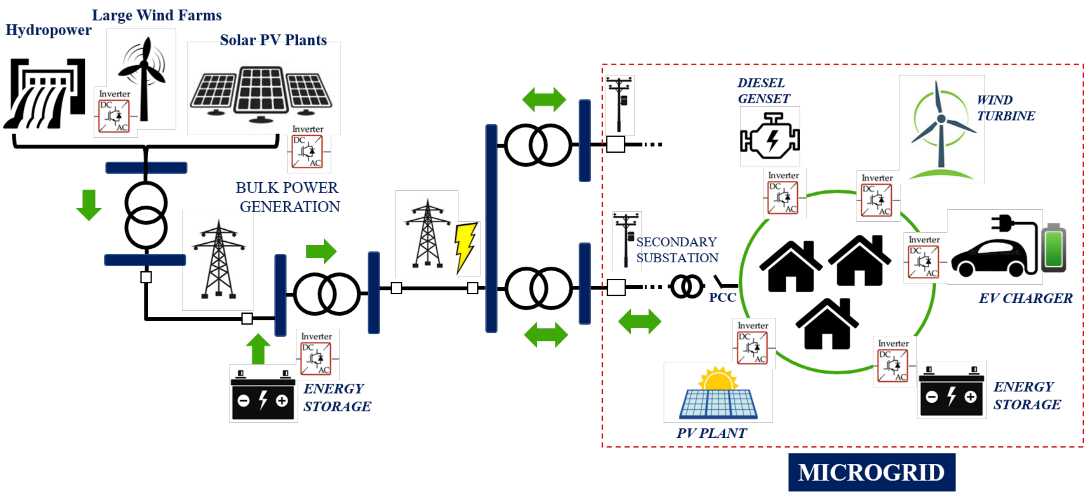

Figure 2.2 – Typical configuration of a Microgrid

The variable nature of RES is particularly relevant in these systems due electrical power is supplied with the electronic interface, and the complications associated with control coordination, and relatively small synchronous machines, propose stability challenges due to low inertia, and relatively low short-circuit capacity, which can lead to inverter shut down (MEEGAHAPOLA, 2018).

To sum up, microgrids present stability challenges that will be described in section 2.5. Also, the most important differences compared to conventional power systems are the: smaller system size, higher RES penetration, lower system inertia, higher uncertainty, limited short-circuit capacity, load unbalanced three-phase, and a higher ratio of resistance to the reactance of the feeders.

2.2 Microgrid Classifications

Microgrids can be mainly classified into three types according to their voltage characteristic and system architecture, 1) AC microgrids, 2) DC microgrids, and 3) AC/DC hybrid microgrids (AHMED et al., 2020). Likewise, microgrids can be classified according to the market segments, for example, 1) Utility microgrids, 2) Commercial and industrial microgrids, 3) Institutional microgrids, 4) Remote-area microgrids, and 5) Transportation microgrids.

2.2.1 AC microgrids

AC microgrids are the most conventional type of microgrid. AC microgrids are often connected to medium and low voltage distribution grids, with the ability to operate in islanded mode. This feature offers integration with minimal modifications to the grid, improving the flow of energy and reducing energy losses in the transmission lines(AHMED et al., 2020). However, they introduce new issues such as power quality, and reactive power shortage. Figure 2.3 shows an example of a typical AC microgrid configuration composed of a synchronous machine, BESS systems, and AC loads.

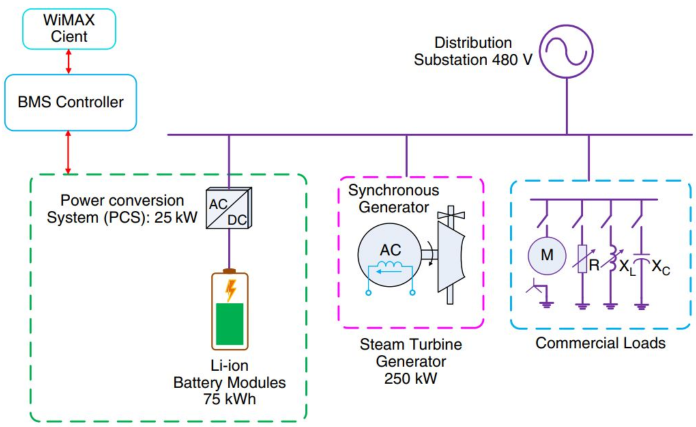

Figure 2.3 – Example of a AC microgrid configuration (FARHANGI; JOOS, 2019)

2.2.2 DC microgrids

The DC microgrid concept is the same as the conventional microgrid, but the energy is available in the DC form. Due to its characteristics of DC operation, DC microgrids have high efficiency and simplified control due to the absence of reactive power, and frequency controls. The integration of generation and storage sources (solar panels, and batteries) in a DC microgrid is easy to integrate (GARCéS, 2018). Likewise, loads such as household appliances could be adapted to operate in direct current. The use of DC/DC converters in the DC microgrid can operate as constant current or constant power, allowing for easy integration. Figure 2.4 shows a typical configuration of a DC microgrid with several storage devices, solar panels, and DC load consumption.

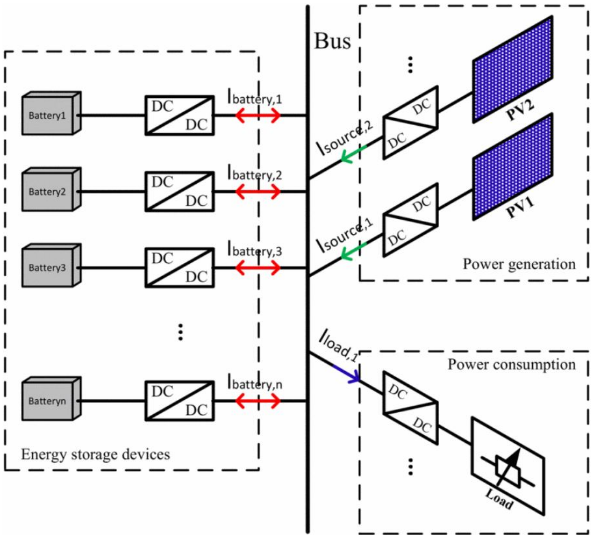

Figure 2.4 – Example of a DC microgrid configuration (LI et al., 2017)

2.2.3 AC/DC hybrid microgrids

Hybrid AC/DC microgrids combine the advantages of AC and DC microgrid architectures. These characteristics are combined in the same distribution grid, which facilitates the direct integration of distributed generation, BESS, photovoltaic systems, diesel generation, and loads based on AC and DC (UNAMUNO; BARRENA, 2015). Additionally, these features provide more efficient integration for RES units or electric vehicles with minimal network modifications. However, this architecture has several drawbacks that need to be further investigated, such as reliability, protection, and control complexity. Figure 2.5 shows a typical hybrid microgrid structure, where AC and DC grids are distinguished.

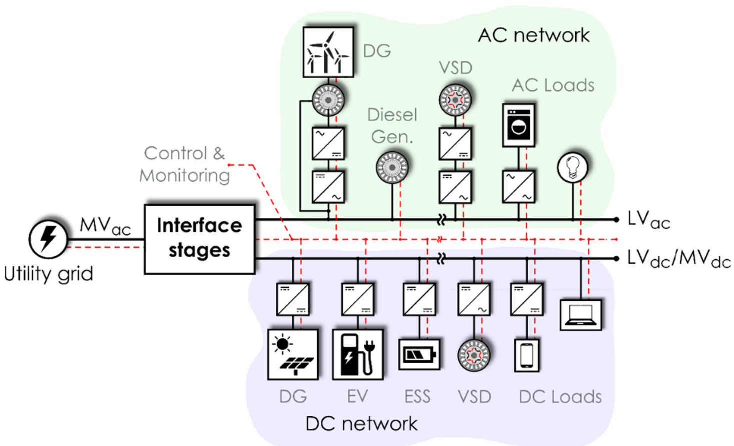

Figure 2.5 – Example of a AC/DC hybrid microgrid configuration (UNAMUNO; BARRENA, 2015).

2.3 IEEE Standards for Interconnection of DERs

Integrating a large number of inverter-based RES and the massification of microgrids in the conventional network is a matter of concern for the electricity system operators to maintain the stability and reliability of the system. The IEEE published standards for the interconnection of DERs into existing power systems. This IEEE 1547-2018 standard provides technical and interconnection test specifications and requirements for distributed power resources. Also, the criteria and conditions of the standard may influence the design and capabilities of the power interface and the communication interface. This Standard defines two categories (Category A and B) (IEEE. . . , 2018), related to reactive power capacity and voltage regulation performance requirements. Likewise, they are sub-categorized into Categories I, II, and III (IEEE. . . , 2018), related to the response to abnormal conditions of the electrical system.

The IEEE 1547 - 2018 standard analyzes seven operational aspects (AHMED et al., 2020), such as 1) voltage and reactive power control, 2) reactive power capability, 3) abnormal operating performance, 4) voltage disturbance ride-through requirements, 5) frequency tripping requirements, 6) islanding and protection aspect, and 7) power quality aspects. Table 2.1 specifies the minimum requirements that the DER must meet, in a stable and transient state for voltage, frequency, active power, reactive power, and time.

Table 2.1 – Minimum measurement and calculation accuracy requirements for manufacturers (IEEE. . . , 2018)

Time frame	**Steady-state measurements**		
Parameters	**Measurement accuracy**	**Measurement**	**Range**
Voltage, RMS	(+- 1% V_{nom})	10 cycles	0.5p.u to 1.2p.u
Frequency	10 mHz	60 cycles	50Hz to 66Hz
Active Power	+- 5% S_{rated}	10 cycles	0.2p.u < P < 1.0p.u
Reactive Power	+- 5% S_{rated}	10 cycles	0.2p.u < Q < 1.0p.u
Time	1% of measured duration	N/A	5s to 600s
Time frame	**Transient measurements**		
Parameters	**Measurement accuracy**	**Measurement**	**Range**
Voltage, RMS	(+- 2% V_{nom})	5 cycles	0.5p.u to 1.2p.u
Frequency	100 mHz	5 cycles	50Hz to 66Hz
Active Power	Not required	N/A	N/A
Reactive Power	Not required	N/A	N/A
Time	2 cycles	N/A	100ms < 5s

Also, during service entry, DER systems must not be energized until the voltage and frequency are within the specified ranges shown in Table 2.2. During service entry, DER's must be able to delay a minimum intentional time between 0s to 600s, until the voltage and frequency variables are within the acceptable ranges in the IEEE 1547-2018 standard.

Table 2.2 – Enter services criteria for DER (IEEE. . . , 2018)

Enter service criteria		**Default settings**	**Ranges of allowable settings**
Permit service		**Enabled**	**Enabled/Disabled**
Voltage	Minimum value	>= 0.917 p.u	0.88 p.u to 0.95p.u
Voltage	Maximum value	<= 1.05 p.u	1.05 p.u to 1.06 p.u
Frequency	Minimum value	>= 59.5 Hz	59.0 Hz to 59.9 Hz
Frequency	Maximum value	<= 60.1 Hz	60.1 Hz to 61.0 Hz

2.4 Hierarchical Control of AC Microgrids

The microgrid control system refers to the operational stability, optimal and reliable. These desired characteristics are mainly realized through microgrids that facilitate the integration of inverter-based RES, which can operate in both grid-connected and island modes. For stable and economically efficient operation, microgrids must have adequate control structures (OLIVARES et al., 2014b). In this context, the main functions of control structures are:

- Voltage and frequency regulation for grid-connected and islanded operating modes;
- Proper load sharing and RES coordination;
- Resynchronization with the main grid;
- Power flow control between the microgrid and the main grid;
- Optimizing the microgrid operating cost.

The distribution of loads and generation systems, electrical market prices, generation costs, and energy availability from RES are the main issues to take into account when determining the point optimal performance of a microgrid (ROCABERT et al., 2012). These requirements have different meanings and time scales, thus requiring a hierarchical control structure. These hierarchical control structures consist of three levels, primary, secondary and tertiary control shown in Figure 2.6. Primary control is the first level of the control hierarchy in charge of maintaining the voltage and frequency stability of the microgrid, it presents the fastest and most efficient response, and includes control

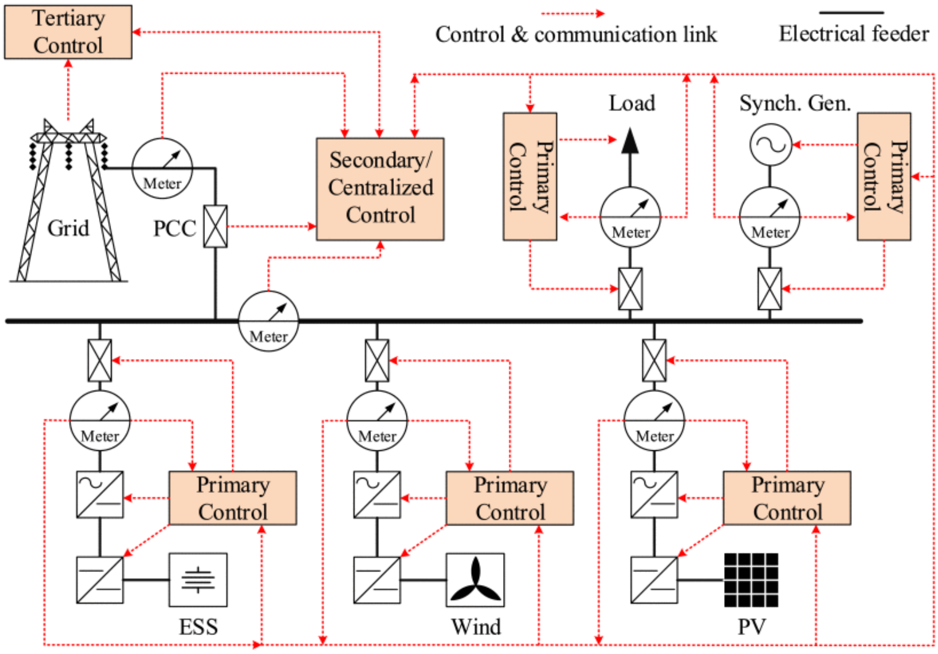

Figure 2.6 – Structure of Microgrids Control System (FARROKHABADI et al., 2020).

hardware, as well as voltage and current control loops. The secondary control compensates for voltage and frequency deviations caused by the operation of the primary control, and finally, the tertiary control manages the flow of energy between the microgrid and the conventional grid, facilitating an economically optimal operation (GUERRERO et al., 2011) (BIDRAM; DAVOUDI, 2012).

2.4.1 Primary Control

Primary control is the first level in the control hierarchy, known as local control or internal control, and it responds quickly. This control is based exclusively on local measurements and does not require communication (OLIVARES et al., 2014b). Likewise, the primary control is designed to keep the voltage and frequency stable, in the face of an event (load variation, generator output, climatic variation, island event) and properly distribute the active and reactive power, respectively. However, the primary control in synchronous generators is given by two control loops, an excitation system that regulates the voltage and a governor that regulates the frequency. In this context, grid-following inverters require reference angle and voltage signals so that power and current control loops can deliver power (GUERRERO et al., 2011).

2.4.2 Secondary Control

The secondary control is a mechanism for the permanent replacement of voltage and frequency deviations produced by the action of the primary control, this is due to the variable nature of the distributed generation units (OLIVARES et al., 2014b). However, this control hierarchy has a slower dynamic response than the main control and requires a communication infrastructure. The authors in (KHAYAT et al., 2020) classify secondary control into three main categories, centralized secondary control with communication infrastructure, distributed secondary control, and decentralized secondary control with infrastructure without communication. These categories of secondary control will not be addressed in this work.

2.4.3 Tertiary Control

Tertiary control is the highest level in the control hierarchy and establishes optimal, long-term setpoints based on power system requirements (OLIVARES et al., 2014b). It is in charge of coordinating the operation of multiple microgrids that interact with each other, to carry out voltage support and frequency regulation of the most critical microgrids (FARROKHABADI et al., 2020). Likewise, the coordination of reactive power management of several microgrids is achieved through tertiary control, which normally operates for several minutes.

2.5 Classification of Stability in Microgrids

A microgrid is defined as stable if, after being subjected to a disturbance, the state variables, voltage, frequency, active and reactive power, return to the initial operating conditions or to new states that satisfy the operating restrictions (MEEGAHAPOLA, 2018). Therefore, microgrids in the face of an isolated mode disturbance must have the capacity and be well designed to carry a small amount of load. However, the intentional firing of loads to maintain the stable operation of the system, during or after a disturbance, means that the microgrid is not fulfilling its objective, defining itself as an unstable system according to work (FARROKHABADI et al., 2020).

Microgrids are systems that are designed to supply power to small loads (for example, university centers, naval bases, hospitals, etc.). In the event of a disturbance that may occur in the conventional network, the microgrid must have the ability to operate in island mode. Therefore, disturbances correspond to any exogenous input and can be associated with load changes and component failures (MEEGAHAPOLA, 2018). In this context, microgrids are classified into small signal disturbances and large disturbances. Small disturbances can be classified so that a set of linearized equations can adequately represent the behavior of the system. Likewise, the main disturbances are short circuits, unplanned transitions from the grid-connected mode of operation to the isolated mode, and losses in the generation units are known as large disturbances. Therefore, these disturbances can be short-term or long-term phenomena that can generate undamped energy oscillations that can quickly grow beyond acceptable operating ranges.

Due to the strong coupling of microgrid variables, instability in these systems is manifested by fluctuations in all variables (voltage, frequency, active and reactive power). This strong coupling between system variables makes it quite difficult to classify instability phenomena as voltage or frequency instability. Given this difficulty, the authors in (MEEGAHAPOLA, 2018), (FARROKHABADI et al., 2020) perform the classification of stability in microgrids, which they divide into two categories, phenomena related to control systems and phenomena related to the balance of active and reactive power, these will be discussed in the following subsection. Figure 2.7 illustrates the classification of stability in microgrids.

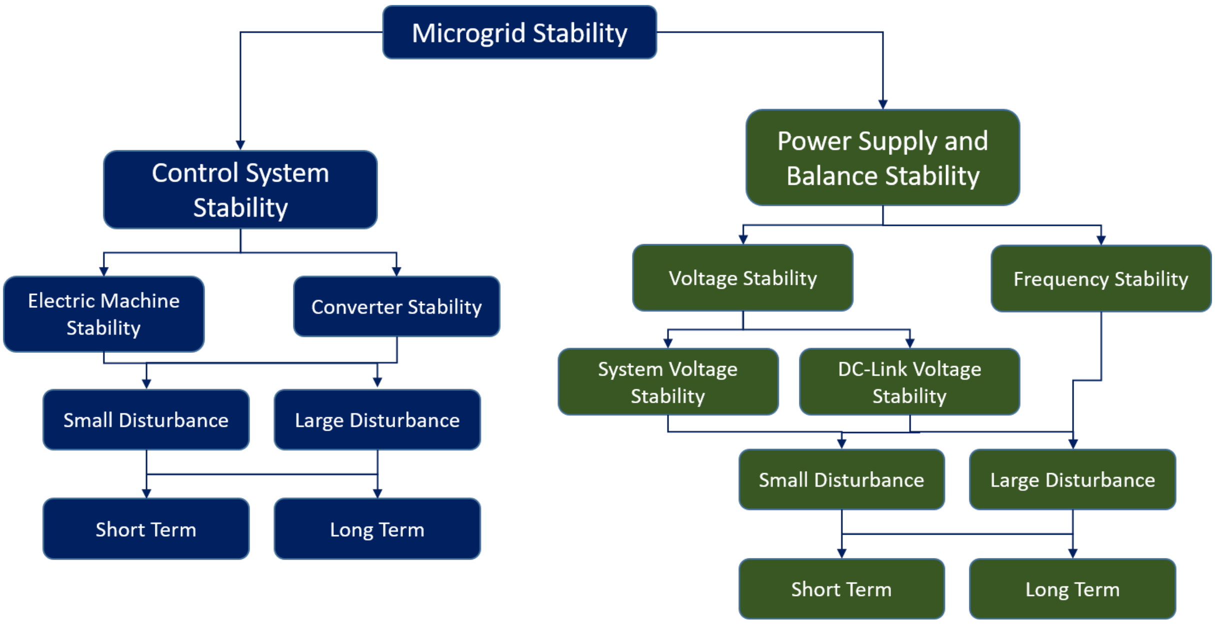

Figure 2.7 – Classification of Stability in microgrids (FARROKHABADI et al., 2020).

2.5.1 Power Supply and Balance Stability

Supply stability refers to the ability of the microgrid to maintain the energy balance between the RES generation sources and the load, in order to satisfy the operational requirements of the system (MEEGAHAPOLA, 2018). In this context, stability issues are associated with loss of generating units, violation of voltage and frequency limits, poor distribution of power among multiple renewable energy sources, and inadvertent tripping of loads. These types of problems cause voltage and frequency instability and are explained below.

2.5.1.1 Frequency Stability

Micrograds, due to their characteristics of low inertia and high integration of intermittent renewable energy, make frequency stability a major concern. Therefore, a disturbance (DER's generation output or load variations) can cause variations in the frequency at a high rate of change, endangering the stability of the system (MEEGAHAPOLA, 2018). However, due to the characteristic of the short feeders, the relation between R/X is high, this characteristic is reflected during voltage variations in the terminals of the DER's, where the demand of the system changes instantly. It is important to take voltage-frequency coupling into account for stability and frequency control analysis.

One of the causes of frequency instability in microgrids is the lack of generation reserve or overload in isolated microgrids, which drives the steady-state frequency out of operating ranges, activating low-frequency load trip relays. Likewise, low inertia combined with inadequate system response can result in a rapid drop in frequency, leading to a system blackout.

2.5.1.2 Voltage Stability

Feed-in distances in microgrids are relatively short, which is immediately reflected in relatively small voltage drops. An appropriate coordination of DER's voltage controllers is crucial. In fact, if not adequately coordinated, small differences in DER's voltages can lead to higher circulating reactive power flows, resulting in large voltage swings (SAO; LEHN, 2005). However, the DER's inverters are linked to the buck/boost converters through a capacitor to maintain the DC voltage (FARROKHABADI et al., 2020). Likewise, these devices are designed to supply a certain power. Therefore, in the event of an increase in demand close to the power limits of the DER's, as a result, undamped voltage waves may appear across the DC link capacitor, causing large fluctuations in the injection of active and reactive power.

Voltage instability can be classified as large disturbances, caused by sudden large changes in demand, the output of large loads, or RES sources. However, the large imbalance between microgrid phases and systems operating very close to their load limits can cause voltage instability. Likewise, they are classified according to the duration of the disturbance, short or long term. The short term due to poor coordination of FER control or rapid dynamic changes (MEEGAHAPOLA, 2018). Finally, long-term voltage instability is related to DER limits, which are gradually reached by a constant increase in demand.

2.5.2 Control System Stability

Control system stability problems can arise due to poor tuning of inverter controllers and poor design of LCL, and PLL filters. Poor PLL setting causes inverter output and shutdown (FARROKHABADI et al., 2020). These mentioned problems are explained below.

2.5.2.1 Electrical Machine Stability

Small synchronous machines are integrated into microgrids, for inertial support in isolated/island systems. This type of stability is related to poor tuning of the control loops of the exciters and speed regulators (FARROKHABADI et al., 2020), (NASR-AZADANI et al., 2014), as well as their poor design. In this context, in the event of faults such as short circuits or transitions of microgrid operating modes, the synchronous machines can slow down, reflected in a drop in frequency and voltage, accompanied by poor tuning of the controls, which would cause the generator to shut down and endanger the stability of the microgrid.

2.5.2.2 Converter Stability

The voltage and current control loops in the inverters are tightly coupled with each other. This can cause low or high-frequency oscillations caused by poor tuning of the drivers. Another cause of instability is poorly designed LCL power filters, which can trigger series and parallel resonances (MEEGAHAPOLA, 2018).

The presence of multiple inverters located in close proximity to each other can also lead to instability issues. The authors at (HE et al., 2013) show the results of inverter interaction problems that result in multiple resonance peaks. Finally, the PLLs are used for the synchronization of the follower and support inverters, the bad synchronization of these, can lead to the exit and finally to the shutdown of the inverter, losing the synchronism of the network or of a forming inverter, this is caused by a large disturbance, such as a large increase in load, the transition of operating modes of microgrids or RES generation losses.

2.5.3 Large vs Small Disturbance

Microgrids are subject to disturbances and are classified according to the magnitude as small or large disturbances, depending on the duration of time, they are called short-term or long-term phenomena (MEEGAHAPOLA, 2018). In this context, large disturbances are considered short circuits, planned or unplanned transitions of operating modes of the microgrid, and losses of generation units. These problems can be due to various reasons, such as poor power coordination between the multiple generation sources, poor control tuning, and their response time (ALABOUDY et al., 2012), which is vital to maintain the microgrid's stability.

Likewise, small disturbances in microgrids are considered a linearized set of equations that can adequately represent the system's behavior (WANG; BLAABJERG; WU, 2014). In this context, small disturbances are considered small load changes causing undamped oscillations, leading to the collapse of the microgrid or the activation of the disconnection of the inverters. Likewise, the poor coordination of multiple RES can generate undamped energy oscillations growing rapidly to unacceptable operating ranges in the short term (FARROKHABADI et al., 2020). These can be caused by poorly adjusted PLLs (Phase Locked Loop) and poorly designed LCL filters.

It is important to correctly identify the main causes of the problem of instability in microgrids, Tables 2.3 and 2.4 describe a summary of each type of instability and its causes.

Table 2.3 – Characteristic of control system stability

Category	**Control System Stability**	
Subcategory	Electric Machine Stability	Converter Stability
Root Cause	Poor controller tuning	Poor controller tuning, PLL bandwidth, PLL synchronization failure, harmonic instability.
Manifestation	Undamped oscillation, aperiodic voltage and / or frequency increase/decrease.	Undamped oscillations, low steady-state voltage, high-frequency oscillations.

Table 2.4 – Characteristic of power supply and balance stability

Category	**Power Supply and Balance Stability**	
Subcategory	Voltage Stability	Frequency Stability
Root Cause	DERs power limits, inadequate reactive power supply, poor reactive power sharing, dc-link capacitor.	DERs active power limits inadequate reactive power supply, poor reactive power sharing.
Manifestation	Low steady- state voltage, large power swings, high dc-link voltage ripples.	High rate of change f frequency, low steady-state frequency, large power and frequency swings.

2.6 Analysis Techniques and Tools

In this work, the analysis of stability in face of large disturbances in microgrids is focused and these can be carried out in three approaches according to the authors (FARROKHABADI et al., 2020), stability studies based on Lyapunov, simulations in the time domain, and hardware in the loop (HIL).

2.6.1 Lyapunov Techniques

Authors in (KABALAN; SINGH; NIEBUR, 2019), (ANDRADE et al., 2014) apply techniques in microgrids to provide information on transient stability. This method is advantageous for transient analyses, without the need to analytically solve the differential equations associated with the system. However, Lyapunov techniques present several challenges, finding the proper Lyapunov function is a major hurdle and requires many simplified assumptions (FARROKHABADI et al., 2020). These are limited to studies of balanced three-phase systems.

2.6.2 Time-Domain Simulations

Simulations in the time domain include major advantages compared to the Lyapunov technique; including greater precision and validity. However, power electronics simulations present a modeling challenge due to the wide variety of time constants, from a computational point of view the simulation of these highly nonlinear systems are intensive. In this context, there are EMT simulation tools such as (PSCAD, Pscad Documentation) to carry out studies of stability problems in microgrids, however, for studies of larger microgrids, this might not be feasible due to the complexity of the components and the computational load (FARROKHABADI et al., 2020).

2.6.3 Hardware-in-the-Loop Technique

Microgrid modeling presents challenges due to the presence of power electronics and the wide variety of time constants. In this context, Hardware in the loop (HIL) technology simulation tools provide an effective platform for the development and testing of highly complex embedded systems (Typhoon HIL, Typhoon HIL). However, correctly representing the high-frequency switching and circuit dynamics of power electronics-based schemes requires small simulation time steps. In the market there are two real-time simulators RTDS (RTDS Technologies, Hardware-in-the-loop testing for renewables) and Typhoon HIL (Typhoon HIL, Typhoon HIL), they are designed to achieve extremely small time steps, which allows the user to model the behavior of inverters in a wide frequency range in real-time. To reduce the risk of a microgrid implementation, the simulated network can be connected to real control hardware and performance can be improved prior to implementation.

2.7 Comments and Conclusions

This chapter reviews the definitions, analysis, and stability modeling of microgrids. For this reason, definitions of the stability problems of microgrids are presented, likewise, they were classified according to their causes. Due to their unique characteristics, microgrids present different stability issues than traditional power systems. Finally it is also mentioned about stability modeling and analysis tools. In the next chapter, the modeling of the elements that make up the microgrid is carried out.

3 Microgrid Elements and Modeling

Microgrids are made up of inverter-based generators and distributed generators based on synchronous machines. Likewise, the elements that make up the microgrid can be divided into static and dynamic elements. In this context, this chapter presents the modeling and analysis of static and dynamic elements. Finally, the inverter is modeled in detail and is classified according to the mode of operation.

3.1 Introduction

A typical microgrid is made up of various components and technologies, including small-capacity synchronous machines, inverter-based DERs, and various types of loads (MEEGAHAPOLA, 2018). Likewise, microgrids have the ability to operate in islanded as well as connected to the grid. In this context, the design, control, and analysis of microgrids require accurate models that adequately reflect their real performance, especially in stability studies (MEEGAHAPOLA, 2018). Therefore, the components of the microgrid can be divided into two categories: static elements and dynamic elements, which will be described below.

3.2 Static Elements

This section provides a discussion of the network and the loads which are static elements that make up the microgrid, providing details of its modeling, techniques, and tools used for stability studies.

3.2.1 Electrical Grid

Stability issues in microgrids, as well as dynamic performance, are considered different from conventional power systems. One of the characteristics of these systems are the feeders that are considered relatively short. In addition, these systems work at medium voltage levels, presenting a high R/X ratio and unbalance in the three phases (FARROKHABADI et al., 2020). In this context, the modeling of microgrids and feeders of distribution systems is different from the modeling of transmission lines of power systems. The model used in this work uses a model based on a grounded three-phase four-wire system, proposed by the authors in (RANJAN et al., 2004). Likewise, admittances are not considered in the model of microgrid feeders because they are short and operate at medium voltage levels.

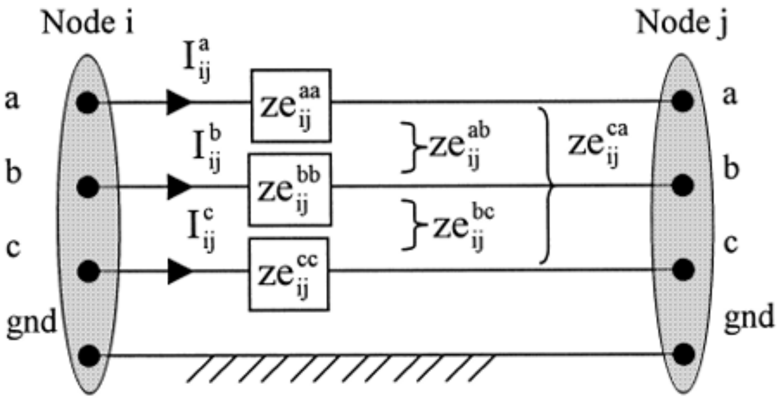

Figure 3.1 – Three-phase distribution feeder in a microgrid with grounded neutral (RANJAN et al., 2004)

Figure 3.1 shows the simple circuit model for a three-phase system with grounded neutral. Likewise, the currents in the three phases that cross the self-impedances and the mutual impedances between the conductors can be observed. In this context, the equations that relate the currents through the feeder of the nodes ij are shown. Using Kirchhoff's voltage law, we can write :

$$\begin{bmatrix} V_i^{ag} - V_j^{ag} \\ V_i^{bg} - V_j^{bg} \\ V_i^{cg} - V_j^{cg} \end{bmatrix} = \begin{bmatrix} Z_{ij}^{aa} & Z_{ij}^{ab} & Z_{ij}^{ac} \\ Z_{ij}^{ba} & Z_{ij}^{bb} & Z_{ij}^{bc} \\ Z_{ij}^{ca} & Z_{ij}^{cb} & Z_{ij}^{cc} \end{bmatrix} \cdot \begin{bmatrix} I_{ij}^{a} \\ I_{ij}^{b} \\ I_{ij}^{c} \end{bmatrix} = \begin{bmatrix} Z_{ij}^{abc} \end{bmatrix} \cdot \begin{bmatrix} I_{ij}^{a} \\ I_{ij}^{b} \\ I_{ij}^{c} \end{bmatrix} \tag{3.1}$$

where the values of the impedance elements of Eq.(3.1) are recalculated using Eq.(3.2)

$$Z_{ij}^{abc} = Ze_{ij}^{abc} - \frac{Ze_{ij}^{\phi n} . Ze_{ij}^{\phi a}}{Ze_{ij}^{nn}} \tag{3.2}$$

Eqs.(3.3), (3.4), and(3.5) describe each of the elements of Eq.(3.2).

$$\begin{bmatrix} Ze_{ij}^{abc} \end{bmatrix} = \begin{bmatrix} Z_{ij}^{aa} & Z_{ij}^{ab} & Z_{ij}^{ac} \\ Z_{ij}^{ba} & Z_{ij}^{bb} & Z_{ij}^{bc} \\ Z_{ij}^{ca} & Z_{ij}^{cb} & Z_{ij}^{cc} \end{bmatrix} \tag{3.3}$$

$$\begin{bmatrix} Ze_{ij}^{\phi n} \end{bmatrix} = \begin{bmatrix} Ze_{ij}^{an} \\ Ze_{ij}^{bn} \\ Ze_{ij}^{cn} \end{bmatrix} \tag{3.4}$$

$$\begin{bmatrix} Ze_{ij}^{n\phi} \end{bmatrix} = \begin{bmatrix} Ze_{ij}^{na} \\ Ze_{ij}^{nb} \\ Ze_{ij}^{nc} \end{bmatrix} \tag{3.5}$$

A single phase feeder is shown in Figure 3.2. It is represented by resistance and inductance in series. The current through the feeder of ij is shown in Eq. (3.6).

$$I_{ij}^{a} = \frac{V_i^a - V_j^a}{Ze_{ij}^{aa}} \tag{3.6}$$

The complex power flow from node i to node j in each phase ϕ is defined in Eq.(3.7).

$$P_{ij}^{\phi} - jQ_{ij}^{\phi} = V_i^{\phi^*} I_{ij}^{\phi} \tag{3.7}$$

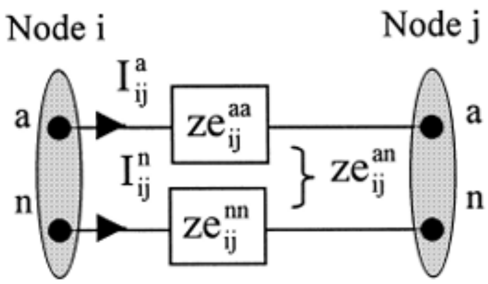

Figure 3.2 – Single phase line section (RANJAN et al., 2004)

3.2.2 Load

The three-phase load model is shown in Figure 3.3, this is used for modeling the microgrid. Likewise, the model may or may not be balanced. In this context, the values of the active P_{ij} and reactive powers Q_{ij} respectively in the three phases are considered, they can have different values or even zero. In fact, the two-phase or single-phase loads are modeled, setting the values of the apparent power S_{ij}^{*} to zero.

$$I_{ij}^{a} = \left[\frac{P_{ij}^{a} + jQ_{ij}^{a}}{V_j^a}\right]^{*} \tag{3.8}$$

$$I_{ij}^{b} = \left[\frac{P_{ij}^{b} + jQ_{ij}^{b}}{V_j^b}\right]^{*} \tag{3.9}$$

$$I_{ij}^{c} = \left[\frac{P_{ij}^{c} + jQ_{ij}^{c}}{V_j^c}\right]^{*} \tag{3.10}$$

The Eqs.(3.8), (3.9), and (3.10) provide a method to calculate the currents through the three phases between nodes ij. In fact, the energy fed to phase a between nodes ij is $V_i^a.(I_{ij}^a)^*$. Therefore active and reactive power losses in the three phases are written in Eqs.(3.11), (3.12), and (3.13) (RANJAN et al., 2004).

$$SL_{ij}^{a} = PL_{ij}^{a} + jQL_{ij}^{a} = V_i^a.I_{ij}^{a\,*} - V_j^a.(I_{ij}^a)^* \tag{3.11}$$

$$SL_{ij}^{b} = PL_{ij}^{b} + jQL_{ij}^{b} = V_i^b.I_{ij}^{b\,*} - V_j^b.(I_{ij}^b)^* \tag{3.12}$$

$$SL_{ij}^{c} = PL_{ij}^{c} + jQL_{ij}^{c} = V_i^c.I_{ij}^{c\,*} - V_j^c.(I_{ij}^c)^* \tag{3.13}$$

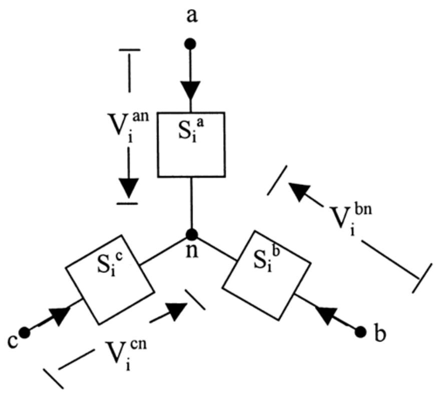

Figure 3.3 – Load model (RANJAN et al., 2004)

3.3 Dynamic Elements

This section provides a discussion of the inverters and synchronous machines known as dynamic elements that make up the microgrid, providing details of their modeling, techniques, and tools used for stability studies.

3.4 Gas Genset

The Gas Genset is modeled with a rotary synchronous machine and has two control loops to regulate the active and reactive power respectively. Therefore, the voltage is regulated through an automatic voltage regulator (AVR) that controls the field voltage v_f according to the reactive power or reference voltage setpoints, and the frequency is regulated by the regulator speed or governor. The control scheme is shown in Figure 3.4.

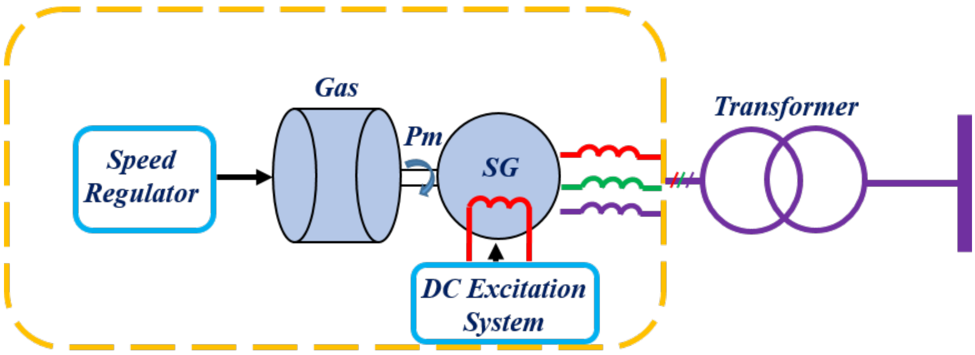

Figure 3.4 – Gas Genset

3.4.1 Three Phase Wound Rotor Synchronous Machine

The synchronous machine consists of two main components, the armature (stator) and the field windings (rotor). The armature windings are 120° apart, with uniform rotation of the magnetic field induced by the rotor and producing voltages shifted 120° in time (KUNDUR, 2017). Likewise, the rotor produces a magnetic field, being fed with direct current, and alternating voltages are induced in the armature windings. Therefore, for the production of constant torque, the stator and rotor fields must rotate at the same speed, which is known as synchronous speed (KUNDUR, 2017) .

3.4.1.1 Electrical sub-system model

The synchronous machine has as parameters inductances and resistances of the stator and rotor circuits, these parameters are deduced and explained in chapter 3 of (KUNDUR, 2017). It is common practice to use equivalent circuits that provide a visual description of the machine model. Likewise, these parameters are referred to as basic parameters and are identified by the elements of the equivalent circuit of the d and q axes, which are shown in Figure 3.5. The authors in (KUNDUR, 2017), (Typhoon HIL Documentation, Three Phase Synchronous Machine) show a model structure that is considered suitable for stability studies. This machine model is oriented to the structure and operation of salient poles. Table 3.1 shows the variables of the model of the electrical subsystem of the synchronous machine.

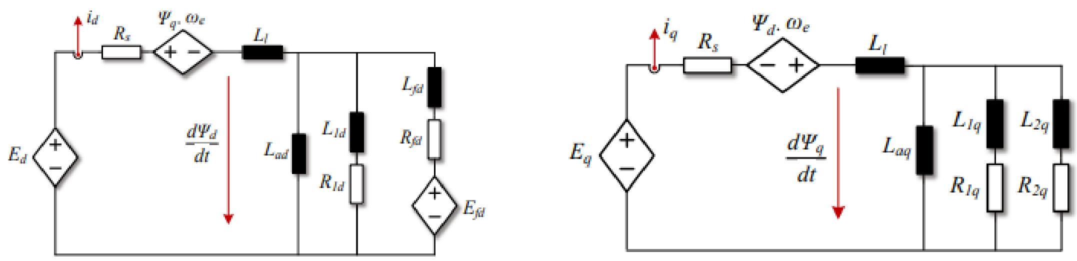

Figure 3.5 – Dq equivalent circuit (GKOUNTARAS, 2017).

3.4.1.2 Mechanical sub-system model

The equation of motion that describes the effect of the imbalance between the electromagnetic torque and the mechanical torque of the machine (KUNDUR, 2017) is shown in Eqs.(3.14), and (3.15). These equations are of importance in stability analysis. Likewise, T_e and T_l are positive for a generator and negative for a motor. The variables of the mechanical subsystem model are shown in Table 3.2.

$$\frac{d\omega_m}{dt} = \frac{1}{J_m}(T_e - T_l.b.\omega_m) \tag{3.14}$$

Table 3.1 – Dq equivalent parameters

Variable	**Description**
E_{dq}	Induced terminal voltage
ψ_{dq}	Flux linkage
f_d	Field winding
ω_e	Rotor angular velocity
L_l, R_s	Self inductance and resistance of stator winding
L_{adq}	Dq components of mutual inductante between stator and rotor windings
L_{1dq}, L_{2dq}	Self inductance of dq amortisseur circuits.
L_{fd}, R_{fd}	Self inductance and resistance of rotor circuit
L_{dq}	Dq-axis synchronous reactance.

$$\theta_m = \int \omega_w dt \tag{3.15}$$

Table 3.2 – Mechanical sub-system model variables

Symbol	**Description**
ω_m	Rotor mechanical speed
J_m	Combined rotor and load moment of inertia
T_e	Machine developed electromagnetic torque
T_l	Shaft mechanical load torque
b	Machine viscous friction coefficient
θ_m	Rotor mechanical angle.

3.4.2 Excitation System - IEEE DC4B

The excitation system of the Gas Genset used is IEEE DC4B, whose function is basically to provide direct current to the field winding. Likewise, it provides voltage and reactive power control loops, improving system stability (KUNDUR, 2017).

A block diagram of the DC4B driver is shown in Figure 3.6. This excitation system includes a proportional, integral, and differential (PID) voltage regulator and overexcitation and underexcitation limiters (Typhoon HIL Documentation, IEEE DC4B Exciter). The variables of the excitation system model are shown in Table 3.3

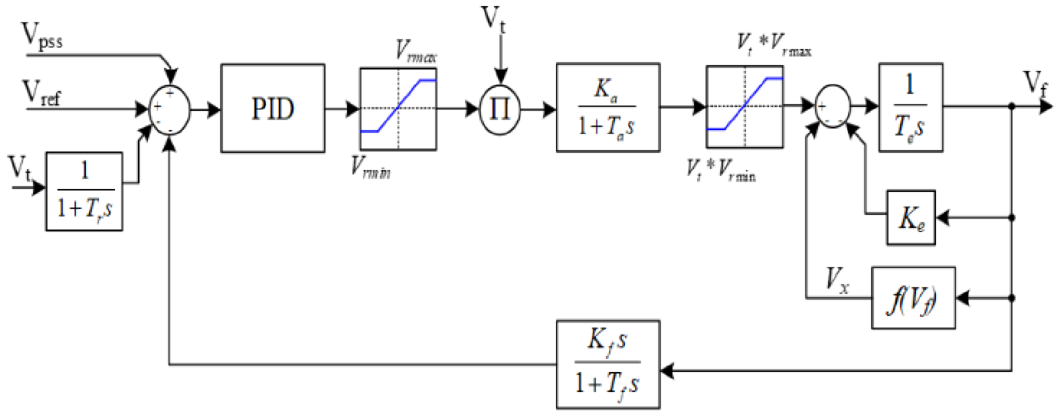

Figure 3.6 – Block diagram of the DC4B exciter

Table 3.3 – Component IEEE DC4B exciter properties

Symbol	**Description**
T_r	Time constant
K_p	Regulator proportional gain
K_i	Regulator integral gain
K_{deriv}	Regulator derivative gain
T_a	Major regulator time constant
V_{rmax}	Saturation upper limit
V_{rmin}	Saturation lower limit
T_e	Exciter time constant
K_e	Exciter gain
K_f	Stabilization feedback gain
T_f	Stabilization feedback time constant

3.4.3 Governor model

The speed governor is responsible for maintaining the frequency of a Gas Genset. Likewise, the regulation of frequency and active power is carried out through the regulation of the fuel injected into the Gas Genset, which is converted into mechanical energy through combustion (PODLESAK et al., 2019). Therefore, the mechanical energy generated by combustion causes the rotor to rotate at speed directly proportional to the frequency of the voltage (ALABOUDY et al., 2012). In this work, the DEGOV Woodward Diesel governor model was used, which has three main components that govern the dynamics of the governor system, the electric control box, the fuel control actuator, and the gas engine, these components are shown in Figure 3.7.

Table 3.4 shows the components of the Woodward Governor. These components affect the model's response, where T_4 and T_5 are fuel gate opening time constants, and K

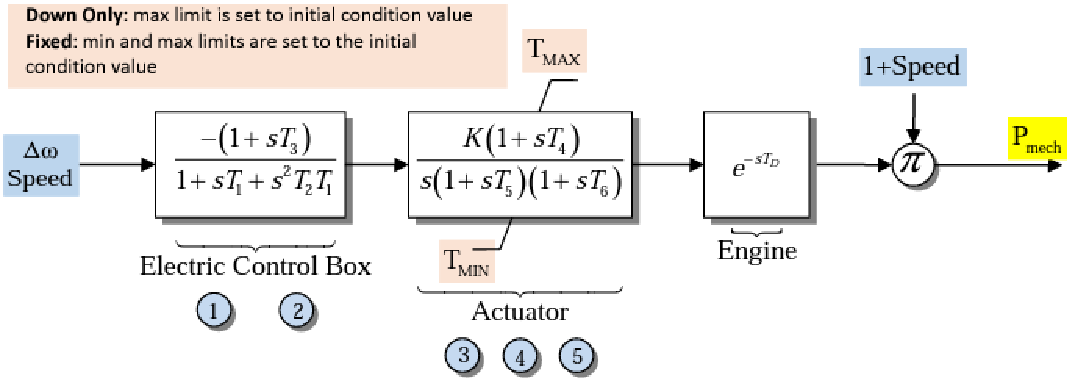

Figure 3.7 – Block diagram of Woodward Diesel Governor Model

the gain constant, alters the generator response.

Table 3.4 – Component of Woodward Diesel Governor

Symbol	Description
T_1, T_2, T_3	Electric control box time constant
K	Actuator gain
T_4, T_5, T_6	Actuator time constant
T_{MAX}	Maximum torque limit
T_{MIN}	Minimun torque limit
T_D	Engine time delay

3.5 Inverter Based Resources

The rapid evolution of energy systems is causing a shift from synchronous equipment to inverter-based resources (IBR), such as solar, wind, and battery storage systems. In this context, IBRs are currently being installed massively in the electric grid. As a result, IBRs do not inherently respond to disturbances in the grid, as synchronous machines do. This poses challenges and opportunities for a network that has historically been designed around synchronous generators (MIRAFZAL; ADIB, 2020). However, as the participation of IBRs continues to increase, there is a need for these systems to provide reliability support to the network. In this context, almost all IBRs currently implemented are grid following (GFL), these systems basically read the voltage and frequency of the grid and supply current, but as the number of synchronous machines decreases, the electric grid becomes more susceptible to the risk of instability. The need for new controls of advanced inverters grid forming (GFM), to maintain the stability of the system is of great importance.

Likewise, these GFM controls establish voltage and frequency, when there are no synchronous machines (generation 100% penetration of IBR). These GFM controls are relatively new and are still being researched and developed. In fact, along with advances in controls, requirements for IBR modeling and survey tools have also been advancing, with increasing demands for model accuracy, as well as computationally intensive, detailed simulation tools (MIRAFZAL; ADIB, 2020). In this context, it is essential to understand the properties and dynamic behavior of IBR. Furthermore, this is an area of active research in industry and academia, and GFM's are beginning to gain traction, with several pilot projects underway around the world. Next, a brief definition and comparison of the GFL and GFM controllers of the IBRs are made.

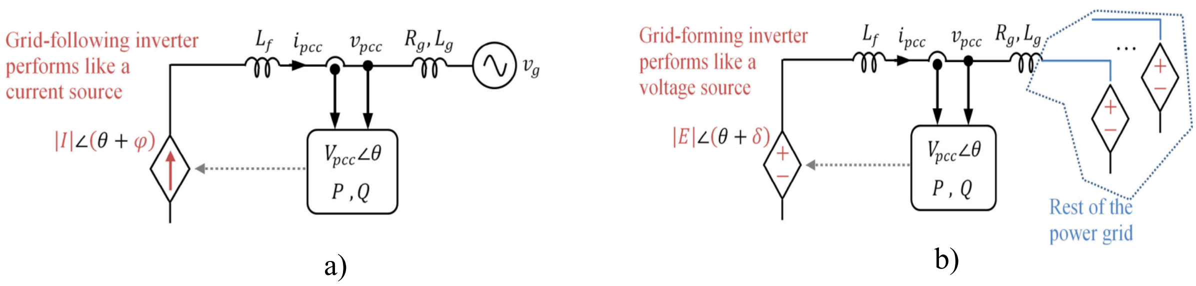

Figure 3.8 – a) Grid following inverter b) Grid forming inverter (MIRAFZAL; ADIB, 2020)

Most IBRs in service today are GFL's. These inverters supply current to the electrical grid through the LC, LCL filters. However, to achieve this, IBR GFL's require a fast-acting timing function, known as a Phase Locked Loop (PLL), which determines the grid voltage angle at the point of connection of the inverter. In this context, the GFL IBR controls follow the measured grid voltage, and the voltage tracking must be fast and accurate to maintain a stable inverter output. These systems can be represented as a constant current source, as shown in Figure 3.8 a). These systems need an external network or a GFM inverter for their operation.

Likewise, GFM inverters locally control the frequency and voltage at the inverter output. This allows the operation of a system in isolated mode (forming the voltage and frequency network). However, these systems are also controlled to synchronize with an external grid, which causes an attraction in the use of microgrids. These GFM inverters can be represented as voltage sources, as shown in Figure 3.8 b). Finally, the GFL and GFM inverter control variations are briefly described in Table 3.5.

Table 3.5 shows the fundamental differences between the IBR controls with the interaction with the electrical grid. As mentioned above, the main purpose of GFL is to supply power and support the grid. On the contrary, in GFM, the main objective is to regulate the voltage and frequency of an islanded microgrid. Also, since GFLs depend on mains voltage and angle measurements to remain synchronized, a fault event or sudden

Table 3.5 – Comparison of Grid-Following and Grid-Forming Controls

Inverter Attribute	**Grid - Following**	**Grid - Forming**
Reliance grid voltage	It is based on a well-defined mains voltage (PCC).	Actively maintains internal voltage magnitude and phase angle.
Dynamic behavior	Controls current injected into the grid (PCC).	Sets voltage magnitude and frequency/phase
PLL synchronization	Needs PLL or equivalent fast control for synchronization.	Does not need PLL for tight synchronization of current controls but may use a PLL o re-synchronize with the network.
Black start	Not usually possible.	It can star automatically in the absence of mains voltage

changes in mains signals can cause an IBR output. This problem is reduced by GFM, enabling operation without requiring dependence on electrical grid signals. In the following subsection, for a better understanding about the IBRs, the principle of operation and modulation is described.

3.5.1 Principle of operation and modulation of IBRs

Inverters are used for the conversion of direct current (DC) to alternating current (AC) and are connected to the electrical grid to supply power through the LCL filters, as shown in Figure 3.9. These IBRs can be single-phase or three-phase with two levels. Depending on how the inverter works within a microgrid, different control strategies can be used, and to cause different dynamic behaviors. These are known as GFM and, GFL.

The two-level inverter illustrated in Figure 3.10 consists of three legs (Sa, Sb, Sc), each of which consists of two switching modules. The switching modules consist of IGBTs (Insulated Gate Bipolar Transistors) or MOSFETs (Metal Oxide Semiconductors), and a diode connected in anti-parallel for the purpose of bidirectional current flow (SALEH; RAHMAN, 2011). The switching modules of each leg of the inverter (Sa, Sb, Sc), can be in two available states each. The total configurations of the switching modules are therefore $2^3 = 8$. However, six configurations are called *basic vectors* and two *zero vectors*, since they represent zero volts at the terminals. These configurations can be represented in eight different binary values (MOHAN; UNDELAND; ROBBINS, 2003). Each of the

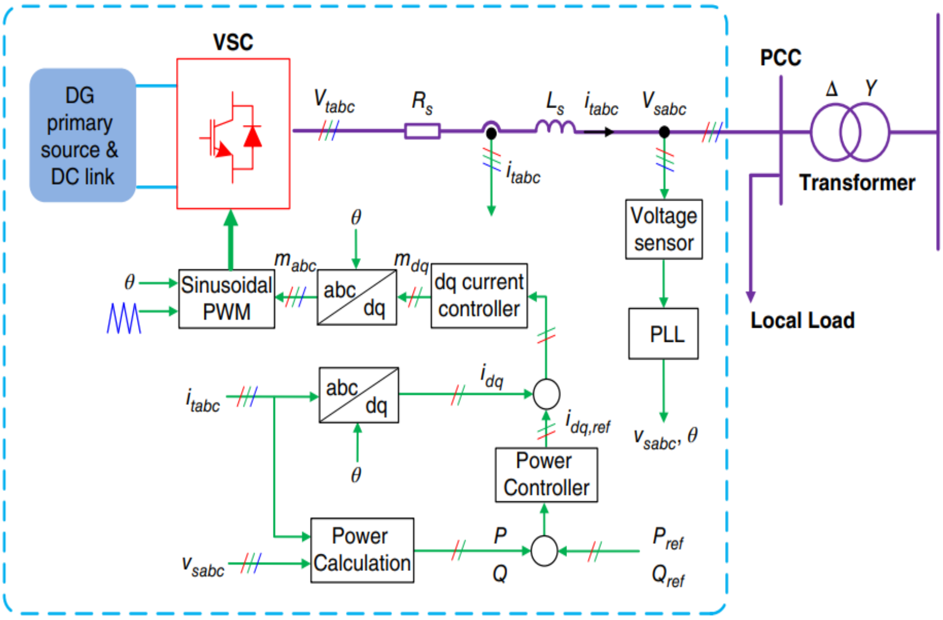

Figure 3.9 – A typical three-phase current-sourced inverter (FARHANGI; JOOS, 2019)

three binary digits refers to a section, where the value 1 indicates the switching module is closed, while the value 0 indicates that the switching module is open.

The commands to turn the switching modules *on* and *off* are issued through the pulse width modulation (PWM) strategy. This PWM strategy is widely used in inverters, it compares a high-frequency triangular waveform, known as the carrier signal, with a sinusoidal waveform, called the modulating signal. Figure 3.11 illustrates the waveforms of the switching functions, according to the PWM strategy, where the switching function of a switch is defined as 1, if the switch is commanded to conduct, 0, if the switch is off.

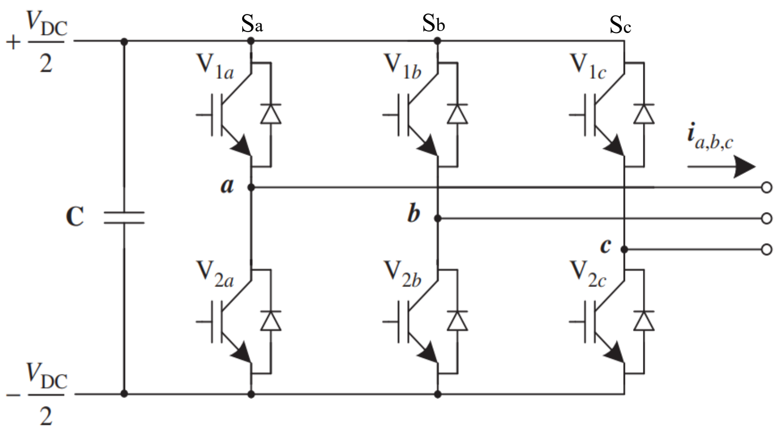

Figure 3.10 – Two-level inverter topology

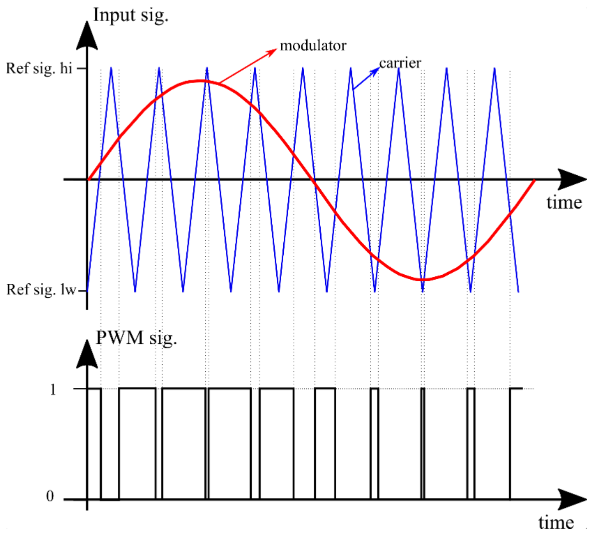

Figure 3.11 – Output of the PWM modulator for given modulator and carrier signals

3.6 Mathematical Modeling of IBR Grid Forming

The GFM inverter generates a nominal sinusoidal voltage V_{ref} determined by a reference voltage amplitude and frequency w_{ref}, this allows a system to operate in islanded mode (ROCABERT et al., 2012) (maintains fixed voltage and frequency). This feature provides stability under challenging grid conditions and can be further enhanced with additional controls and equipment. In the event of load variations, microgrid operation mode transitions or generation source output, GFM inverters respond immediately by providing active power P and reactive power Q as needed.

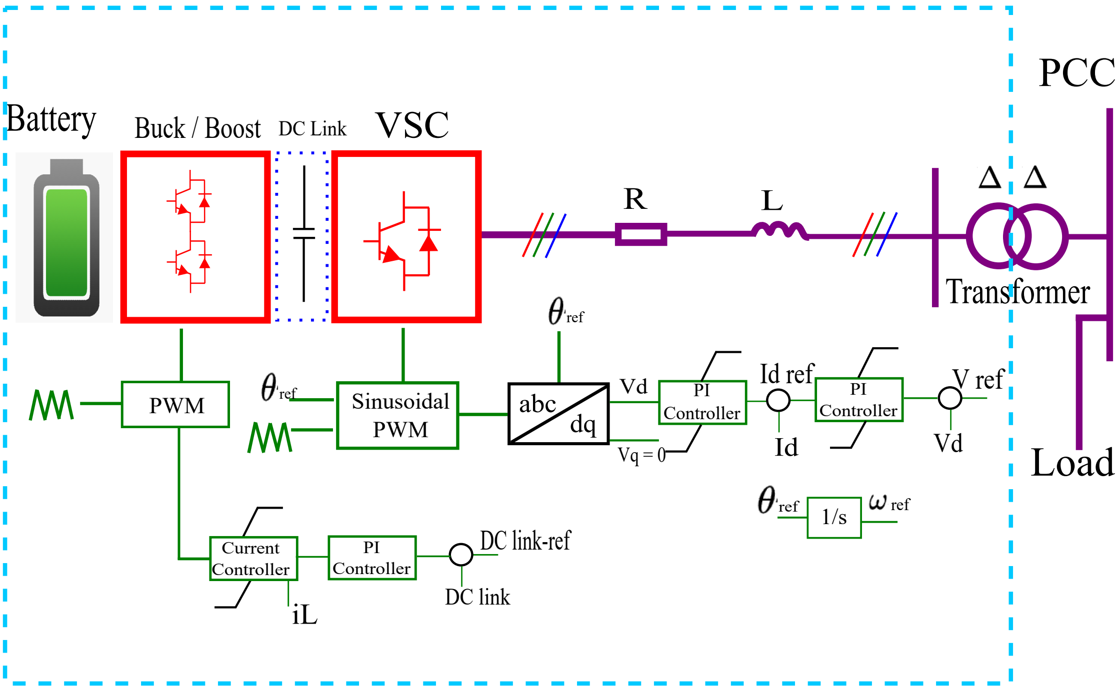

Figure 3.12 – Basic Structure Grid Forming Control (FARHANGI; JOOS, 2019)

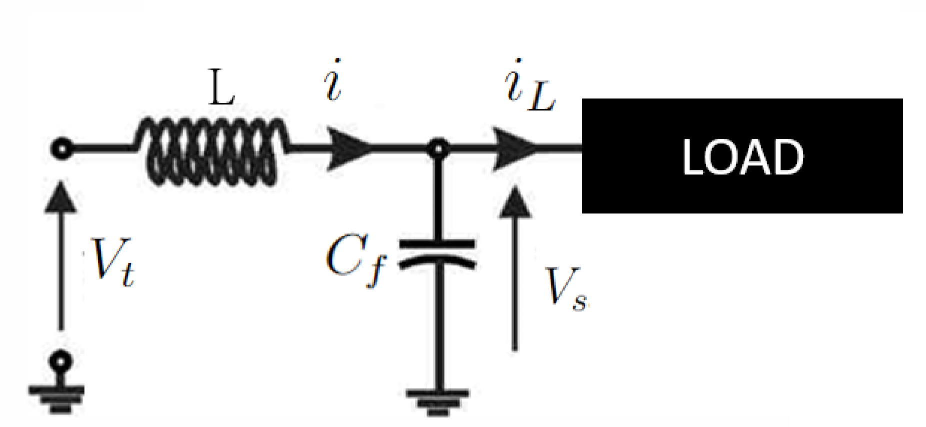

Figure 3.13 – Grid Forming IBR filter LC

Likewise, Figure 3.12 shows a basic structure of the grid forming control, where the reference inputs are voltage V_{ref} and frequency ω_{ref}. In fact, the reference voltage passes through the cascaded PI control loops, which work in the reference frame of the axis dq, likewise, the reference frequency passes through an integrator, obtaining the reference output angle θ_{ref}. In order to maintain the reference voltage in the islanded system, the mathematical model of the voltage controller is given considering the filter capacitor voltage and the inductor current (TALAPUR et al., 2018), shown in Figure 3.13, in this context, the current in the three phases (a, b, c) is:

$$\left\{\begin{matrix} C_f \frac{dV_{sa}}{dt} = i_a - i_{La} \\ C_f \frac{dV_{sb}}{dt} = i_b - i_{Lb} \\ C_f \frac{dV_{sc}}{dt} = i_c - i_{Lc} \end{matrix}\right\} \tag{3.16}$$

Eq.(3.16) constitute the space vector.

$$C_f \frac{d\overrightarrow{V_s}}{dt} = \overrightarrow{i} - \overrightarrow{i_L} \tag{3.17}$$

expressing each space vector in Eq.(3.17) in terms of its frame components dq, we get Eqs.(3.19), and (3.20).

$$C_f \frac{d}{dt}[(V_{sd} + jV_{sq})e^{j\rho}] = (i_d + ji_q)e^{j\rho} - (i_{Ld} + ji_{Lq})e^{j\rho} \tag{3.18}$$

$$C_f \frac{dV_{sd}}{dt} = C_f(\omega V_{sq}) + i_d - i_{Ld} \tag{3.19}$$

$$C_f \frac{dV_{sq}}{dt} = -C_f(\omega V_{sd}) + i_q - i_{Lq} \tag{3.20}$$

from Eqs.(3.19), and (3.20) in the dq coordinate and applying the Laplace transform, we obtain Eq.(3.21).

$$\begin{Bmatrix} C_f S V_{sd}(s) - C_f \omega V_{sq}(s) - I_d(s) + I_{Ld}(s) = 0 \\ C_f S V_{sq}(s) + C_f \omega V_{sd}(s) - I_q(s) + I_{Lq}(s) = 0 \end{Bmatrix} \tag{3.21}$$

from Eq.(3.21), the $C_f \omega V_{dq}$ components are decoupled and we obtain the following transfer function:

$$\begin{Bmatrix} V_{sd}(s) = \frac{1}{C_f S}(I_d(s) - I_{Ld}(s)) \\ V_{sq}(s) = \frac{1}{C_f S}(I_q(s) - I_{Lq}(s)) \end{Bmatrix} \tag{3.22}$$

by this Eq.(3.22), we can control the inverter voltage.

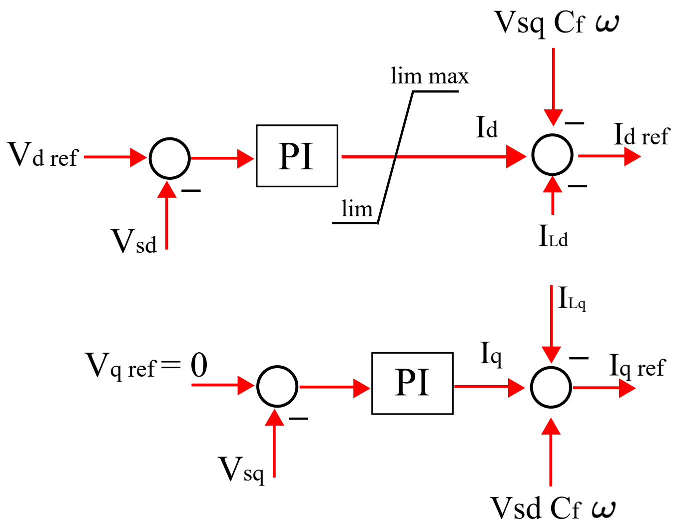

Figure 3.14 – GFM IBR Voltage control loop

The purpose of the control in Figure 3.14 is to regulate the amplitude of the load voltage V_s. However, V_s can assume different phase with respect to the d axis. A possible combination, which is adopted in this work, is $V_{sd} = V_{ref}$ and $V_{sq} = 0$, in this context V_{sq} is forced to zero.

Likewise, to determine the current control loop, the filter LC in Figure 3.15 is considered. Applying Kirchhoff's second Law in Figure 3.15, the voltage equation at the output terminals of the GFM inverter is:

$$\begin{Bmatrix} V_t = Ri_a + L_f \frac{di_a}{dt} + V_{sa} \\ V_t = Ri_b + L_f \frac{di_b}{dt} + V_{sb} \\ V_t = Ri_c + L_f \frac{di_c}{dt} + V_{sc} \end{Bmatrix} \tag{3.23}$$

it is possible to reduce Eq.(3.23) a general form as in Eq.(3.24), where $\vec{V_t}$, $\vec{V_s}$, and $\vec{i}$ are space vectors.

$$\vec{V_t} = R\vec{i} + L\frac{\vec{i}}{dt} + \vec{V_s} \tag{3.24}$$

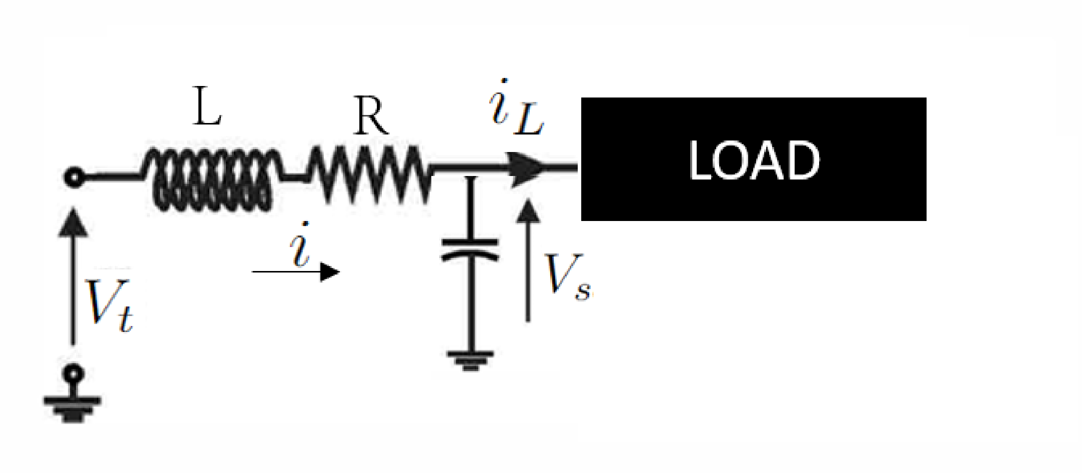

Figure 3.15 – Grid Forming IBR filter LC

using park's transformations, we get:

$$V_{t-d,q}e^{j\omega t} = Ri_{dq}e^{j\omega t} + L\frac{i_{dq}}{dt}e^{j\omega t} + V_{s-d,q}e^{j\omega t} \tag{3.25}$$

likewise, from Eq.(3.25), we get:

$$V_{t-d,q} = j\omega Li_{d,q} + Ri_{d,q} + L\frac{di_{d,q}}{dt} + V_{s-d,q} \tag{3.26}$$

where:

$$U_{d,q} = Ri_{d,q} + L\frac{di_{d,q}}{dt} \tag{3.27}$$

applying the Laplace transform, Eq.(3.27) results in:

$$\begin{Bmatrix} V_{t,d}(s) - RI_d(s) - SLI_d(S) + \omega LI_q(s) - V_{s,d}(s) = 0 \\ V_{t,q}(s) - RI_q(s) - SLI_q(S) - \omega LI_d(s) - V_{s,q}(s) = 0 \end{Bmatrix} \tag{3.28}$$

of the Eq.(3.28) in *dq* coordinates they are linked together. Thus, for a better analysis of the modeling, the components $\omega LI_{d,q}(s)$ and $V_{s,d,q}(s)$ are decoupled and we can obtain:

$$\begin{Bmatrix} V_{t,d}(s).\frac{1}{R+SL} = I_d(s) \\ V_{t,q}(s).\frac{1}{R+SL} = I_q(s) \end{Bmatrix} \tag{3.29}$$

it can be seen that there is a direct relationship between the current in the dq axes and the inverter output voltage V_t through the Eq.(3.29). Likewise, this is represented in Figure 3.16, through of block diagrams.

Figure 3.17 shows the block diagram representation of the GFM control, in cascade. The objective of this control is to keep the microgrid stable in islanded mode, through the voltage and frequency control.

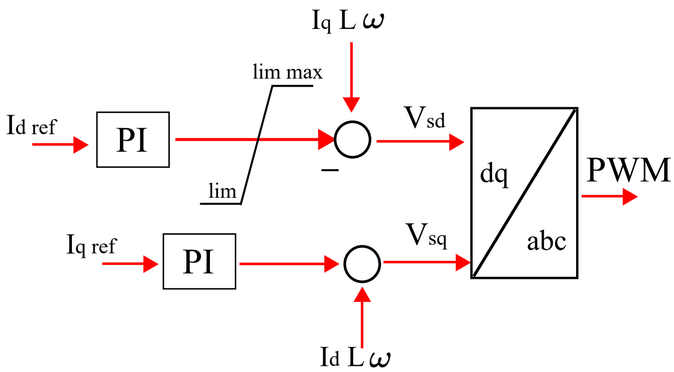

Figure 3.16 – GFL IBR Current control loop

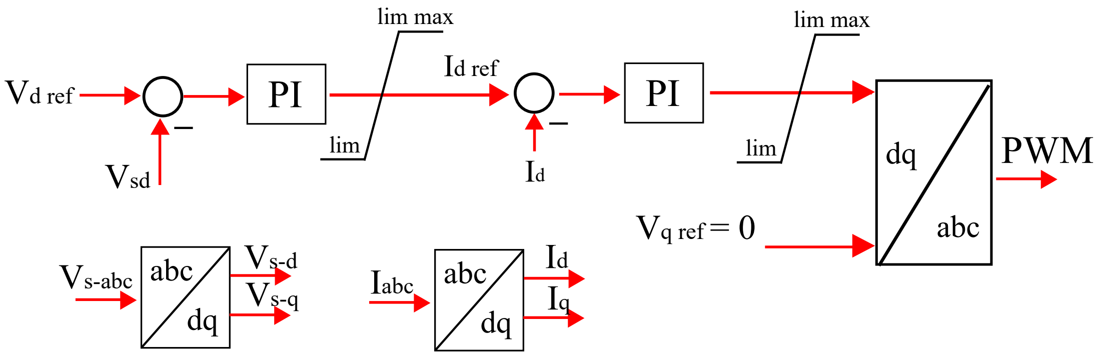

Figure 3.17 – Grid Forming - Cascaded control structure

3.7 Mathematical Modeling of IBR Grid Following

This mode of operation is possible if there is a local synchronous generator, or a GFM inverter, which establishes the amplitude of the voltage and frequency. If the PLL is mis-tuned and cannot accurately and quickly track the external voltage, the GFL inverter cannot maintain a stable output, resulting in system inverter output or shutdown. Figures 3.18, and 3.19 shows the control structure of the power inverter in GFL mode.

In this context, **grid synchronization** is one of the most important issues in the integration of IBRs in electrical systems. The magnitude and angle of the voltage of the concession network are used to synchronize the output variables of the inverters, this is fundamental for the control of the IBR. In this context, the synchronization is done by a Phase Locked Loop (PLL) (RODRIGUEZ et al., 2007), which must quickly and accurately detect the angle and frequency of the electrical system, even if the system is distorted and unbalanced.

A block diagram of the synchronous frame three-phase PLL is shown in Figure 3.20. A transformation of the voltages of the three phases (V_{Sa}, V_{Sb}, V_{Sc}) to dq rotating reference frame is performed by Clarke and Park transforms. These dq reference frame signals are controlled by a feedback loop that regulates the q component to zero through PI controls, in order to track the frequency. The Clarke and Park transform are essential to implement vector control methods in inverters for synchronization. Basically, the Clarke

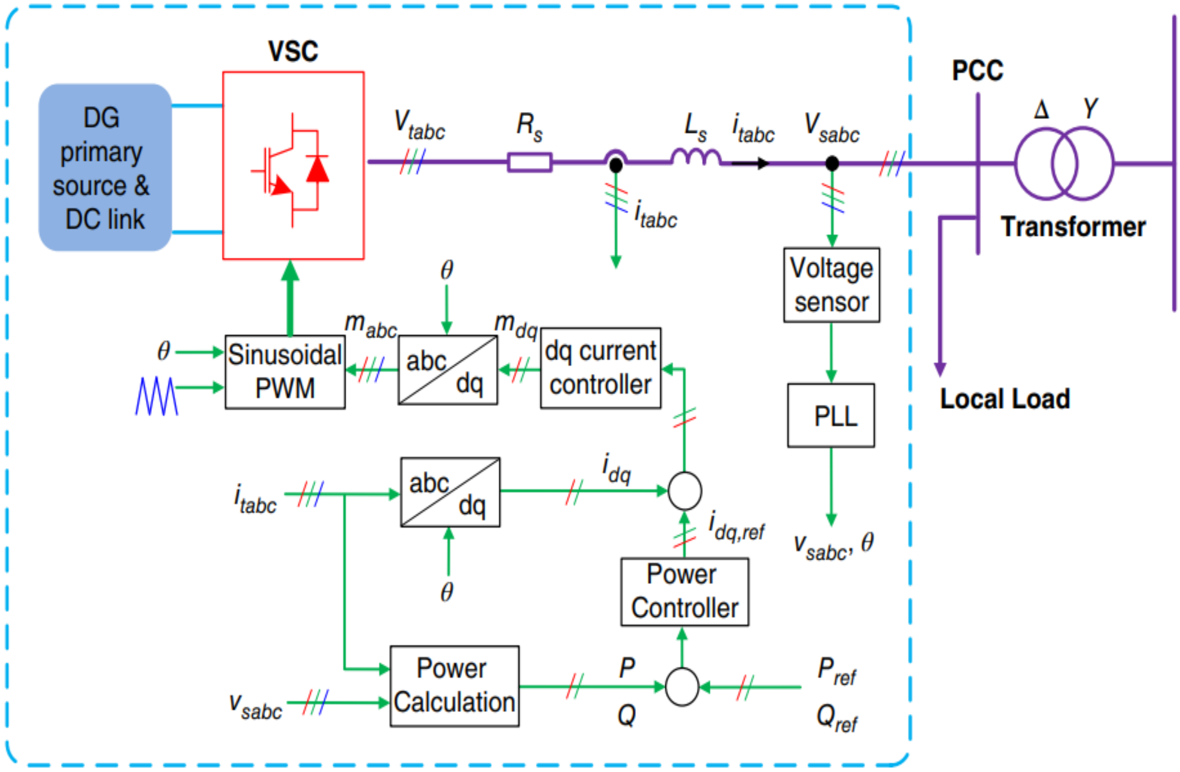

Figure 3.18 – A typical three-phase voltage-sourced inverter(FARHANGI; JOOS, 2019)

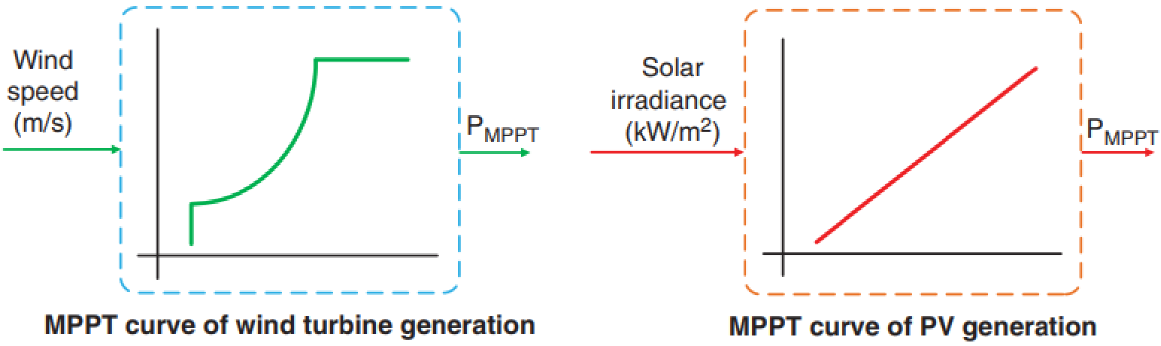

Figure 3.19 – MPPT curve

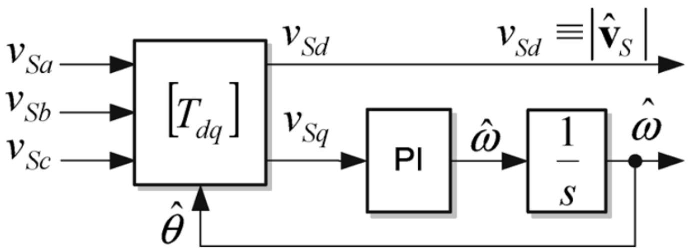

Figure 3.20 – Basic block diagram of the SRF-PLL (RODRIGUEZ et al., 2007)

transformation converts the stationary quantities (a, b, c) to quantities $(\alpha - \beta)$. While the Park transformation converts the quantities $(\alpha - \beta)$ into rotational quantities $(d - q)$.

Clark and Park transforms are described in the Appendix A.5.

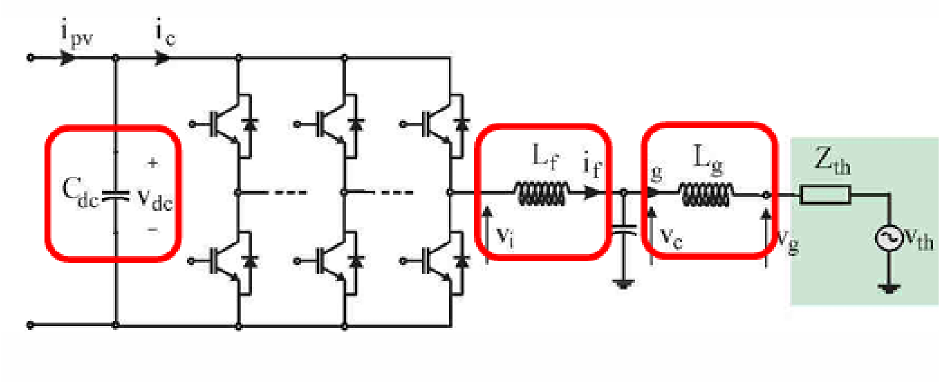

Figure 3.21 – Configuration Inverter

Likewise, the dynamic of IBRs synthesizes an output voltage that forces the circulation of a current. In this case, the effects of switching harmonics are neglected, consistent with the operating principle of the PWM modulator. Figure 3.21 shows the variables that can be controlled in the inverters, the current in the capacitors and the currents in the inductors at the inverter output. They are selected to perform inverter controls. The Figure 3.22 shows the output elements of the inductor. In this context, the capacitor is used to filter the high-frequency components, but our control is at 60Hz, the current at 60Hz passes mostly through the inductors. For a simplification of the model, the capacitor is disregarded, as shown in Figure 3.23 the simplified structure.

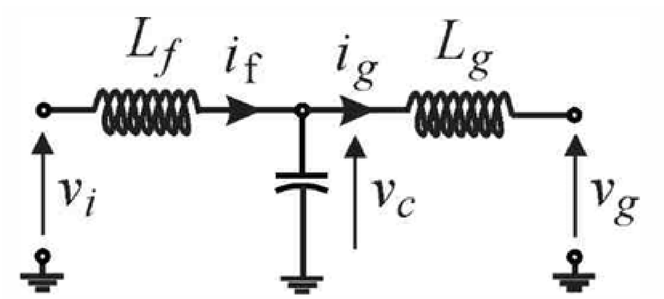

Figure 3.22 – Inverter output elements - LCL filter

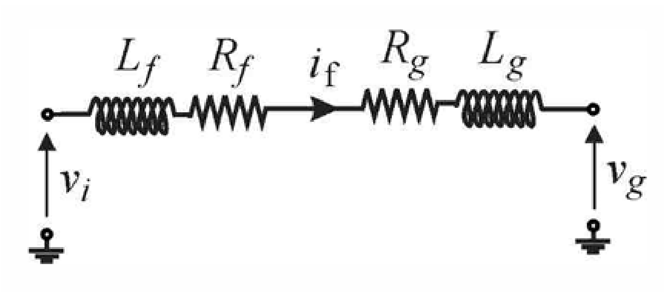

Figure 3.23 – Simplified structure - LCL filter

From Figure 3.23, through Kirchhoff's second law, we obtain:

$$\begin{Bmatrix} V_{ia}(t) - (R_f + R_g)i_a(t) - (L_f + L_g)\frac{di_a(t)}{dt} - V_{ga}(t) = 0 \\ V_{ib}(t) - (R_f + R_g)i_b(t) - (L_f + L_g)\frac{di_b(t)}{dt} - v_{gb}(t) = 0 \\ V_{ic}(t) - (R_f + R_g)i_c(t) - (L_f + L_g)\frac{di_c(t)}{dt} - v_{gc}(t) = 0 \end{Bmatrix} \tag{3.30}$$

Eq.(3.30) are reduced in a general form as in Eq.(3.31), where $\overrightarrow{V_i}$, $\overrightarrow{V_g}$, and $\overrightarrow{i}$ are space vectors in:

$$\overrightarrow{V_i} - R\overrightarrow{i} - L\frac{d\overrightarrow{i}}{dt} - \overrightarrow{V_g} = 0 \tag{3.31}$$

where :

$$\begin{Bmatrix} R = R_f + R_g \\ L = L_f + L_g \end{Bmatrix} \tag{3.32}$$

carrying out the transformation from abc to $\alpha\beta$ of Eq.(3.31), we obtain :

$$\overrightarrow{V_{i,\alpha\beta}} - R\overrightarrow{i_{\alpha\beta}} - L\frac{d\overrightarrow{i_{\alpha\beta}}}{dt} - \overrightarrow{V_{g,\alpha\beta}} = 0 \tag{3.33}$$

and

$$\begin{Bmatrix} V_{i\alpha}(t) - Ri_\alpha(t) - L\frac{di_\alpha(t)}{dt} - V_{g\alpha}(t) = 0 \\ V_{i\beta}(t) - Ri_\beta(t) - L\frac{di_\beta(t)}{dt} - V_{g\beta}(t) = 0 \end{Bmatrix} \tag{3.34}$$

applying Park transformation, we obtain:

$$(\overrightarrow{V_{i,\alpha\beta}} - R\overrightarrow{i_{\alpha\beta}} - L\frac{d\overrightarrow{i_{\alpha\beta}}}{dt} - \overrightarrow{V_{g,\alpha\beta}} = 0).(e^{-j\rho}.e^{j\rho}) \tag{3.35}$$

noting that $\overrightarrow{X_{\alpha\beta}}.e^{-j\rho} = \overrightarrow{X_{dq}}$, we can obtain:

$$\overrightarrow{V_{i,dq}}.e^{j\rho} - R\overrightarrow{i_{dq}}.e^{j\rho} - L\frac{d\overrightarrow{i_{qd}}}{dt}.e^{j\rho} - \overrightarrow{V_{g,dq}}.e^{j\rho} = 0 \tag{3.36}$$

and

$$\overrightarrow{V_{i,dq}}.e^{j\rho} - R\overrightarrow{i_{dq}}.e^{j\rho} - L\frac{d\overrightarrow{i_{qd}}}{dt}.e^{j\rho} - jL\overrightarrow{i_{dq}}\frac{d\rho}{dt}.e^{j\rho} - \overrightarrow{V_{g,dq}}.e^{j\rho} = 0 \tag{3.37}$$

separating into real and imaginary parts, we get:

$$\begin{Bmatrix} V_{i,d} - Ri_d - L\frac{di_d}{dt} + Li_q\frac{d\rho}{dt} - V_{g,d} = 0 \\ V_{i,q} - Ri_q - L\frac{di_q}{dt} - Li_d\frac{d\rho}{dt} - V_{g,q} = 0 \end{Bmatrix} \tag{3.38}$$

from Eq.(3.38).Applying the Laplace transform, we obtain:

$$\begin{Bmatrix} V_{i,d}(s) - RI_d(s) - SLI_d(s) + \omega LI_q(s) - V_{g,d}(s) = 0 \\ V_{i,q}(s) - RI_q(s) - SLI_q(s) - \omega LI_d(s) - V_{g,q}(s) = 0 \end{Bmatrix} \tag{3.39}$$

for a better analysis of the modeling, the components $\omega LI_{d,q}(s)$ and $V_{g,d,q}(s)$ are decoupled, and we will obtain:

$$\begin{Bmatrix} V_{i,d}(s) - RI_d(s) - sLI_d(s) = 0 \\ V_{i,q}(s) - RI_q(s) - sLI_q(s) = 0 \end{Bmatrix} \tag{3.40}$$

it can be seen, in Eq.(3.40) there is a direct relationship between the current in the dq axes and the inverter output voltage V_i through the Eq.(3.41).

$$\begin{Bmatrix} I_d(s) = \frac{V_{i,d}(s)}{R+sL} \\ I_q(s) = \frac{V_{i,q}(s)}{R+sL} \end{Bmatrix} \tag{3.41}$$

by this equation, we can control the inverter current. The current mesh control diagram is shown in Figure 3.24.

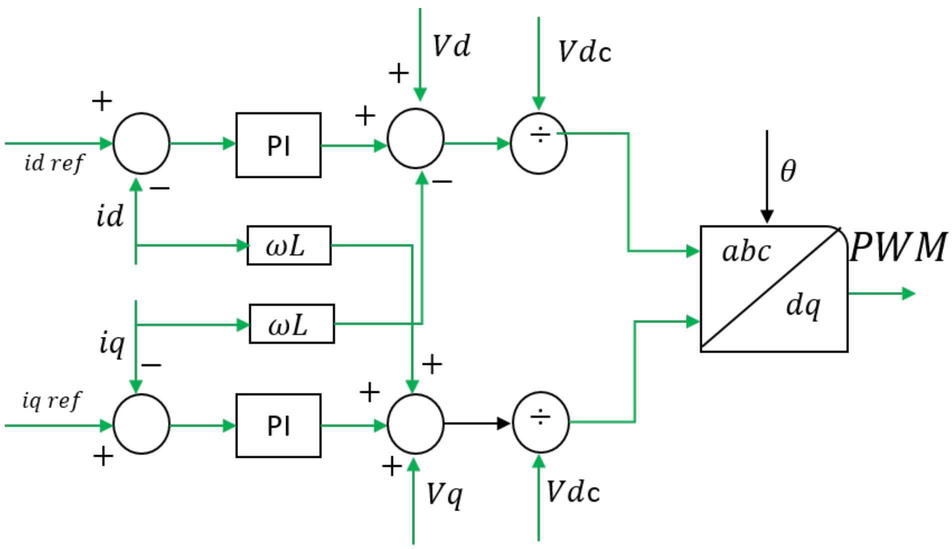

Figure 3.24 – GFL IBR Current control Loop

As shown in Figure 3.24 , it represents the modeling of the system. The currents in the dq axes are compared with the measured currents, the error is passed through the PI controller, the decoupled components are added in Eq.(3.41) $\omega LI_{d,q}(s)$, and $V_{g,d,q}(s)$.

Likewise, power control is an external control loop. This module is responsible for generating the reference currents of the dq axes and passes through the current loop from the preset active and reactive power references, as shown in Figure 3.25. In fact, the reference currents are obtained by equations:

$$i_{dref} = \frac{V_d.P_{ref} + V_q.Q_{ref}}{V_d^2 + V_q^2} \tag{3.42}$$

,and

$$i_{qref} = \frac{V_q.P_{ref} - V_d.Q_{ref}}{V_d^2 + V_q^2} \tag{3.43}$$

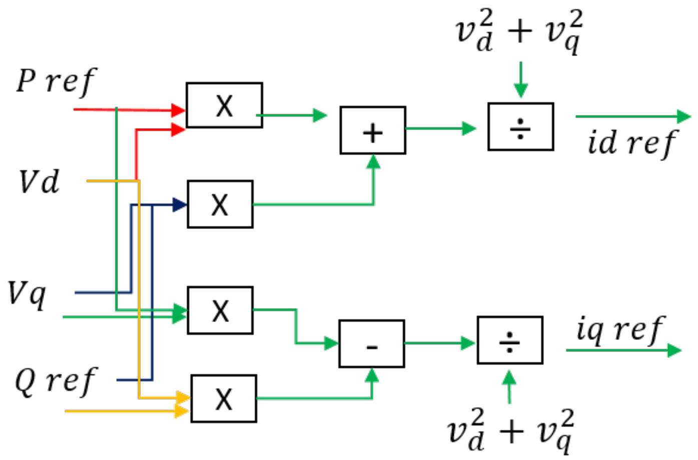

Figure 3.25 – GFL IBR Power control Loop

3.8 Battery pack

Recently, storage systems are receiving considerable attention, particularly as a solution to the challenges of modern distribution systems (microgrids). Batteries play a crucial role in microgrids and provide auxiliary keys such as load switching, dynamic local voltage support, short-term frequency smoothing, and grid contingency support (MEEGAHAPOLA, 2018). However, one of the challenges in microgrids is island mode operation. The operation of the storage system with a GFM control structure supplies constant voltage and frequency to keep the system stable. In this context, the need to have a model that reflects the behavior and performance of the system is in fact important.

3.8.1 Battery model

Figure 3.26 is presented as a battery diagram implemented in Typhoon Hil (Typhoon HIL, Typhoon HIL). It is modeled as a controllable DC voltage source with a series resistor R_{bat}. The DC source is controlled by the state of charge (SOC) of the battery using non-linear equation. The battery voltage as a function of the state of charge (it), is defined as:

$$E = E_o - K\frac{Q}{Q - it} + A.exp(-B.it) \tag{3.44}$$

(it) expressed by:

$$it = \int_0^t ibat.dt \tag{3.45}$$

the others constants that appear in Eq.(3.44) are:

$$A = E_{full} - E_{exp} \tag{3.46}$$

were, the A is voltage drop during the exponential zone.

$$B = \frac{3}{Q_{exp}} \tag{3.47}$$

K: polarization voltage, expressed by:

$$K = \frac{E_{full} - E_{nom} + A(exp(-B.Qnom) - 1).(Q - Q_{nom})}{Q_{nom}} \tag{3.48}$$

voltage constant E_o, that can be given by:

$$E_o = E_{full} + K + R_{bat}.i - A \tag{3.49}$$

where i is the rated discharge current. The series resistance is calculated by assumption that the battery efficiency is 99.5% by (Typhoon HIL, Typhoon HIL).

$$R_{bat} = V_{nom}.\frac{1 - 0.995}{0.2.Q_{nom}} \tag{3.50}$$

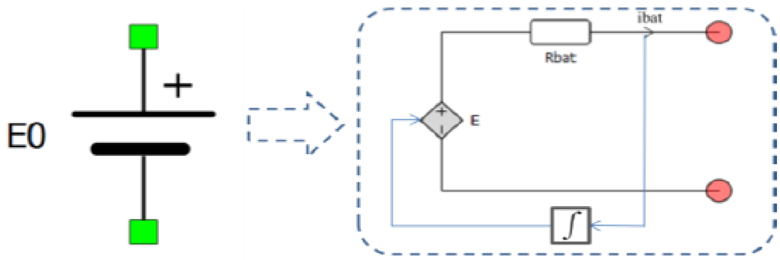

Figure 3.26 – Battery model in Typhoon HIL (Typhoon HIL, Typhoon HIL)

There are three points at the battery's discharge curve (Figure 3.27) that are used by the equations:

- Fully charged battery ($Vfull$, Q - rated capacity of the battery).
- End of exponential zone ($Vexp, Qexp$).
- End of nominal zone ($Vnom, Qnom$)

3.8.2 Buck/boost converter model

The buck/boost converter is responsible for DC link capacitor voltage control and properly charging and discharging the battery. Also, it uses a cascaded PI controller to generate the duty cycle for the switches based on the DC link voltage difference and its set-point (FARROKHABADI et al., 2020), as shown in Figure 3.28. In this context,

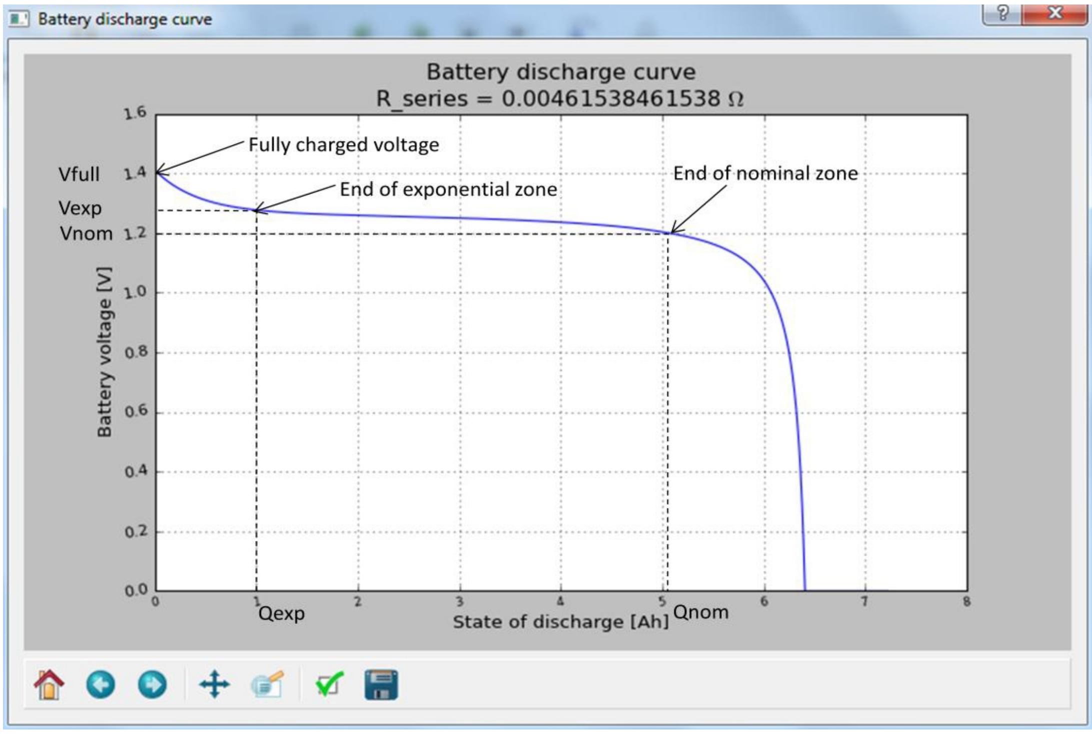

Figure 3.27 – Battery discharge curve - Typhoon schematic (Typhoon HIL, Typhoon HIL)

the buck/ boost contains a faster internal current control loop structure and an external voltage control loop.

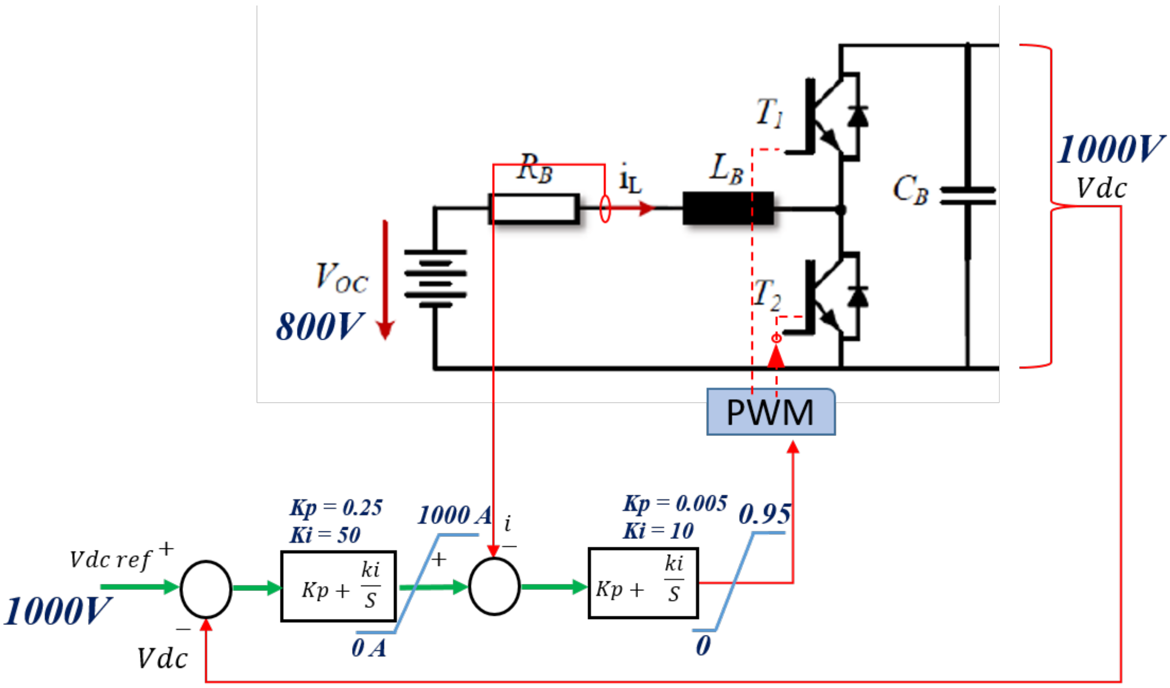

Figure 3.28 – Bi-directional dc-dc converter

The state variables of the converter are identified as the current flowing through the converter input inductor and the DC link voltage at the output. Likewise, the equations that govern the state variables when the upper switch T_1 is conducting are formulated as:

$$L_B.\frac{di_L}{dt} = V_{OC} - i_L(R_B) - V_{out} \tag{3.51}$$

and

$$C_B.\frac{dV_{out}}{dt} = i_L - \frac{V_{out}}{R_L} \tag{3.52}$$

and when the lower switch T2 is conducting respectively:

$$L_B.\frac{di_L}{dt} = V_{OC} - i_L(R_B) \tag{3.53}$$

and

$$C_B.\frac{dV_{out}}{dt} = -\frac{V_{out}}{R_L} \tag{3.54}$$

3.9 Comments and Conclusions

In this chapter, the models of the elements that make up a microgrid were explored. Initially, the network and microgrid loads were modeled and classified as static elements. Likewise, the control models of the IBR, grid following, and grid forming were addressed with greater emphasis, in this context comparison of their benefits in the operation of a microgrid was made. Also, the buck/boost converters were modeled, as well as the batteries. These models will be useful in modeling the CAMPUSGRID microgrid. In the following chapter, the test microgrid is described, likewise, the models used in the Typhoon HIL Control Center software are shown.

4 System under Study : CAMPUSGRID

In this chapter, the implementation of a microgrid, called CAMPUSGRID, is presented. It will be a microgrid deployed at the State University of Campinas (UNICAMP) in Brazil, which will serve a set of loads within it. The focus of this chapter is the location, the types of generation within the microgrid as well as their description and the specifications to carry out studies of them. Likewise, the computational tool for the implementation and simulation of this system is mentioned.

4.1 CAMPUSGRID microgrid

The growing interest in microgrids accompanies the need to better understand the new scenarios, which translates into various implementations carried out in the world, ranging from laboratory microgrids to pilot projects. In this context, the ($P\&D$) MERGE (Microgrids for Efficient, Reliable, and Greener Energy) research and development project was proposed, which began in 2020, with the aim of implementing four microgrids with different purposes and characteristics (LÓPEZ et al., 2020). Among these, CAMPUSGRID is one of the university AC microgrids within the UNICAMP university, in which the installation of an energy storage system will be carried out, and extensive use of photovoltaic generation the implementation of a energy management with extensive measurement of demand and generation. This will be the largest microgrid built in Brazil and has been implemented thanks to the joint efforts of a multidisciplinary team of researchers in energy systems, power electronics and computing. The MERGE project is executed by UNICAMP, the Federal University of Maranhao (UFMA) and the Advanced Institute of Technology and Innovation (IATI), with financing from CPFL Energia through the ANEEL $R\&D$ Program (LÓPEZ et al., 2020).

4.1.1 Description of microgrid

CAMPUSGRID is a microgrid that is being implemented on the UNICAMP university campus, in the district of Barao Geraldo, a suburban area in the center of Campinas - Sao Paulo. This system is connected to the medium voltage concessionary network at 11.9KV, and feeds different loads of the university campus, the Multidisciplinary Gymnasium/ Convention Center (GMU), the Faculty of Physical Education (FEF), the Rare Works Library (BORA), and the Central Library (BC) César Lattes (QUADROS et al., 2021). The system will include 975 KWp photovoltaic generation plants (PV), a bus charging station, a 1MVA battery-based energy storage system (BESS), and 300 KVA gas generators. Likewise, it will have an interconnection key to the main network, which must allow its operation in islanded mode and connected to the concession network. Currently, CAMPUSGRID is in the process of quoting its components and installation.

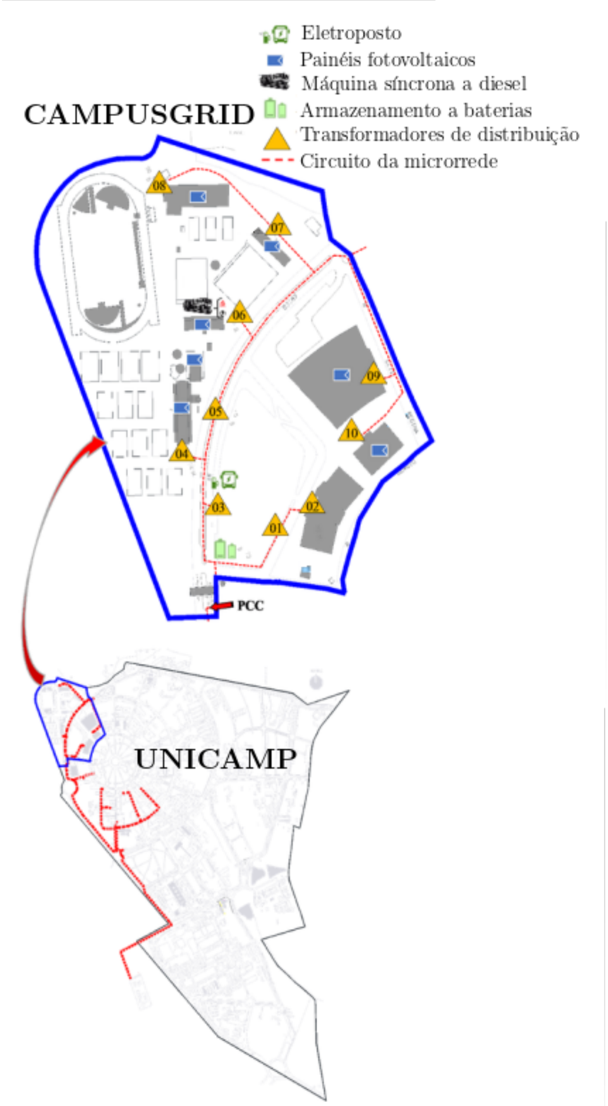

Figure 4.1 – Map of the university of Campinas and the CAMPUSGRID microgrid (QUADROS et al., 2021)

Figure 4.1 shows the main devices of the microgrids such as the location of the generation sources, transformers and loads to be fed. There are 337 KWp of photovoltaic panels installed on the roof of the GMU with a plan to add 620 KWp distributed, which will cover most of the constructions belonging to the microgrid area. Likewise, with the aim of increasing reliability and resilience, two dispatchable generation units (natural gas generators) with a capacity of 250 KVA and 50 KVA, respectively, will be installed.

Table 4.1 shows the characteristics of distribution transformers. Likewise, the microgrid contains 11 transformers already installed, plus a 1MVA transformer that will be installed for the BESS storage system, totaling 3370 KVA the total power of the distribution transformers. In addition, Table 4.2 shows electrical characteristics of the feeders, as well as the distances between them. Finally, from the electrical energy measurements of the individual CAMPUSGRID buildings, the maximum energy demand has been extracted, with an average demand of 480.83 KW of active power and 232.86 KVAr of reactive power. Figure 4.2 shows the profile of the maximum demand load for a period of one day, in which academic activities, such as classes and laboratories, are concentrated. These data will be used to model the microgrid in the Typhoon HIL Control Center software, the computational tool used in this work that will be described below.

Table 4.1 – Data transformers

(LP)	Power Nominal KVA	Impedance (%)	Connection (MV - LV)	Voltage
04	45 KVA	2.5%	Δ - Y	11.9Kv/0.22Kv
06	300 KVA	4.5%	Δ - Y	11.9Kv/0.22Kv
06	300 KVA	4.5%	Δ - Y	11.9Kv/0.22Kv
08	1 MVA	6%	Δ - Δ	11.9Kv/0.22Kv
11	112.5 KVA	3.5%	Δ - Y	11.9Kv/0.22Kv
13	112.5 KVA	3.5%	Δ - Y	11.9Kv/0.22Kv
14	75 KVA	3.52%	Δ - Y	11.9Kv/0.22Kv
16	300 KVA	4.58%	Δ - Y	11.9Kv/0.22Kv
18	225 KVA	4.54%	Δ - Y	11.9Kv/0.22Kv
19	300 KVA	4.81%	Δ - Y	11.9Kv/0.22Kv
23	300 KVA	4.81%	Δ - Y	11.9Kv/0.22Kv
25	300 KVA	4.58%	Δ - Y	11.9Kv/0.22Kv

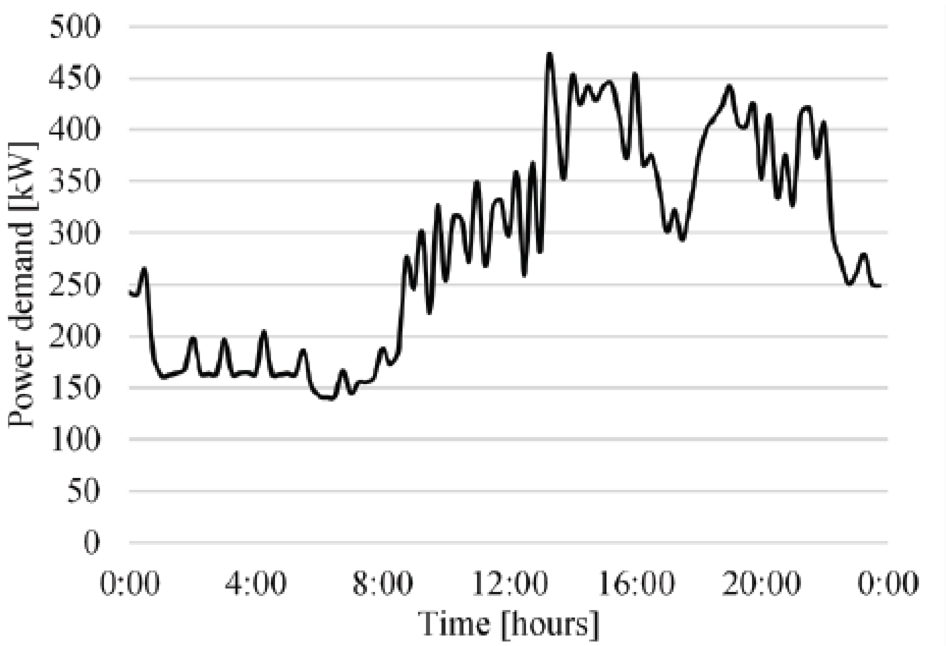

Figure 4.2 – Demand maximum load profile (QUADROS et al., 2021)

Table 4.2 – Electrical Characteristics of the feeders - CAMPUSGRID

Stretch (from)	Stretch (to)	length (m)	R CA (Ω)	L(mH)
1	2	59.09	0.01248	0.28995
2	3	15.48	0.00327	0.07596
3	4	61.64	0.03502	0.04769
4	5	46.90	0.02665	0.03629
5	6	30.53	0.02964	0.01279
3	7	30	-	-
7	8	20	-	-
2	9	18.89	0.00399	0.09269
9	10	96.28	0.03158	0.10446
10	11	14.41	0.00819	0.01115
10	12	27.20	0.00892	0.02951
12	13	33.20	0.03224	0.01391
12	14	42.66	0.01399	0.04629
14	15	89.66	0.02941	0.09728
15	16	14.92	0.00848	0.01154
15	17	90.38	0.02964	0.09806
17	18	58.65	0.03332	0.04538
18	19	149.92	0.08518	0.11600
17	20	52.26	0.01714	0.05670
20	21	30.67	0.01006	0.03328
20	22	145.01	0.08239	0.11220
22	23	26.11	0.02535	0.01094
22	24	19.68	0.01118	0.01523
24	25	83.01	0.08060	0.0378

4.2 CAMPUSGRID at Typhoon HIL Control Center

Based on the present status of the project and its specifications, it was decided to simulate the CAMPUSGRID microgrid with PV photovoltaic generation energy resources, a BESS storage system with the capacity to form the grid, and two gas synchronous machines, as described in Table 4.3. Considering that the inclusion of planned energy resources is sufficient for the dynamic analysis of the microgrid in islanded and connected modes.

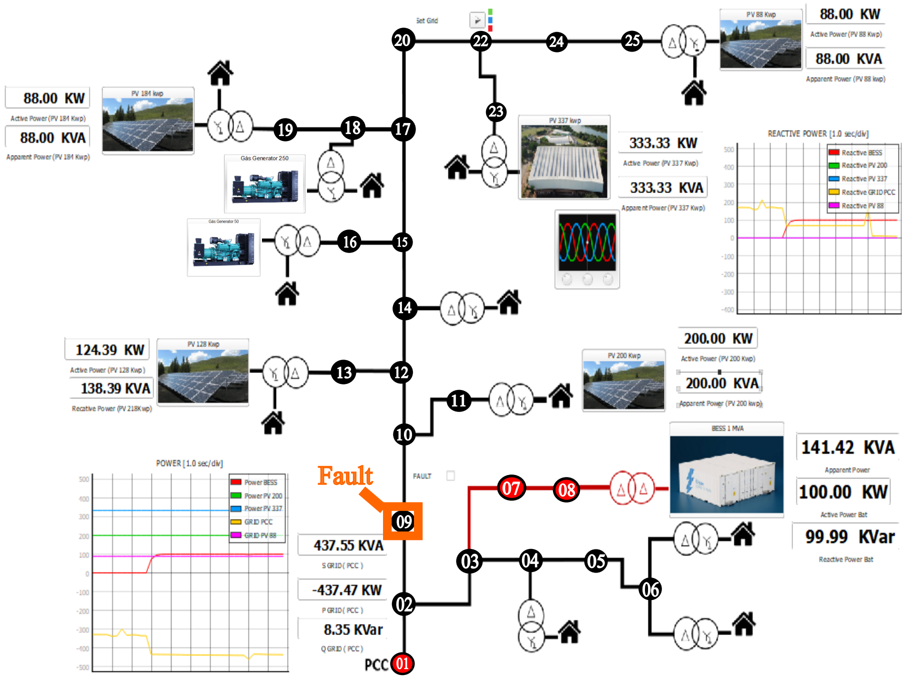

Figure 4.3 – Simulation structure of the CAMPUSGRID microgrid in the Virtual SCADA of Typhoon HIL Control Center.

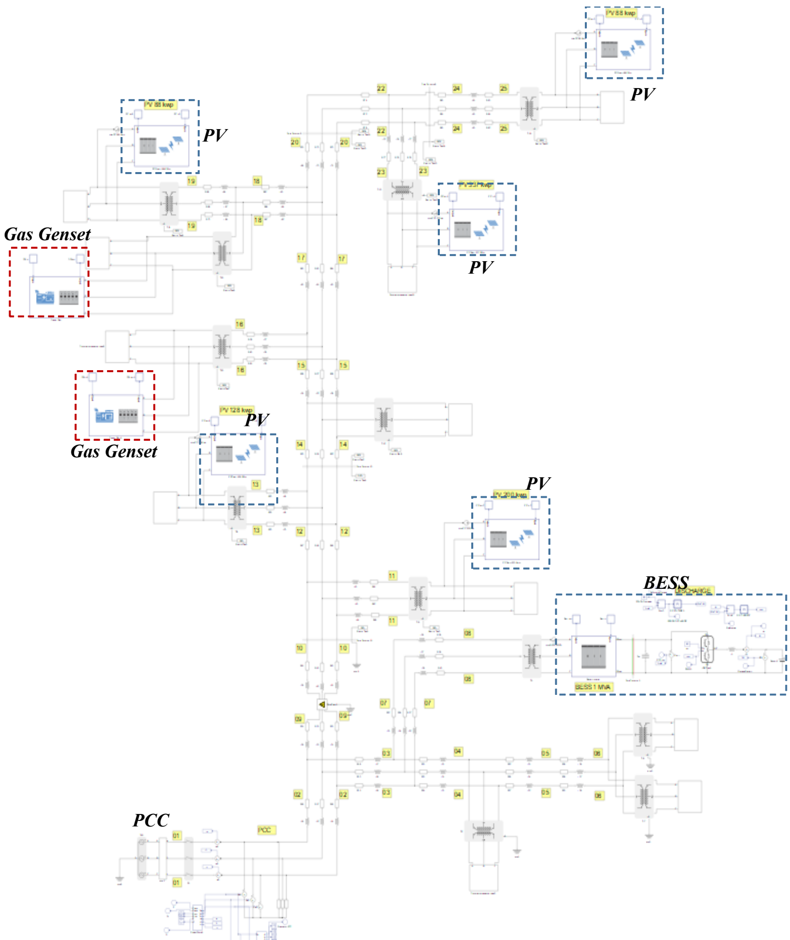

Figure 4.4 – CAMPUSGRID in Schematic Editor

In Figure 4.3 shows the single-line diagram of the designed microgrid with the widgets that Typhoon SCADA makes available. It shows in Figure 4.3, and 4.4 five PV systems connected to the network through transformers at points 25, 23, 19, 13, and 11. Likewise, the BESS storage system supplies energy through the transformer located at point 08. Finally, the Gas generators are located at points 18 and 16.

The results are presented in Section 5, which were obtained through Typhoon HIL Virtual. The models used in Typhoon HIL Control Center are described below.

Table 4.3 – Energy Resources at CAMPUSGRID

Location Point	Component	Capacity	
08	BESS	1MVA/810KWH	not exist
25	PV	88kwp	not exist
23	PV	337kwp	exists
19	PV	184kwp	not exist
13	PV	128kwp	not exist
11	PV	200kwp	not exist
18	GG	50KVA	exists
16	GG	250KVA	not exists

4.3 Elements model in Typhoon HIL Control Center

As mentioned in Chapters 2 and 3, grid-forming inverters are considered enabling elements of modern smart grids and microgrids, therefore, the BESS system is considered a key element for modern systems. In this context, many researchers and companies use simulation software packages to model and investigate potential problems that may occur in microgrids. Likewise, the components of the grid must be properly modeled to correctly reflect the behavior and performance of the system. In fact, for this work, the Typhoon HIL control Center computational tool was used, where a series of storage system models are available. However, the models provided are not detailed models. Finally, in this work, a detailed model of the BESS system is proposed considering the dynamics of the buck/boost converter and the dynamics of the DC-Link capacitor.

4.3.1 (i) Simplified DC-link model - Typhoon HIL

The Schematic Editor library of the Typhoon HIL Control Center computer program provides two models of storage systems, Battery inverter (Switching) and Battery inverter (Average). In fact, the Battery inverter (Switching) model is shown in Figure 4.5.

These available models do not model the switching impact of the buck/boost converters, in fact, the dynamics of the DC link capacitor are also not considered. Finally, this model will be compared with the proposed detailed model, which is presented in the following subsection. Likewise, the impact of these models on the stability and dynamic performance of the microgrid will be analyzed.

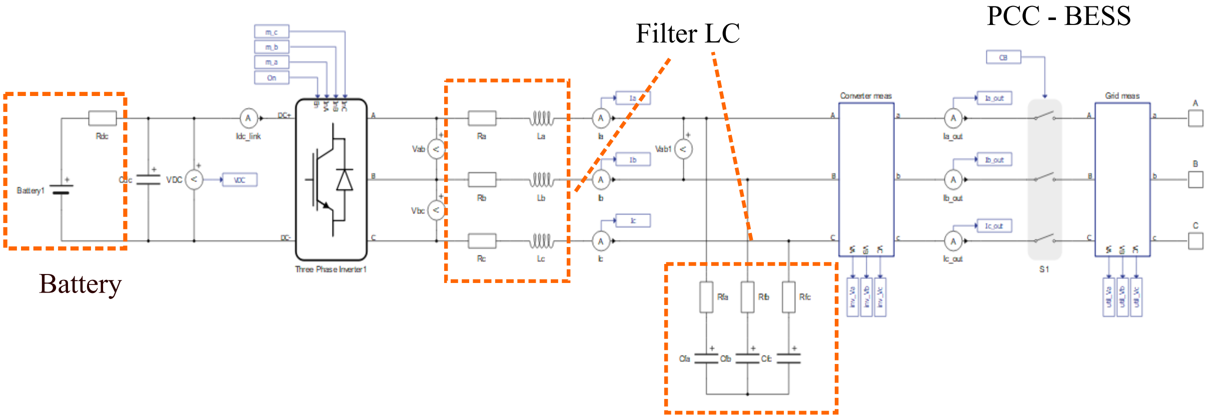

Figure 4.5 – Battery inverter (Switching)

4.3.2 (ii) detailed model - proposed

The proposed detailed model, shown in Figure 4.6, is composed of buck/boost converters, DC link capacitor, and DC /AC inverters. This system will be studied and compared with the model available in the Typhoon HIL library, the impact of the detailed model on the stability and dynamic performance of the microgrid will be analyzed. Likewise, the performance of the proposed model will be studied in different microgrid conditions, such as heavy loads, microgrid transitions to islanded mode.

As shown in Figures 4.6 and 4.7 the control structures of the BESS storage system of a detailed model. The Buck/Boost converter aims to control the voltage of the DC-Link capacitor by charging or discharging correctly. Here PI controllers in cascade are used as seen in Figure 4.7, to maintain the capacitor voltage at a set point, likewise, the second PI controller reacts to changes in inductor current, thus improving the capacity of the Buck/Boost controller to maintain DC-Link voltage. In this work, only the discharge scenario is considered. Finally, Figure 4.6 illustrates the inverter that connects the battery and the Buck/Boost converter to the electrical grid through the LC filter, with control modes that allow the system to operate in parallel with the electrical grid and in islanded mode. Figure 4.7 shows the two states of control of the inverter according to the purpose of the system. In this context, when voltage and reference frequency of the grid is lost, the BESS system provides master controls of voltage and frequency, which is called the GFM control technique. However, if the BESS operates in parallel with the grid, it requires a PLL for synchronization and power supply, this is known as the GFL technique. These control strategies are described in detail in Section 3.

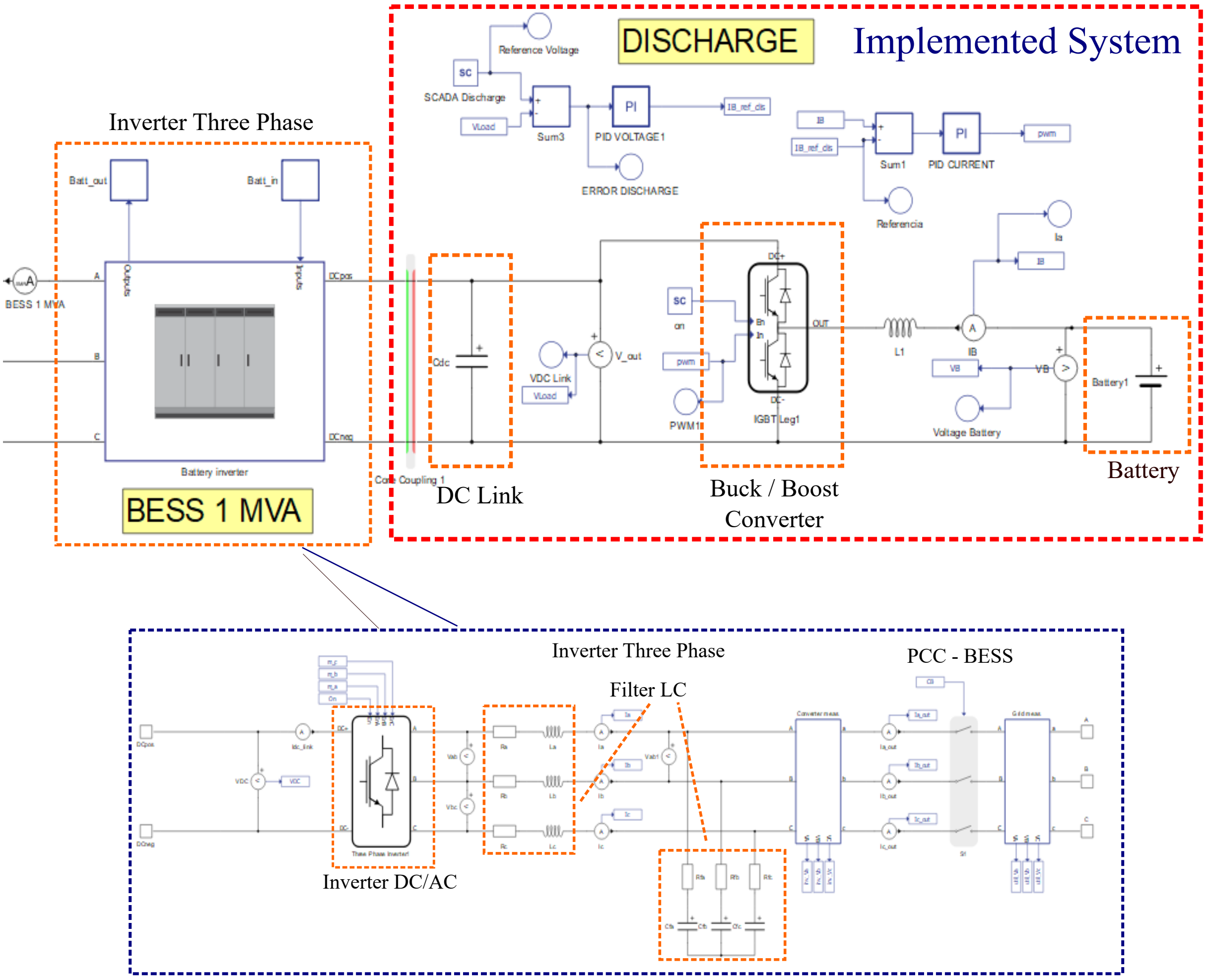

Figure 4.6 – BESS - detailed model

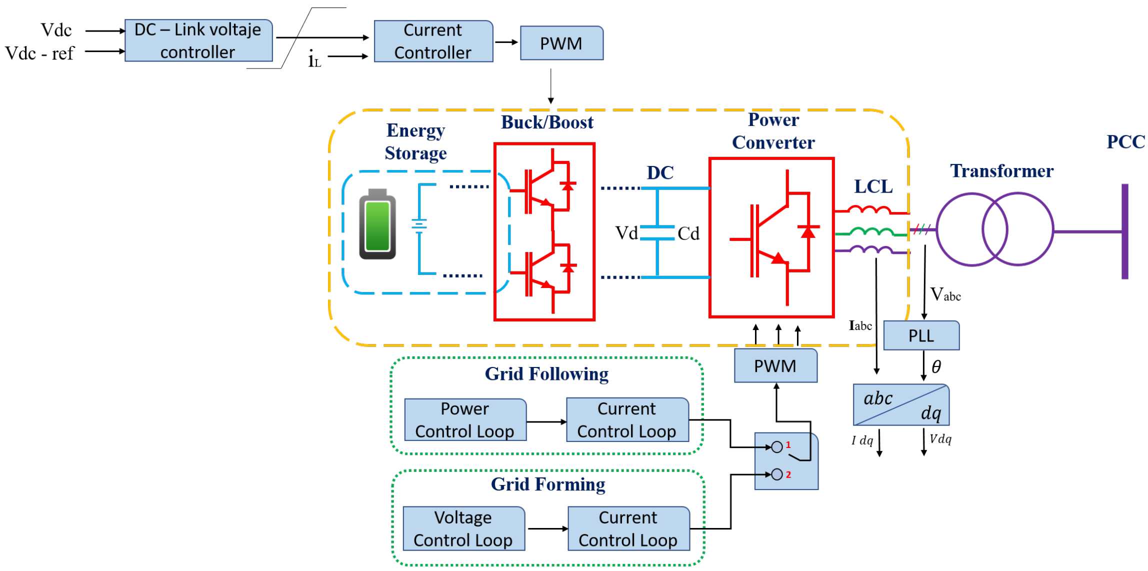

Figure 4.7 – BESS Control Schemes

4.3.3 Photovoltaic system model - Typhoon HIL

The Schematic Editor library block in Typhoon HIL models a PV plant implemented with a two-level, three-phase inverter with a current control loop. The DC link is powered by a constant voltage source, thus simplifying the photovoltaic plant. Irradiance effects are considered by regulating the active power reference accordingly. The photovoltaic plant can operate in voltage or reactive power control mode, as shown in Figure 4.8.

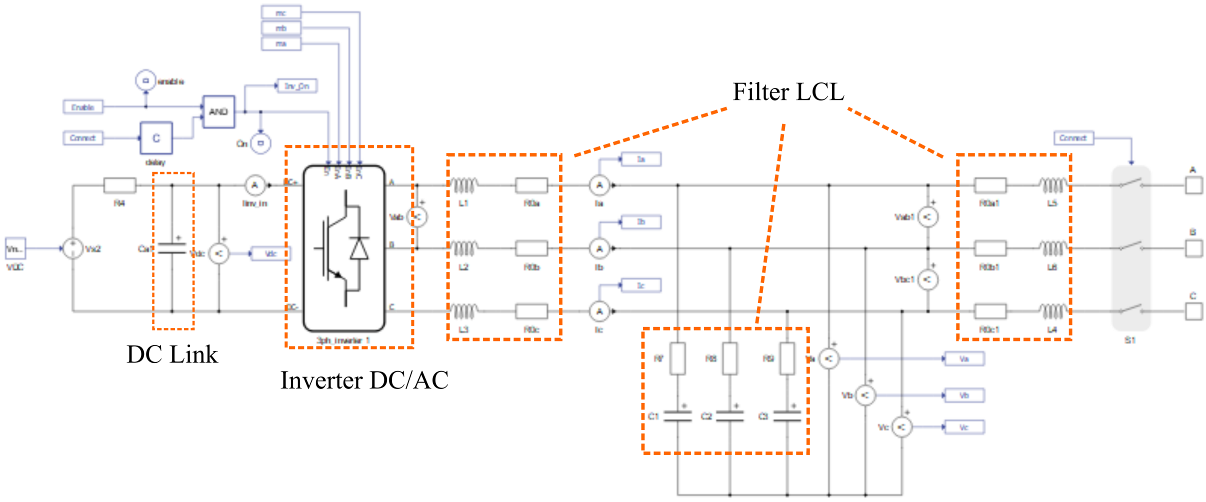

Figure 4.8 – Photovoltaic system model implemented with Typhoon HIL Scheme Editor

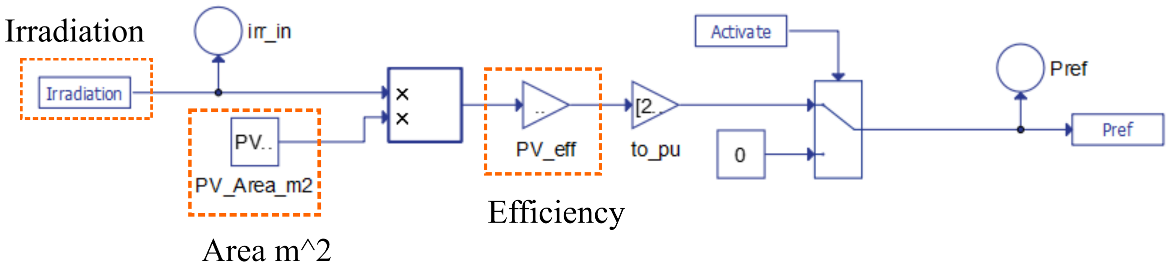

Figure 4.9 – Photovoltaic system - Irradiation

As shown in Figure 4.10, this PV system omits the dynamic part of the Boost converter, as well as the maximum power point tracking (MPPT) controller that establishes reference values of P_{ref} reference active power for the control structures of the three-phase inverter. To emulate the behavior of the Boost converter and the MPPT, it is replaced by the block diagram shown in Figure 4.9. In this context, the shading effects are the result of the variation in incident irradiance of the photovoltaic panels and this is simulated considering the A_{pv} area, η efficiency, and G irradiance comprised by the panels, as shown in Figure 4.9, thus achieving the active power variation as a function of irradiance. Finally, the inverter uses the control technique known as GFL, allowing it to operate in parallel with the grid, being able to participate in the control of the amplitude and frequency

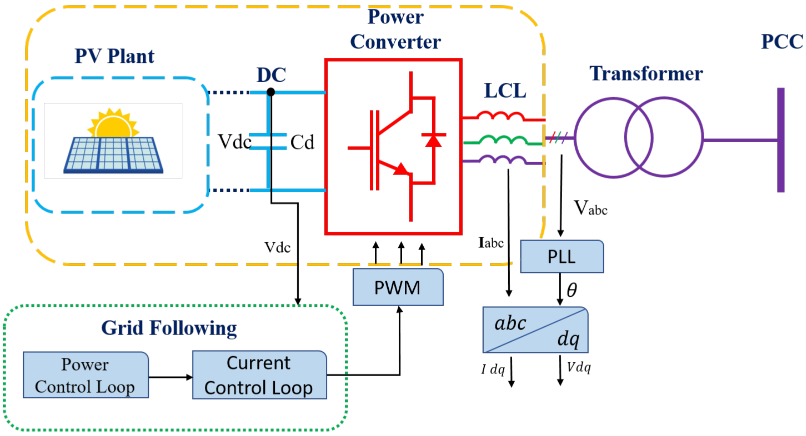

Figure 4.10 – Photovoltaic system Control Scheme

of the microgrid, adjusting the active and reactive power references. This GFL control scheme is explained in detail in Section 3.

4.3.4 Gas Genset model - Typhoon HIL

The Schematic Editor library block in Typhoon HIL models a Gas generator implemented as a synchronous machine with speed and voltage control, shown in Figure 4.11. The speed control is carried out through a Woodward Diesel governor model that governs the dynamics of the engine-governor system, these components are shown in Figure 4.12. Likewise, the voltage is regulated through the excitation system, the model used is IEEE-DC4B. These controls are explained in more detail in Section 3.

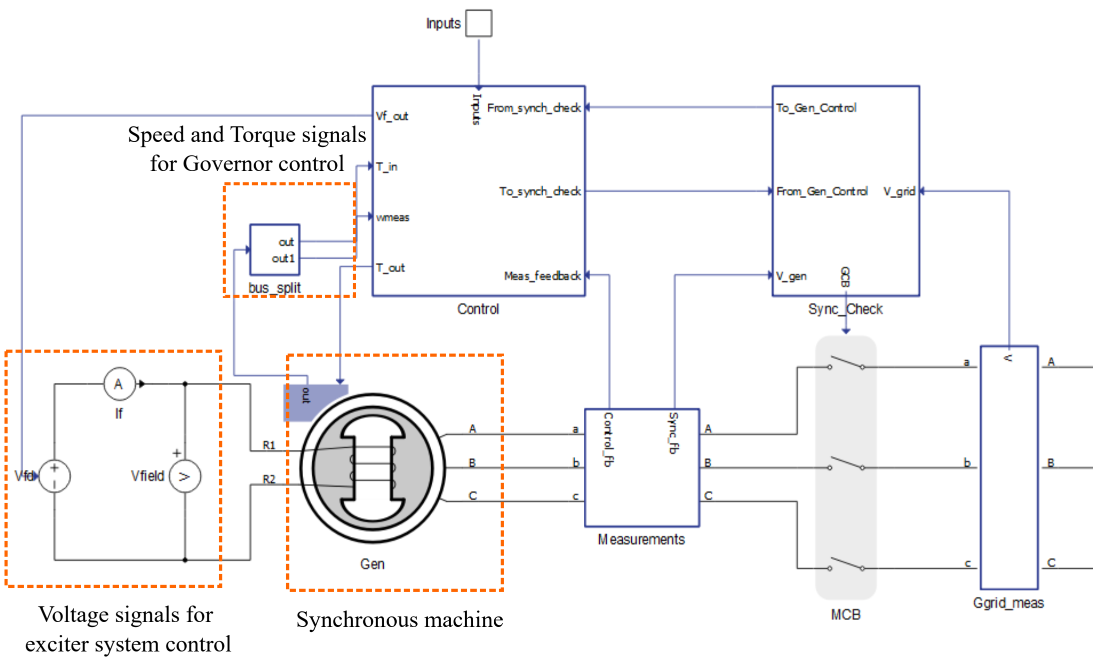

Figure 4.11 – Gas generator implemented with Typhoon HIL Schematic

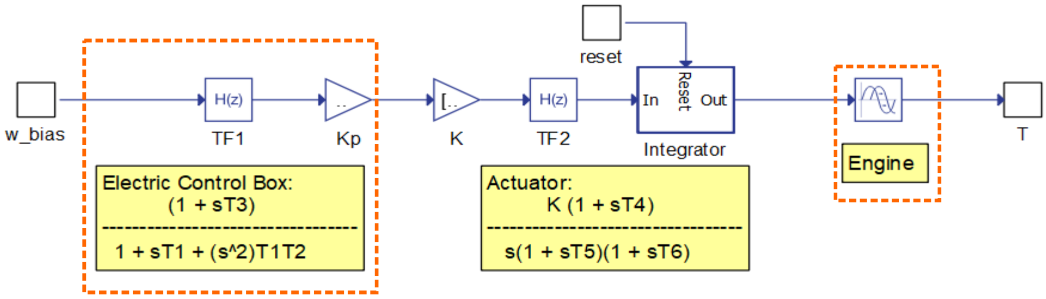

Figure 4.12 – Woodward Diesel governor - typhoon HIL Schematic

4.4 Comments and Conclusions

This chapter showed the characteristics of the CAMPUSGRID microgrid, and their modeling, in the Typhoon HIL Control Center software. Likewise, the control schemes of each of the generation sources that make up the microgrid are also shown. In the following chapter, the results are shown in six scenarios, to see the dynamic behavior of our microgrid, in the face of disturbances.

5 Tests and Results

This chapter presents the results and simulations in the time domain, with the use of the computer program Typhoon HIL Control Center (Typhoon HIL, Typhoon HIL). These simulations aim to (i) verify the performance of the models proposed in the work, (BESS simplified DC Link) and (BESS complete model) (ii) verify the dynamic behavior of the microgrid before, during, and after the islanded mode. Finally, simulations of six cases are performed:

- Case 1: Transition of the microgrid to islanded mode
- Case 2: Resynchronization.
- Case 3: Loss of generation in islanded mode.
- Case 4: Maximum load test in islanded mode.
- Case 5: Loss of BESS system in islanded mode.
- Case 6: Inverter behavior during a phase A to ground fault.

All tests were carried out on a workstation with an Intel(R) Core(TM) i7-8700 CPU with a 3.20 GHz processor and 8 GB of RAM.

5.1 Case 1

The simulations of Case 1 present the transition from the connected mode to the island mode. Likewise, the detection of the islanded microgrid is considered instantaneous. This scenario presents results of the dynamic behavior of the microgrid, using two models of the BESS system (i) simplified DC Link model, (ii) detailed model (proposed).

5.1.1 (i) Simplified DC Link

The Figures 5.1 present the results of the transition from microgrid to islanded mode, considering a simplified BESS model (the dynamics of the buck/boost converter are not considered), likewise, the detection of the island system is instantly considered. Initially, the microgrid operates together with the utility grid, which supplies energy at the demand of 439.54 KW and 240.22 Kvar. At the same time, the BESS system is operating in GFL control mode. Figure 5.1(a), shows the variation of the power of the generation sources of the microgrid, a PV system, and a Gas Genset system. For the verification and analysis of the dynamic performance of the CAMPUSGRID microgrid, the microgrid is intentionally isolated at t = 4.2s, it can be observed that at the instant of the transition 6 Hz oscillations are produced, which are quickly damped, they are caused by the presence of the synchronous machine of the Gas Genset, likewise, these oscillations are reflected in the voltage and frequency at the PCC point, shown in Figure 5.1. Likewise, both the frequency and voltage in PCC Figure 5.1 (b) and (c) can be observed, they return to their reference values after islanded microgrid. The frequency at the PCC point varies between 59.8 Hz and 60.1 Hz. The voltage varies between 0.94 p.u and 1.02 p.u, these ranges are within the minimum requirements of the standard (IEEE. . . , 2018). In fact, at the instant of the transition from the microgrid to islanded mode, the control structure of the BESS system changes from GFL to GFM, allowing the operation of the microgrid in islanded mode. Figure 5.1 (d) shows the currents of the BESS system, initially operating with GFL control mode, without supplying power, at the instant of transition to isolated mode, it is instantly detected and changes to GFM control mode, instantly supplies power to the microgrid.

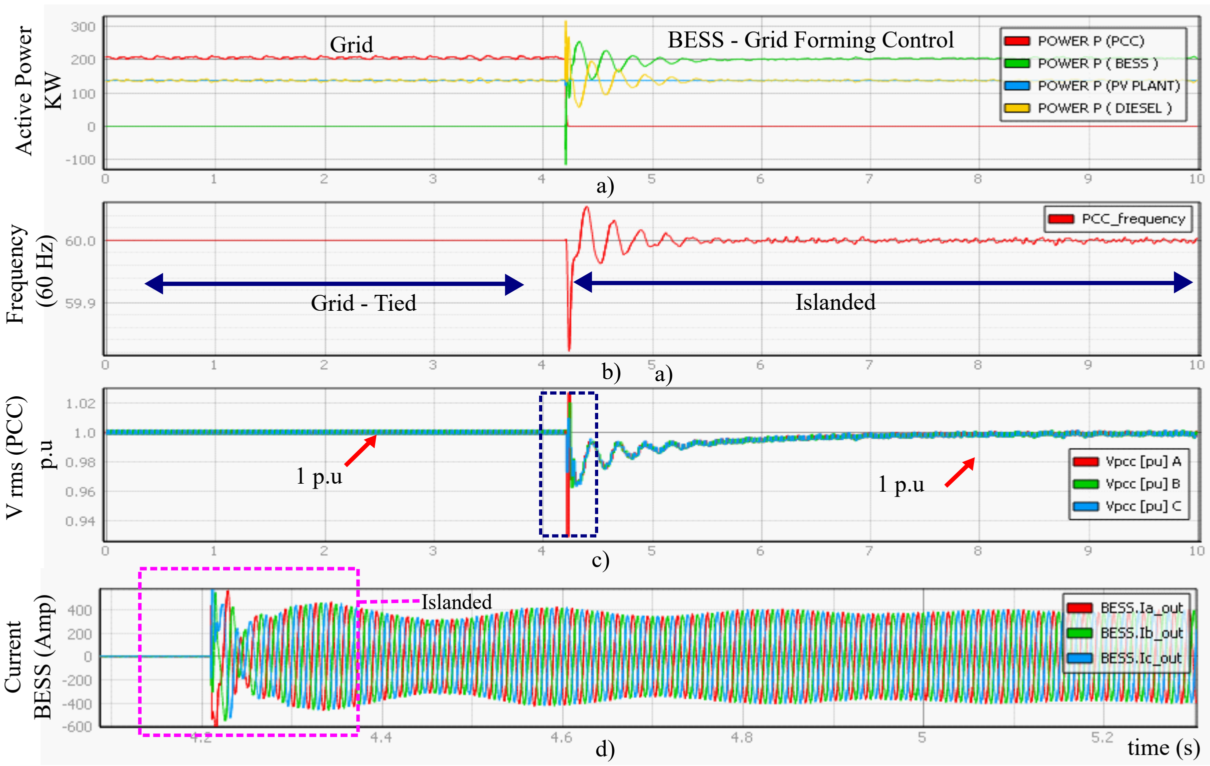

Figure 5.1 – Resulting for microgrid islanding a) Active Power (KW), b) Frequency in PCC (Hz), c) voltage in PCC (p.u), and d) Current of BESS

5.1.2 (ii) Detailed model

Figure 5.2 presents the results of the microgrid transition to islanded mode, considering a detailed model of the BESS system. Figure 5.2 (a) shows that the system initially operates with two Gas Genset, and a BESS system. Likewise, intentional islanded of the CAMPUSGRID microgrid is carried out at t = 3.1s. Observing in Figure 5.2 (d) the current of the BESS system, where it is seen that initially, the BESS system is operating in GFL mode without supplying energy to the grid, occurs at islanded of the microgrid in t = 3.1s, instantly the BESS system changes to the control mode to GFM, enabling the operation of the microgrid in islanded mode, likewise, the beginning of the BESS system current is distorted, due to the damped oscillations (6Hz) produced by synchronous machines. Figures 5.2 (a) and (b) show the variations in voltage and frequency at the moment of island of the CAMPUSGRID microgrid, these vary between 1.1p.u to 0.95 p.u in voltage, and 60Hz to 59.7Hz in frequency. These transient values are within the minimum requirements according to the standard (IEEE. . . , 2018). In fact, the microgrid remains stable, as well as the grid forming control of the BESS system manages to keep the microgrid stable in the event of a transition.

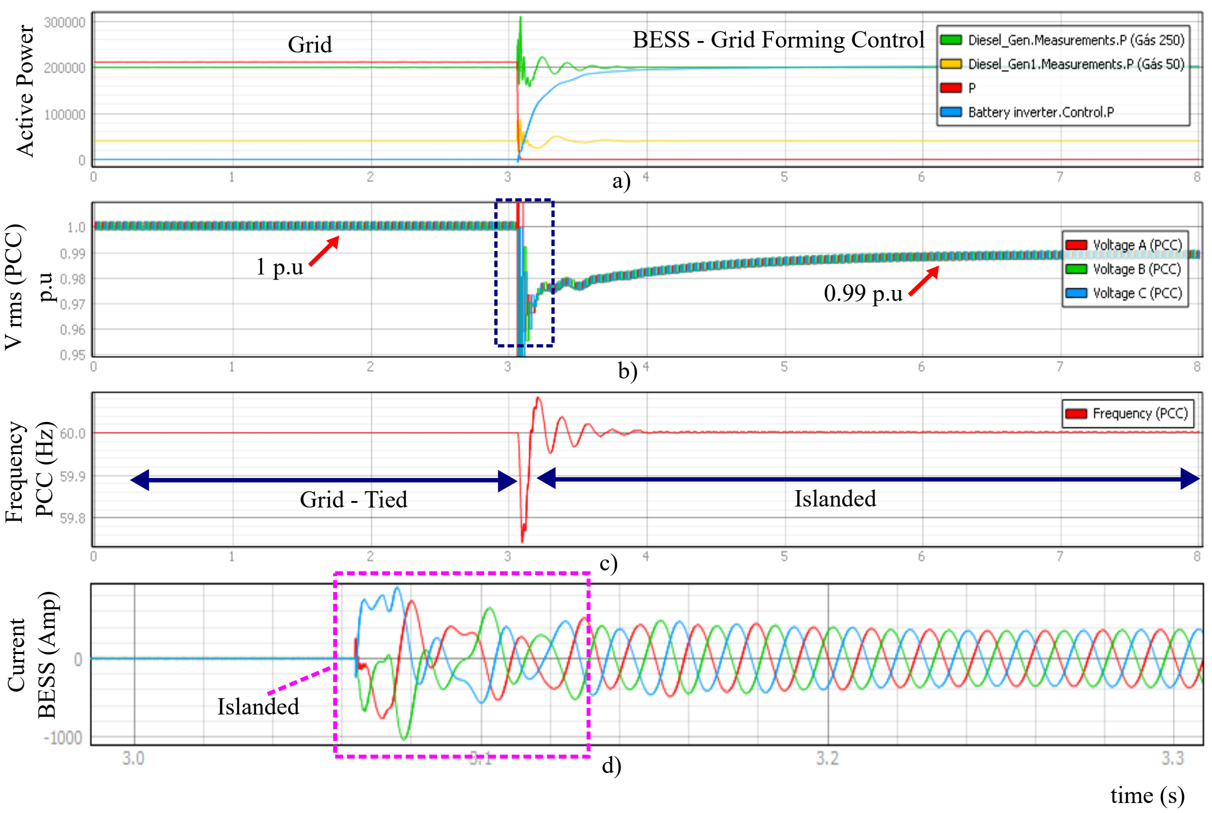

Figure 5.2 – Resulting for microgrid islanding - BESS + Gas Generator a) Active Power (W), b) voltage in PCC (p.u), c) Frequency in PCC (Hz), and d) Current of BESS (Amp)

Figure 5.3 shows the behavior of the BESS system battery. In fact, the battery system is capable of increasing its current, once it detects the disconnection from the grid in connected mode. The current increases from 0 A to 480 A and the voltage drops from 875 V to 870 V. Also, an oscillation can be seen in the transition from microgrid to islanded mode. This happens because the system is working together with two Gas Genset. Likewise, Figure 5.3 (c) shows the state of charge of the battery, where it is observed that

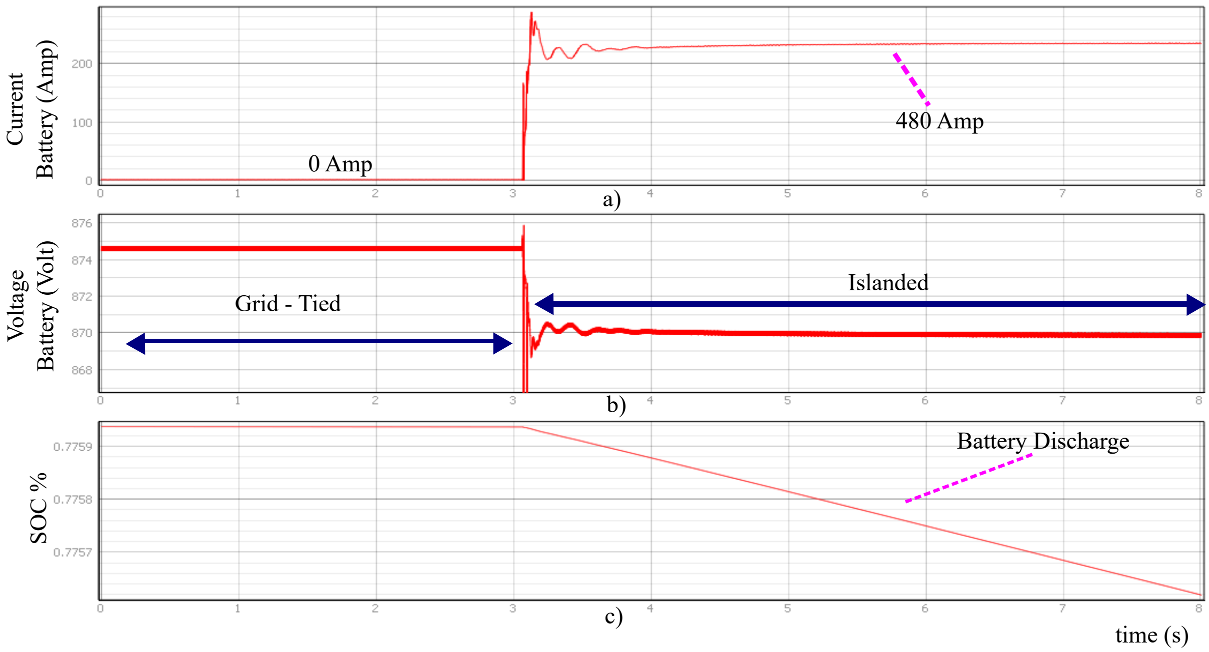

Figure 5.3 – Resulting for microgrid islanding - BESS + Gas Generator a) Current Battery (Amp), b) Voltage Battery in PCC (Volt), and c) State of Charge (%).

initially it is in standby without discharging, once it changes to the GFM control mode, the battery begins to discharge, supplying energy to the islanded microgrid.

5.2 Case 2

The simulations of Case 2 present the resynchronization of the microgrid with the utility grid. Initially, the microgrid operates in islanded mode, with a BESS operating in GFM control mode. Likewise, the results of the dynamic behavior of the microgrid are presented using two models of the BESS system (i) simplified DC Link model, (ii) detailed model (proposed).

5.2.1 (i) Simplified DC Link

In this scenario, the microgrid initially operates in islanded mode, with a BESS system in grid forming control mode. Also, the model used for the BESS is (Simplified DC Link). In this context, the BESS system (300KW), Gas Genset (200KW) ,and PV system (200KW) are supplying energy to the load (islanded microgrid) of 750 KVA balanced in the three phases, with a power factor of 0, 9. At t = 3.9s, the synchronization of the microgrid to the utility grid is carried out, likewise it is considered that the detection is instantaneous and the closing time of the switch is not considered. With these conditions, it is observed in Figure 5.4 (a), the powers of the generation sources of the microgrid, likewise, the oscillation (7 Hz) in the synchronous machine at the time of synchronization with the utility grid is shown. The oscillations caused by the synchronous machine at the time of resynchronization are not reflected in the voltage in the PCC Figure 5.4 (b), this is because now the frequency and voltage signals are supplied by the conventional network (robust system in frequency and voltage).

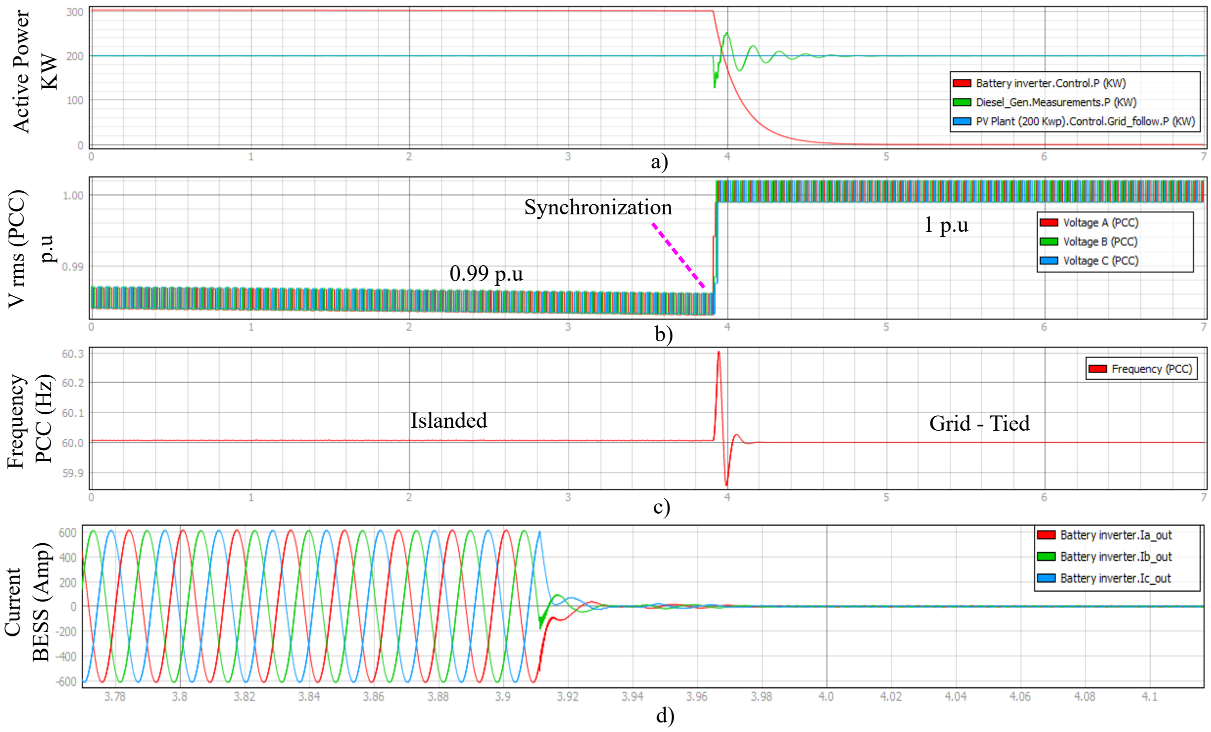

Figure 5.4 – Resynchronization only BESS a) Active Power (KW), b) voltage in PCC (p.u), c) Frequency in PCC (Hz), and d) Current of BESS (Amp).

5.2.2 (ii) Detailed model

In this case, the Gas Genset are providing 200 kW and 40 kW of active power, respectively, likewise, the BESS system provides 200 kW. These generation sources are operating together in islanded mode with a GFM control structure provided by BESS. The system load is 440 kW of active power, balanced in all three phases. At t = 3.28s, the grid re-connection process occurs, assuming that the grid returned after some event (blackout) occurs, synchronization with the grid is assumed to be instantaneous, therefore the breaker closing time in the PCC is not considered. According to Figure 5.5 (b), initially, the RMS voltage at the PCC point is 0.99 p.u, it returns to 1 p.u once it is synchronized with the conventional network. Likewise, Figure 5.5 (c) shows the system frequency at the moment of synchronization with the network, varying between 60.25 Hz and 59.8 Hz. However, Figure 5.5 (a) shows oscillation (6Hz) in the powers of the Gas Genset systems in the re-synchronization with the network, but this is not reflected in voltage and frequency at the PCC point, because these two variables are no longer provided by the BESS system, instead, it is supplied by the utility grid (robust system in frequency and voltage).

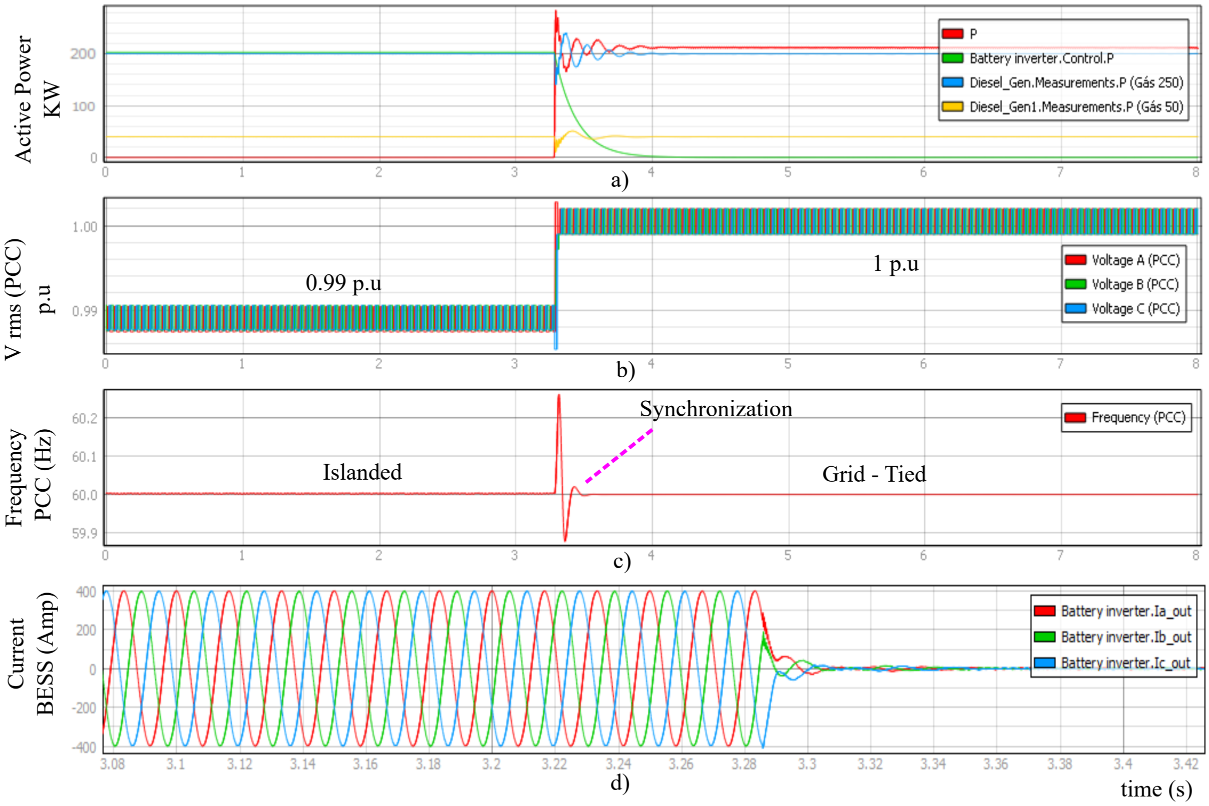

Figure 5.5 – Resynchronization BESS + Gas Generator a) Active Power (KW), b) voltage in PCC (p.u), c) Frequency in PCC (Hz), and d) Current of BESS (Amp).

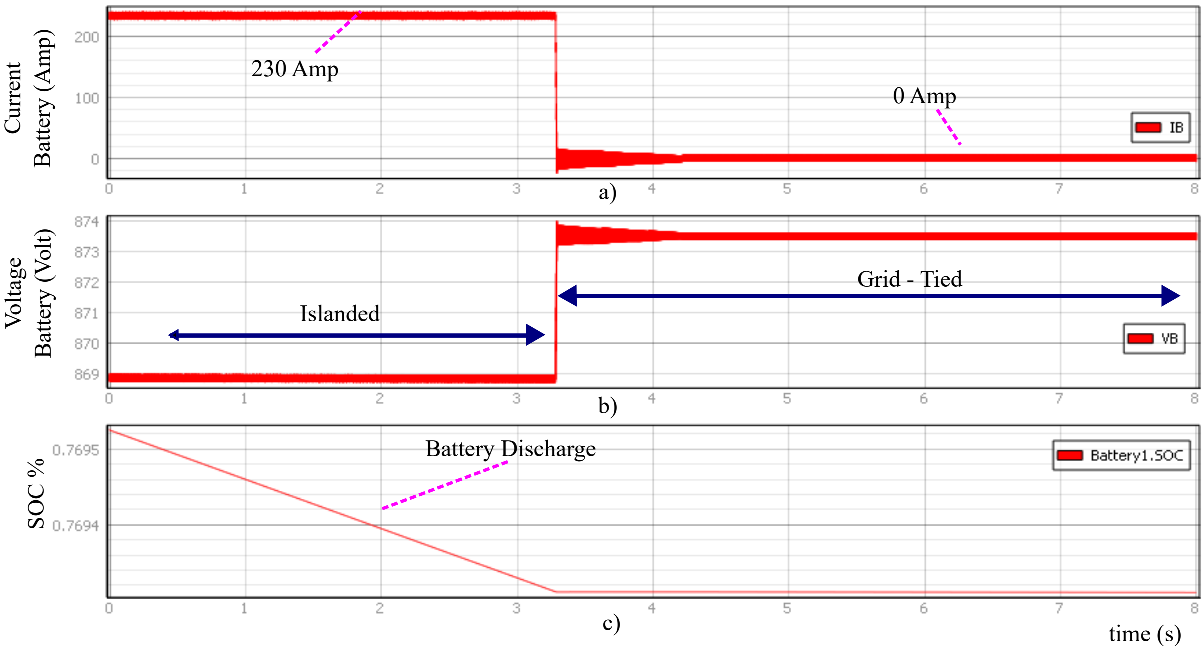

Figure 5.6 – Resynchronization BESS + Gas Generator a) Current Battery (Amp), b) Voltage Battery in PCC (Volt), and c) State of Charge (%).

The BESS system is the master frequency and voltage controller, with the GFM control scheme in the islanded microgrid. In this context, Figure 5.6 shows the behavior of the battery, in the process of reconnection to the utility grid. According to

Figure 5.6 (a), it is initially observed that the current supplied by the battery is 230 A (GFM) and changes to 0 A (GFL), at t = 3.28 s, time in which the reconnection is made. Likewise, Figure 5.6 (c) shows the state of charge of the battery (SOC %), the discharge of the battery is observed initially. At t = 3.28 s resynchronization occurs and the state of charge (SOC%) of the battery changes to standby (SOC% constant). Likewise, the resynchronization process with the grid was a smooth process without producing any oscillation in the battery.

5.3 Case 3

The simulations in Case 3 present the loss of the Gas Genset ,and photovoltaic system, operating the microgrid in islanded mode. Also, the BESS operates as a GFM control. In this case, results of the dynamic behavior of the BESS system are presented (i) simplified DC Link model, (ii) detailed model (proposed). The objective of this Case is to observe the behavior of the BESS system, when it operates at its nominal value. In this context, the operation of all photovoltaic systems and Gas Genset in the microgrid is not considered. The generation systems used are located in the CAMPUSGRID at nodes 11, 18, and 08, as shown in Figure 4.3.

5.3.1 (i) Simplified DC Link

In this case, the microgrid is operating in islanded mode, with a BESS system operating in GFM mode, enabling the operation of the microgrid in the islanded mode. Likewise, the Gas Genset and photovoltaic system are connected, generating an active power of 200 kw and 200 kwp respectively. The demand for the microgrid is 935 kw of active power and 450 kva of reactive power. Figure 5.7 illustrates the dynamic behavior of the BESS system, with a simplified DC link model. Initially, the microgrid operates in islanded mode, at t = 4.5 s Gas Genset is disconnected, and the demand is quickly supplied by the BESS system, in the same way at t = 5.9 s photovoltaic generation is disconnected, leaving only the BESS system operating. The BESS system manages to keep the microgrid stable, after a scenario of interruption and failure of components of the microgrid generation systems. Voltage and frequency of the microgrid during shutdown of generation sources drop from 1 p.u to 0.98 p.u as well as the frequency from 1 p.u to 0.994 p.u can be observed in Figures 5.7 (a) and (b). Likewise, the BESS system quickly returns to the initial conditions. The system remains stable for the simplified DC-link model, without showing any type of oscillations due to disturbances caused by the output of the Gas Genset, and the photovoltaic system.

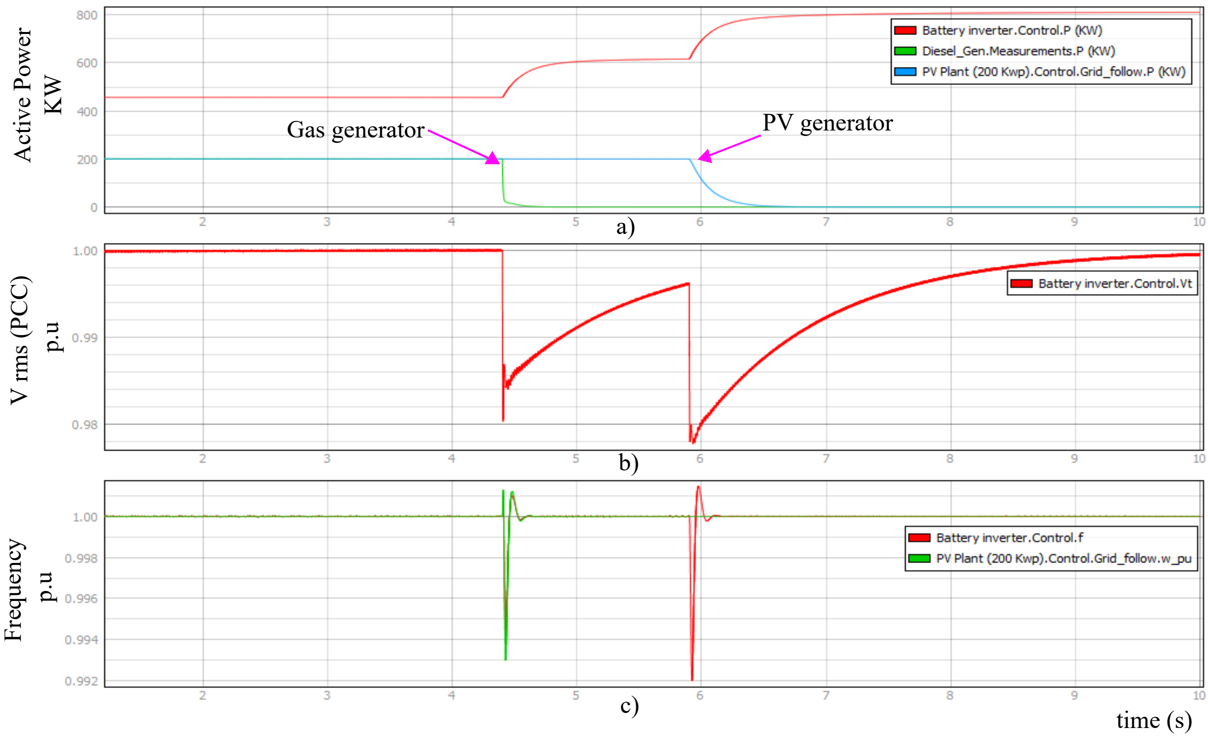

Figure 5.7 – Islanded microgrid a) Active power (KW), b) Voltage rms PCC (p.u) y c) Frequency PCC (p.u)

5.3.2 (ii) Detailed model

In this scenario, the microgrid operates in islanded mode, together with the photovoltaic and Gas Genset. Likewise, a storage system is considered with a detailed model, with the dynamics of the buck/boost converters and the DC link capacitor. In this context, the BESS system operates with the GFM control mode. Figure 5.8 (a), shows the active power of the generation sources in KW, at t = 2.9 s the Gas Genset is disconnected, and the BESS system supplies the demand. Figure 5.8 (b) shows the microgrid voltage drops, but it is quickly recovered by the BESS system and is returned to its reference values, likewise, a small variation is shown without any effect on the frequency. However, at t = 4.5 s the photovoltaic generation is disconnected, the microgrid voltage drops to 0.97 p.u, likewise, the BESS system manages to keep the microgrid stable. However, the system shows oscillations in frequency and voltage for the model detailed. In fact, the most pronounced oscillations are reflected in the voltage, this is because as the power demand increases, the discharge current of the battery and the DC link capacitor also increases, exceeding a certain value, reflecting in non-sustained voltage ripples, which could lead the microgrid to instability, if more demand continues to increase, taking the BESS system to its nominal values. Figure 5.9 shows the dynamic behavior of the DC link of the storage system, based on the detailed model.

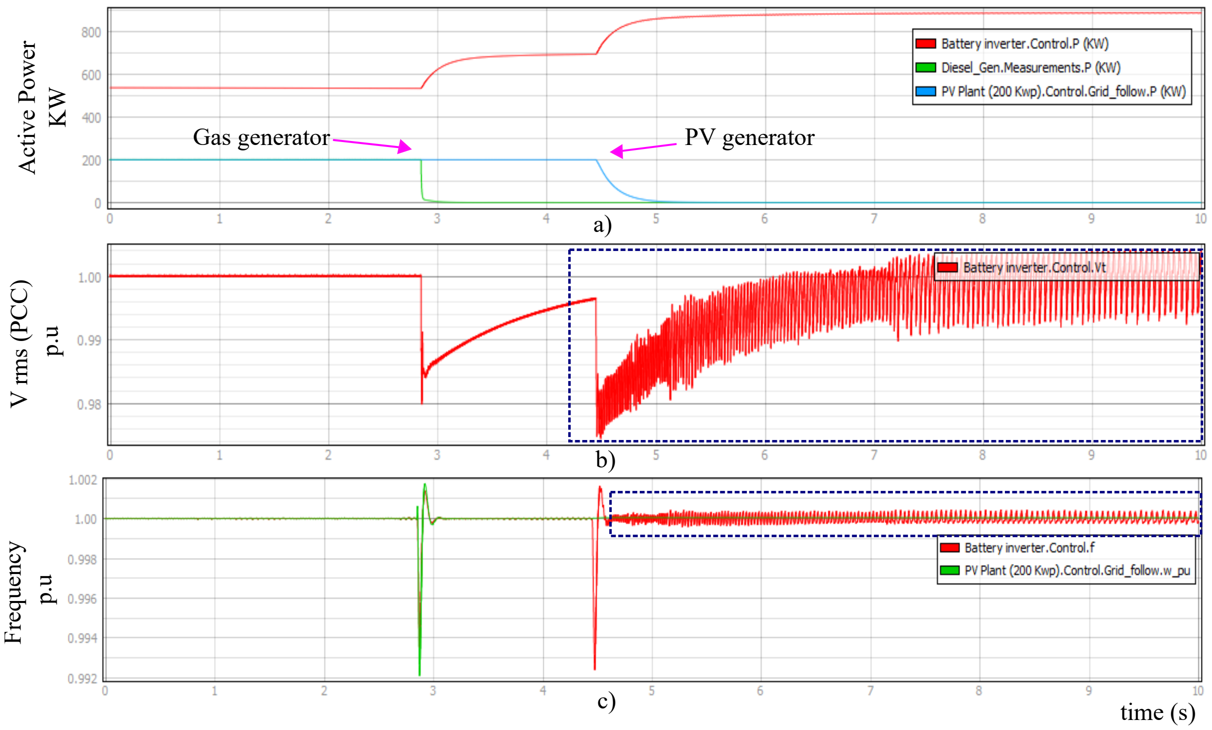

Figure 5.8 – Islanded microgrid a) Active power (KW), b) Voltage rms PCC (p.u) y c) Frequency PCC (p.u).

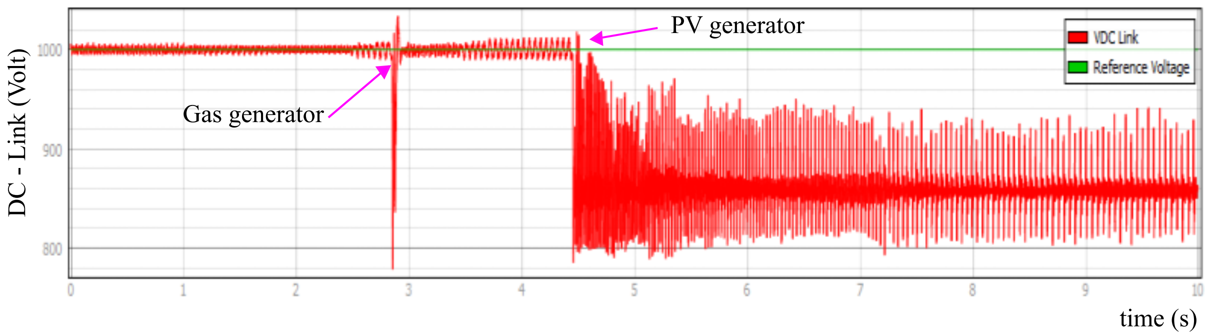

Figure 5.9 – DC-link voltage for the detailed model.

5.4 Case 4

The simulations of Case 4 present a maximum load test, with the microgrid operating in isolated mode. Likewise, the BESS system operates in GFM mode. The system initially operates with a demand of 780 kW of active power and 380 kvar of reactive power, with a balanced load in all three phases. The microgrid is brought to its maximum load, thus load is supplied up to the maximum demand of 1100 KVA of power, with a power factor of 0.9. In this context, the results of the dynamic behavior of the BESS system (i) simplified DC-link model and (ii) detailed model are presented.

5.4.1 (i) Simplified DC-link model

Initially, the microgrid operates in islanded mode with a simplified BESS system model (the buck/boost converter dynamics are not considered). Figure 5.10 shows the variation of the active power demand in KW, as well as the voltage and frequency of the system. Initially, it is observed that the BESS system supplies a demand of 780 kW of active power and 380 kvar of reactive power. The demand increases progressively up to its nominal value in t = 5 s (1MVA, with a power factor 0.9), in t = 11 s the demand increases by 10% more than the nominal capacity of the BESS system, reaching the demand in 1.1 MVA with a power factor of 0.9. In fact, it can be seen that the system frequency and voltage have small oscillations without much impact on the microgrid shown in Figure 5.10 (b) and (c). Finally, as seen in these Figures 5.10(a), (b), and (c), the system can maintain its stability for the simplified BESS DC-link models when it is subjected to an overload of 10% of its rated power.

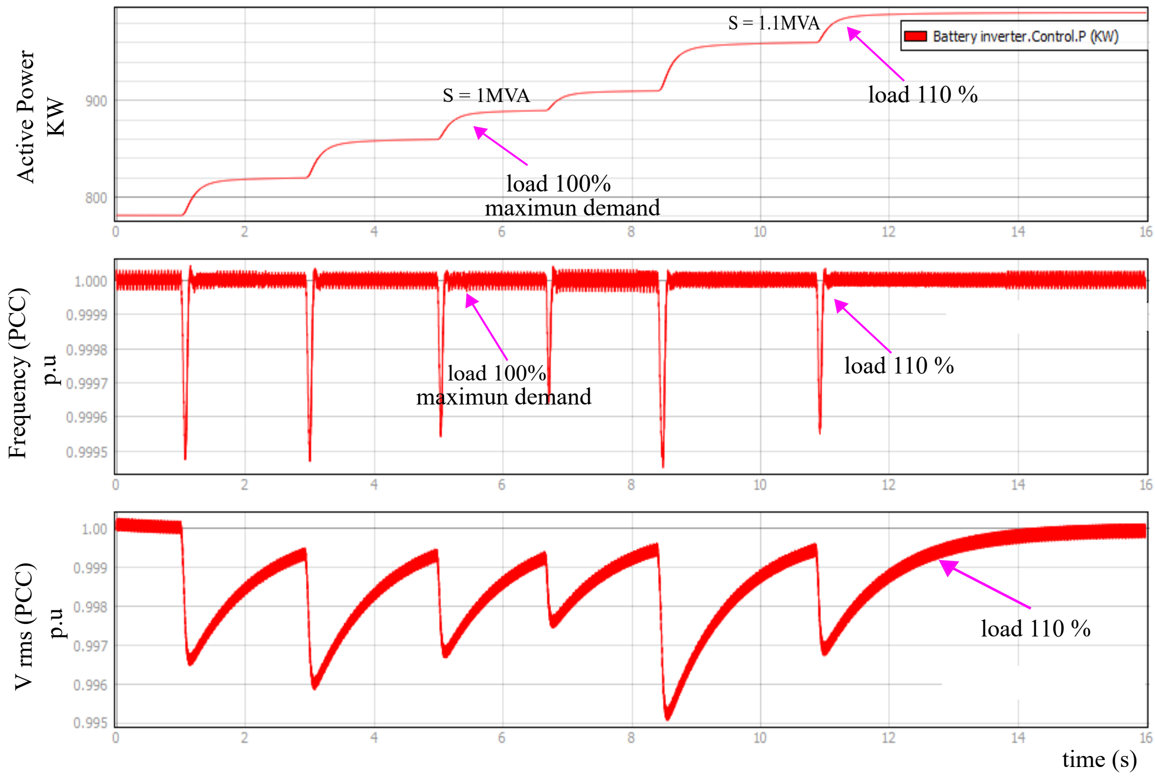

Figure 5.10 – Islanded microgrid a) Active power (KW), b) Frequency PCC (p.u) y c) Voltage rms PCC (p.u)

5.4.2 (ii) Detailed mode

In this scenario, the microgrid initially operates in isolated mode, with a detailed BESS model. In this context, the microgrid has a demand of 780 KW and 380 kVAr, at t = 1.9 s the demand increases to 100% (1MVA with power factor pf = 0.9), it is observed in Figure 5.11 (b) and (c) small oscillations in the voltage and frequency of the microgrid.

At t = 9 s, the demand increases a further 10%, reaching 1.1 MVA with pf = 0.9. In this context, the BESS system operates with an overload of 10% of its nominal value, at t= 9.5 s the BESS system fails to maintain the demand, having an abrupt voltage drop at 0.4 p.u (Figure 5.11 (c)), consequently, the BESS system does not can satisfy the demand 110% and the system collapses at t = 11 s. Because the battery has to increase its power generation and has limited discharge current capacity, the DC link capacitor voltage cannot maintain its voltage, which reflects in non-sustained oscillations in the battery and reflected in the variables of the microgrid system.

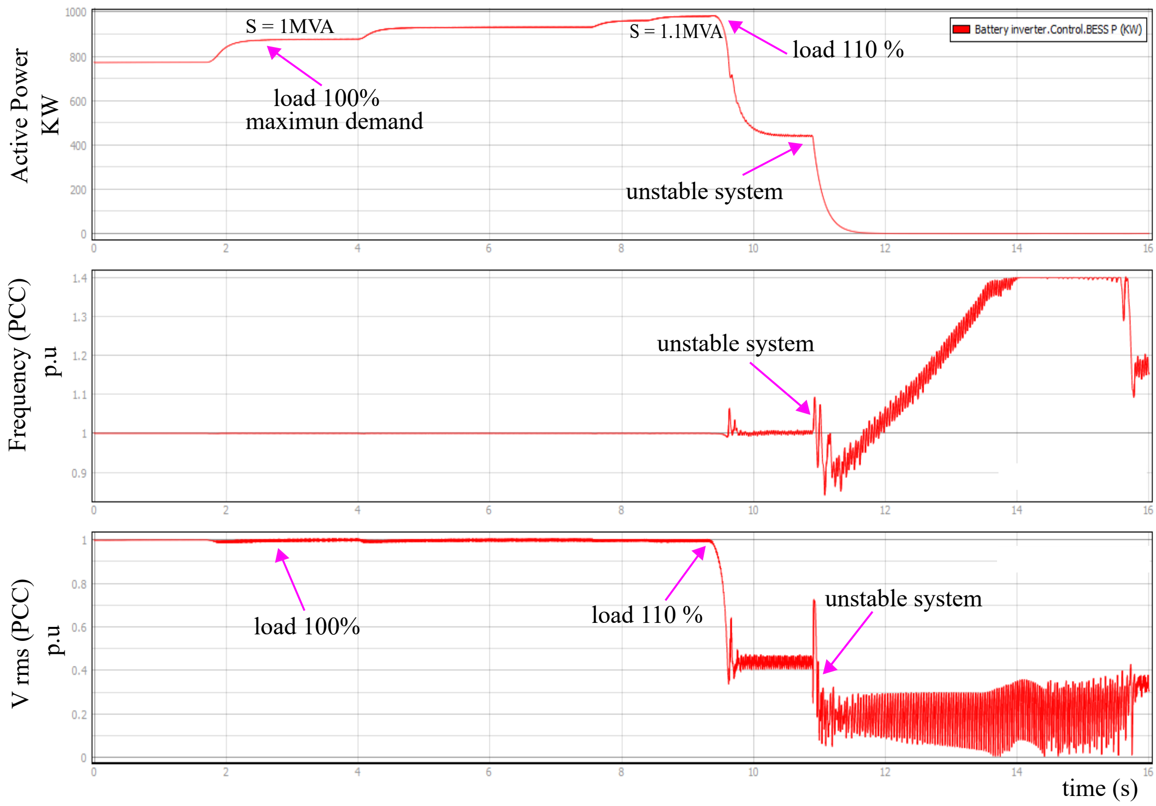

Figure 5.11 – Islanded microgrid a) Active power (KW), b) Frequency PCC (p.u) y c) Voltage rms PCC (p.u)

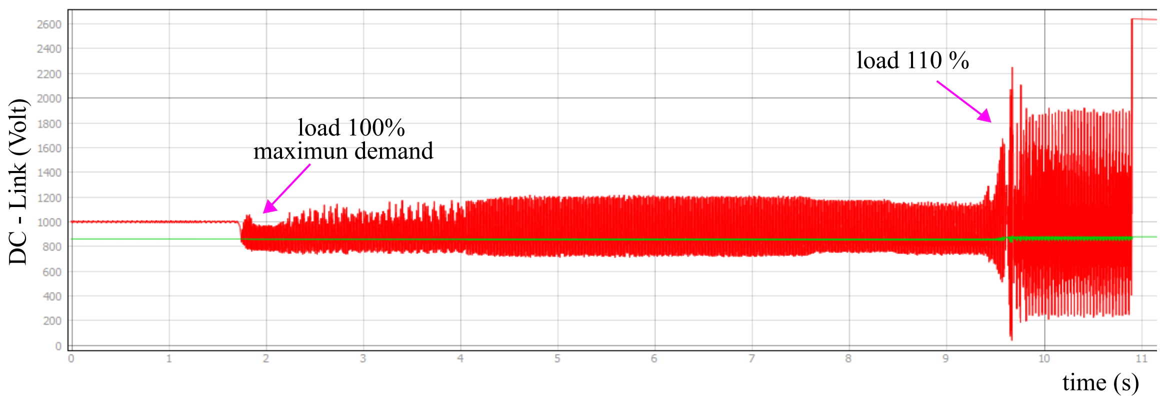

Figure 5.12 – DC-link voltage for the detailed model

Figure 5.12 shows the dynamic behavior of the DC link capacitor, likewise, it can be seen that as the demand increases, the DC capacitor link discharge current also increases, and when the demand exceeds after 100%, the DC link capacitor voltage ripple becomes significant, leading to instability of the microgrid.

5.5 Case 5

Case 5 presents the dynamic behavior of the microgrid operating in islanded mode, when losing the BESS system operating in GFM mode. In fact, the system works 100% based on inverters, made up of five photovoltaic systems and one BESS system.

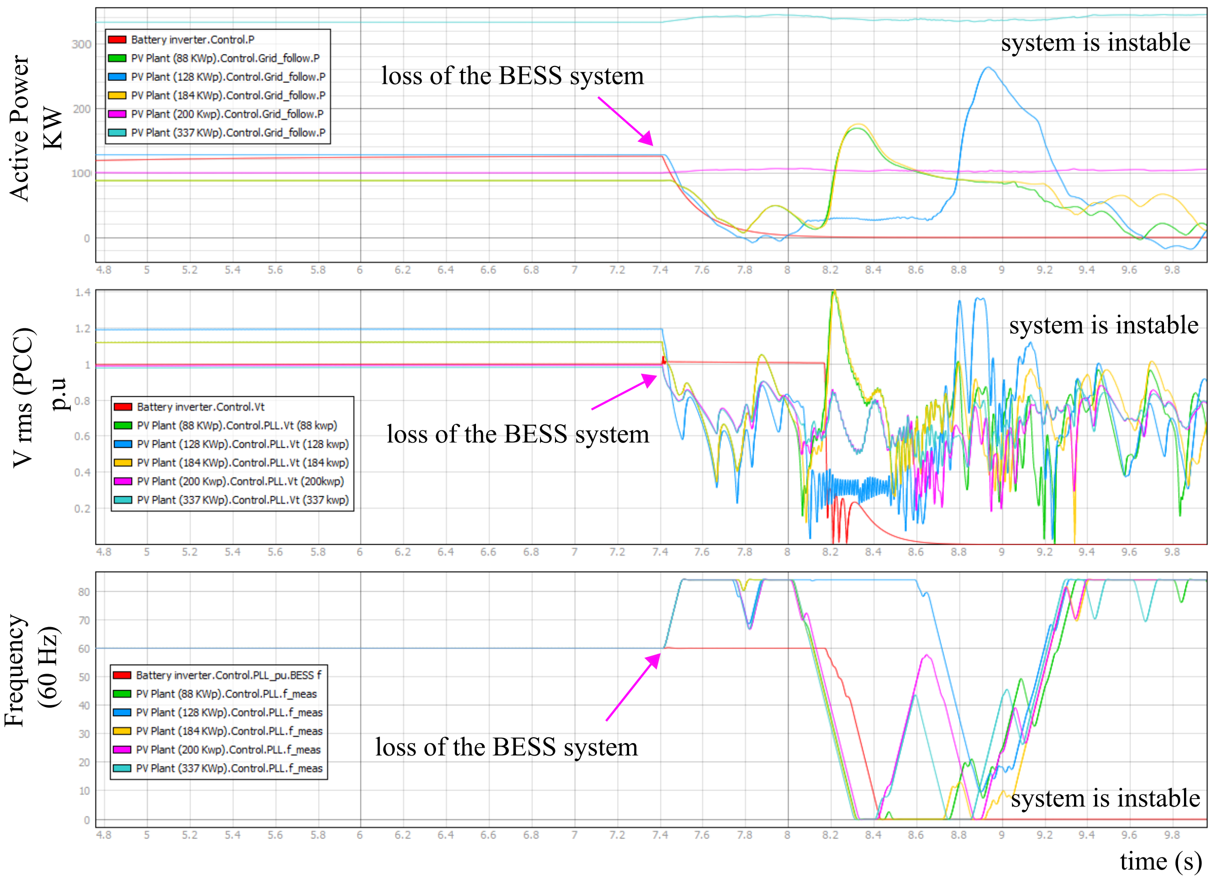

Figure 5.13 – Islanded microgrid a) Active power (KW), c) Voltage rms (p.u), y C) Frequency (Hz).

In this scenario, the microgrid is shown operating in islanded mode with 100% IBRs. The generation sources are assembled of one BESS system that operates in GFM mode and five photovoltaic systems that operate in GFL mode. The microgrid has a demand of 1000 KVA with a power factor of 0.9, balanced in the three phases. As shown in Figure 5.13, the demand is mainly supplied by photovoltaic sources, all of them operating in GFL control mode. At t = 7.4 s, the BESS system is disconnected, and the photovoltaic generation sources with GFL control mode, lose stability instantly, caused by the loss of frequency and angle reference of the grid forming system (BESS).

5.6 Case 6

In this scenario, single-phase short-circuit tests are carried out in (i) connected to the network, and (ii) islanded mode. In node 9 of the CAMPUSGRID microgrid (Figure 4.3), the fault in phase A is applied to ground, in order to analyze the behavior of the IBRs.

5.6.1 (i) Microgrid connected to the network

In this scenario, the microgrid is operating and connected to the utility grid. The IBRs are operating with the GFL control mode, and a single-phase short circuit test is performed on phase A to ground (fault applied node 9 Figure 4.3). Figures 5.14, and 5.15 show the behavior of the BESS system and the five photovoltaic systems. The 1MVA capacity BESS system, at 480V, has a current limit of 1.2 p.u, or a maximum of 600A during a short circuit, and returns to 170A after the fault is cleared, shown in Figure 5.14 (b). In the same way, the short-circuit current capacity of photovoltaic systems is 1.1 p.u. of its rated current. The contribution of short-circuit current in IBRs systems is minimal compared to traditional generation sources based on synchronous machines. Note*: BESS is initially supplying 100 kW and 100 kvar of its active and reactive power, respectively, which is reflected in its current.

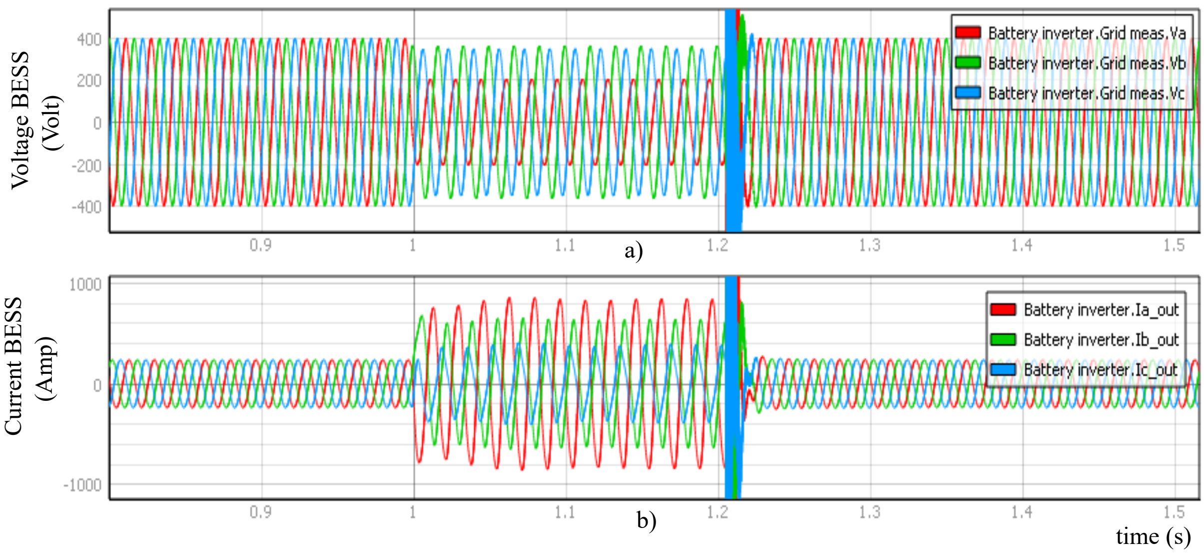

Figure 5.14 – Inverter behavior during a phase A to ground fault. a) BESS - Grid following inverter voltage, b) BESS - Grid following inverter current.

5.6.2 (ii) Islanded microgrid

In this scenario, the microgrid is operating in islanded mode, with 100% IBRs generation sources, five photovoltaic systems operating with the GFL control structure, while the BESS system is the master voltage and frequency controller (GFM), enabling the

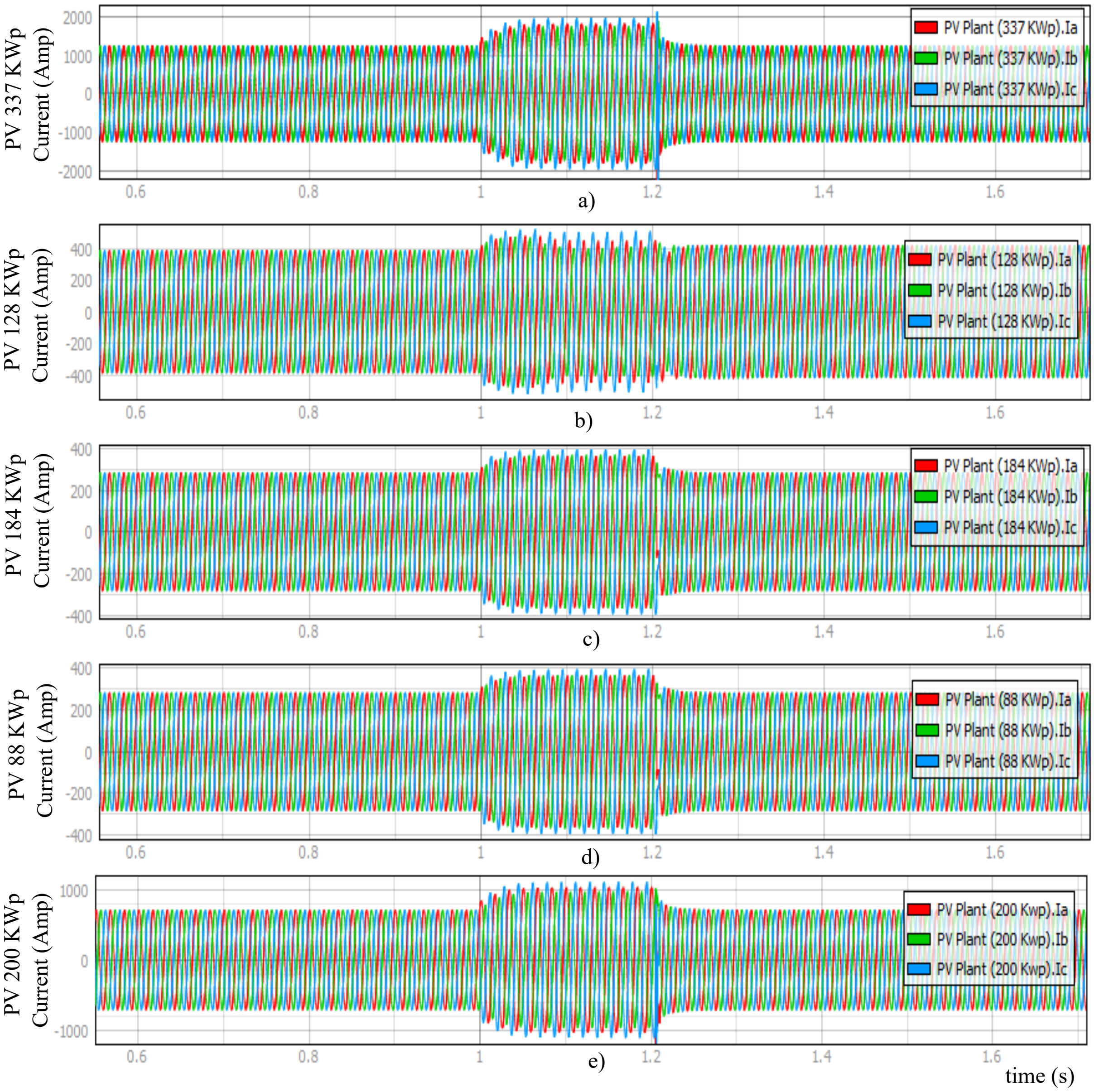

Figure 5.15 – Inverter behavior during a phase A to ground fault. a) PV 337 KWp - Grid following inverter output current, b) PV 128 KWp - Grid following inverter output current, c) PV 184 KWp - Grid following inverter output current, d) PV 88 KWp - Grid following inverter output current y e) PV 200 KWp - Grid following inverter output current.

islanded mode operation. A test single-phase short-circuit is applied on phase A to ground, at node 9 shown in Figure 4.3, the applied fault is 20 ms, starts at t= 0.5 s and clears at t = 0.7 s. Figures 5.16 and 5.17 show that the short circuit current contribution in IBRs is zero. This is due to the fact that the microgrid transformers have a delta connection in medium voltage (MV) and a star connection in low voltage (fault is applied in MV node 9), the microgrid is left without reference to ground in islanded mode, causing the protection systems cannot detect it.

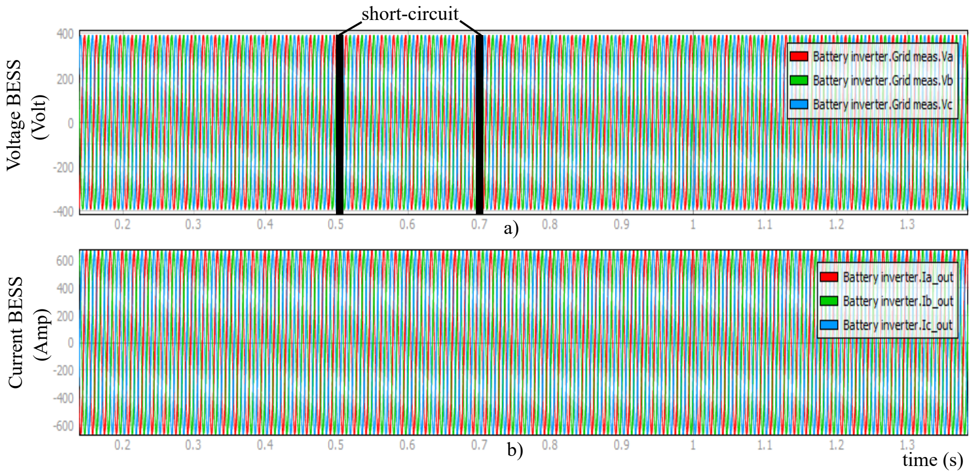

Figure 5.16 – Inverter behavior during a phase A to ground fault. a) BESS - Grid forming inverter voltage, b) BESS - Grid forming current.

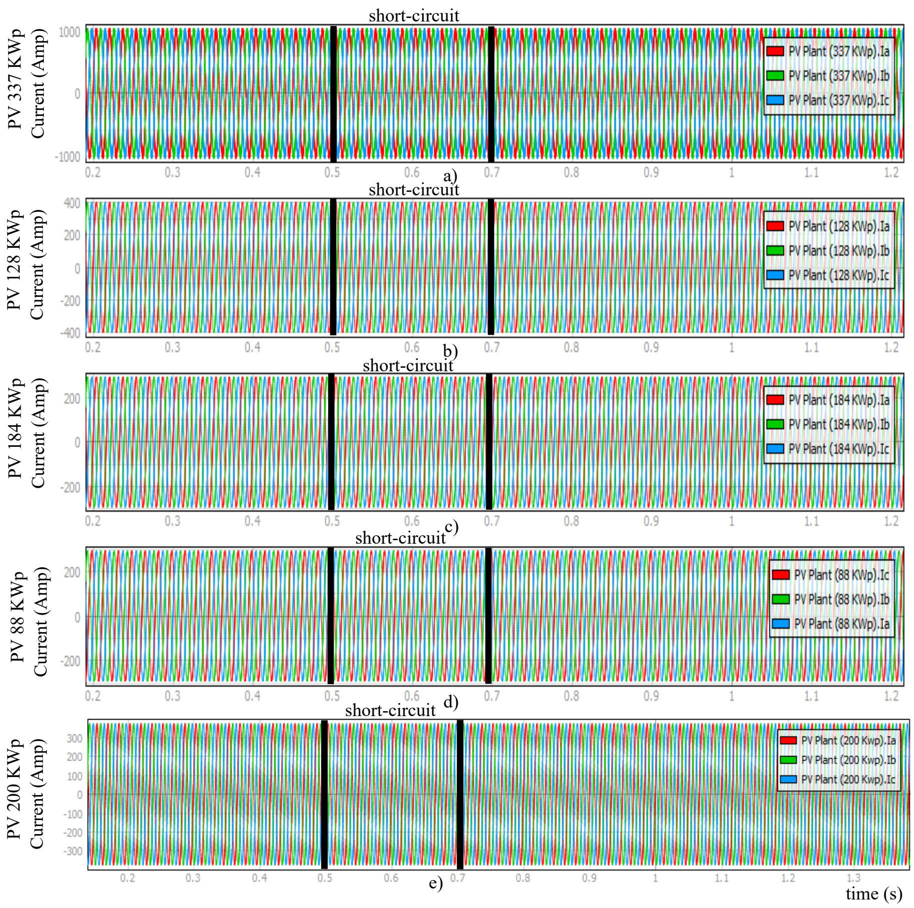

Figure 5.17 – Inverter behavior during a phase A to ground fault. a) PV 337 KWp - Grid following inverter current, b) PV 128 KWp - Grid following inverter current, c) PV 184 KWp - Grid following inverter current, d) PV 88 KWp - Grid following inverter current y e) PV 200 KWp - Grid following inverter current.

6 Conclusions and Future Works

6.1 Conclusions

In this document, the modeling of the CAMPUSGRID microgrid was carried out with photovoltaic generation sources, gas generation, and simplified and detailed models of the BESS system, also including all the necessary details of the model and control. Likewise, an analysis of the dynamic behavior of the microgrid in six scenarios was carried out.

From the studies presented, the following can be concluded:

- We can conclude that the microgrid using both simplified and detailed models of the BESS system, show almost the same behavior, in the transition to islanded mode. In both cases, the microgrid presents operational flexibility, capable of keeping the system stable during the transition, showing the correct performance of the control structures.
- From scenario 5.2, we can conclude that the microgrid with the simplified and detailed models. Both manage to maintain stability in the re-synchronization with the utility grid.
- It was shown that in the simplified BESS model in an islanded microgrid, and the system is highly loaded, the model does not capture the behavior during and after the maximum load disturbance. Likewise, it was observed that the dynamics of the DC link of the complete model contribute to the instability, caused by the increase in the charging and discharging current of the DC link capacitor. In fact, the detailed BESS model loses its stability for certain load levels, while the simplified model remains stable.
- From scenario 5.5 it was shown that it is important to have at least one grid forming IBR in the system, to maintain the stability of the microgrid in islanded mode.
- From scenario 5.6 it was shown that the fault currents in the IBR have a very small short-circuit contribution between 1.1 to 1.2 p.u of their nominal currents, this brings problems to traditional protection systems, becoming unreliable against the IBR. Likewise, in the case of having a secondary grid in delta, it is important to have a ZIGZAG transformer to have a reference to ground, to be able to determine the short-circuit currents of the IBR generation sources, and to be able to detect faults.

6.2 Future Works

- Implement isolation detection algorithms in the time domain simulations, to make the analysis of the transition of the microgrid operating modes more realistic.
- Study and implementation of microgrid protection structures.
- Fault analysis in inverters operating the microgrid in isolated mode.

6.3 Published Articles

- Analise Dinamica da CAMPUSGRID: Microrrede na Universidade Estadual de Campinas (UNICAMP) congreso: IX Simpósio Brasileiro de Sistemas Elétricos (SBSE 2022)

Bibliography

AHMED, M. et al. Stability and control aspects of microgrid architectures–a comprehensive review. *IEEE Access*, v. 8, p. 144730–144766, 2020. Cited 2 times on pages 25 and 27.

ALABOUDY, A. K. et al. Microgrid stability characterization subsequent to fault-triggered islanding incidents. *IEEE transactions on power delivery*, v. 27, n. 2, p. 658–669, 2012. Cited 2 times on pages 33 and 43.

ANDRADE, F. et al. Study of large-signal stability of an inverter-based generator using a lyapunov function. In: *IECON 2014 - 40th Annual Conference of the IEEE Industrial Electronics Society*. [S.l.: s.n.], 2014. p. 1840–1846. Cited on page 35.

BIDRAM, A.; DAVOUDI, A. Hierarchical structure of microgrids control system. *IEEE Transactions on Smart Grid*, v. 3, n. 4, p. 1963–1976, 2012. Cited on page 29.

BUSO, S.; MATTAVELLI, P. Digital control in power electronics. *Synthesis Lectures on Power Electronics*, Morgan & Claypool Publishers, v. 5, n. 1, p. 1–229, 2015. Cited 3 times on pages 12, 99, and 101.

CESPEDES, M.; XING, L.; SUN, J. Constant-power load system stabilization by passive damping. *IEEE Transactions on Power Electronics*, IEEE, v. 26, n. 7, p. 1832–1836, 2011. Cited on page 18.

DU, W. et al. Comparison of electromagnetic transient and phasor-based simulation for the stability of grid-forming-inverter-based microgrids. In: IEEE. *2021 IEEE Power & Energy Society Innovative Smart Grid Technologies Conference (ISGT)*. [S.l.], 2021. p. 1–5. Cited on page 20.

DU, W. et al. Modeling of grid-forming and grid-following inverters for dynamic simulation of large-scale distribution systems. *IEEE Transactions on Power Delivery*, IEEE, v. 36, n. 4, p. 2035–2045, 2020. Cited on page 20.

FARHANGI, H.; JOOS, G. Microgrid elements and modeling. In: ______. *Microgrid Planning and Design: A Concise Guide*. [S.l.: s.n.], 2019. p. 37–55. Cited 5 times on pages 10, 25, 47, 48, and 53.

FARROKHABADI, M. et al. Microgrid stability definitions, analysis, and examples. *IEEE Transactions on Power Systems*, v. 35, n. 1, p. 13–29, 2020. Cited 11 times on pages 10, 24, 29, 30, 31, 32, 33, 34, 35, 37, and 58.

FARROKHABADI, M. et al. Battery energy storage system models for microgrid stability analysis and dynamic simulation. *IEEE Transactions on Power Systems*, IEEE, v. 33, n. 2, p. 2301–2312, 2017. Cited on page 20.

GARCéS, A. On the convergence of newton's method in power flow studies for dc microgrids. *IEEE Transactions on Power Systems*, v. 33, n. 5, p. 5770–5777, 2018. Cited on page 25.

GKOUNTARAS, A. *Modeling techniques and control strategies for inverter dominated microgrids*. [S.l.]: Universitätsverlag der TU Berlin, 2017. v. 2. Cited 2 times on pages 10 and 41.

GONZALEZ-LONGATT, F. M.; RUEDA, J. L. *PowerFactory applications for power system analysis*. [S.l.]: Springer, 2014. Cited on page 23.

GUERRERO, J. M. et al. Hierarchical control of droop-controlled ac and dc microgrids—a general approach toward standardization. *IEEE Transactions on Industrial Electronics*, v. 58, n. 1, p. 158–172, 2011. Cited on page 29.

HE, J. et al. Investigation and active damping of multiple resonances in a parallel-inverter-based microgrid. *IEEE Transactions on Power Electronics*, v. 28, n. 1, p. 234–246, 2013. Cited on page 33.

HIRSCH, A.; PARAG, Y.; GUERRERO, J. Microgrids: A review of technologies, key drivers, and outstanding issues. *Renewable and sustainable Energy reviews*, Elsevier, v. 90, p. 402–411, 2018. Cited on page 18.

IEEE Standard for Interconnection and Interoperability of Distributed Energy Resources with Associated Electric Power Systems Interfaces. *IEEE Std 1547-2018 (Revision of IEEE Std 1547-2003)*, p. 1–138, 2018. Cited 5 times on pages 13, 27, 28, 73, and 74.

KABALAN, M.; SINGH, P.; NIEBUR, D. Nonlinear lyapunov stability analysis of seven models of a dc/ac droop controlled inverter connected to an infinite bus. *IEEE Transactions on Smart Grid*, v. 10, n. 1, p. 772–781, 2019. Cited on page 35.

KARIMI, H.; NIKKHAJOEI, H.; IRAVANI, R. Control of an electronically-coupled distributed resource unit subsequent to an islanding event. *IEEE Transactions on Power Delivery*, IEEE, v. 23, n. 1, p. 493–501, 2007. Cited on page 18.

KARIMI, H.; YAZDANI, A.; IRAVANI, R. Negative-sequence current injection for fast islanding detection of a distributed resource unit. *IEEE Transactions on power electronics*, IEEE, v. 23, n. 1, p. 298–307, 2008. Cited on page 18.

KATIRAEI, F.; IRAVANI, M. R.; LEHN, P. W. Micro-grid autonomous operation during and subsequent to islanding process. *IEEE Transactions on power delivery*, IEEE, v. 20, n. 1, p. 248–257, 2005. Cited on page 18.

KHAYAT, Y. et al. On the secondary control architectures of ac microgrids: An overview. *IEEE Transactions on Power Electronics*, v. 35, n. 6, p. 6482–6500, 2020. Cited on page 30.

KUNDUR, P. S. Power system stability. In: *Power System Stability and Control*. [S.l.]: CRC Press, 2017. p. 8–1. Cited 2 times on pages 41 and 42.

LASSETER, B. Microgrids [distributed power generation]. In: IEEE. *2001 IEEE power engineering society winter meeting. Conference proceedings (Cat. No. 01CH37194)*. [S.l.], 2001. v. 1, p. 146–149. Cited on page 18.

LI, C. et al. Power flow analysis for low-voltage ac and dc microgrids considering droop control and virtual impedance. *IEEE Transactions on Smart Grid*, IEEE, v. 8, n. 6, p. 2754–2764, 2016. Cited on page 18.

LI, F. et al. Active dc bus signaling control method for coordinating multiple energy storage devices in dc microgrid. In: *2017 IEEE Second International Conference on DC Microgrids (ICDCM)*. [S.l.: s.n.], 2017. p. 221–226. Cited 2 times on pages 10 and 26.

LISERRE, M. et al. The smart transformer: Impact on the electric grid and technology challenges. *IEEE Industrial Electronics Magazine*, IEEE, v. 10, n. 2, p. 46–58, 2016. Cited on page 18.

LÓPEZ, J. C. et al. Objetivos e desafios do projeto de p&d merge: Microgrids for efficient, reliable and greener energy. *Simpósio Brasileiro de Sistemas Elétricos-SBSE*, v. 1, n. 1, 2020. Cited 2 times on pages 19 and 61.

MEEGAHAPOLA, L. *Microgrid Stability Definitions, Analysis, and Modeling (Technical Report PES-TR66)*. [S.l.], 2018. Cited 7 times on pages 24, 30, 31, 32, 33, 37, and 57.

MIRAFZAL, B.; ADIB, A. On grid-interactive smart inverters: Features and advancements. *IEEE Access*, v. 8, p. 160526–160536, 2020. Cited 3 times on pages 10, 44, and 45.

MOHAN, N.; UNDELAND, T. M.; ROBBINS, W. P. *Power electronics: converters, applications, and design*. [S.l.]: John wiley & sons, 2003. Cited on page 46.

NASR-AZADANI, E. et al. Stability analysis of unbalanced distribution systems with synchronous machine and dfig based distributed generators. *IEEE Transactions on Smart Grid*, IEEE, v. 5, n. 5, p. 2326–2338, 2014. Cited 2 times on pages 19 and 33.

OLIVARES, D. E. et al. Trends in microgrid control. *IEEE Transactions on smart grid*, IEEE, v. 5, n. 4, p. 1905–1919, 2014. Cited on page 18.

OLIVARES, D. E. et al. Trends in microgrid control. *IEEE Transactions on Smart Grid*, v. 5, n. 4, p. 1905–1919, 2014. Cited 3 times on pages 28, 29, and 30.

PODLESAK, T. et al. Auto-tuning for military microgrids. In: *2019 IEEE Energy Conversion Congress and Exposition (ECCE)*. [S.l.: s.n.], 2019. p. 6270–6277. Cited on page 43.

PSCAD. *pscad*. Pscad Documentation. <https://www.pscad.com/>. Acessado em 10/05/2022. Cited on page 35.

QUADROS, R. et al. Implementation of microgrid on the university campus of unicamp brazil: Case study. *Journal of Electronics and Advanced Electrical Engineering*, v. 1, n. 2, p. 21–25, 2021. Cited 4 times on pages 11, 61, 62, and 63.

RANJAN, R. et al. Power flow solution of three-phase unbalanced radial distribution network. *Electric Power Components and Systems*, Taylor & Francis, v. 32, n. 4, p. 421–433, 2004. Cited 5 times on pages 10, 37, 38, 39, and 40.

ROCABERT, J. et al. Control of power converters in ac microgrids. *IEEE Transactions on Power Electronics*, v. 27, n. 11, p. 4734–4749, 2012. Cited 2 times on pages 28 and 48.

RODRIGUEZ, P. et al. Decoupled double synchronous reference frame pll for power converters control. *IEEE Transactions on Power Electronics*, v. 22, n. 2, p. 584–592, 2007. Cited 3 times on pages 10, 52, and 53.

RTDS Technologies. *RTDS Technologies Documentation*. Hardware–in–the–loop testing for renewables. <https://www.rtds.com/>. Acessado em 10/05/2022. Cited on page 35.

SALEH, S. A.; RAHMAN, M. A. Modeling of power inverters. In: ______. *An Introduction to Wavelet Modulated Inverters*. [S.l.: s.n.], 2011. p. 41–63. Cited on page 46.

SAO, C.; LEHN, P. Autonomous load sharing of voltage source converters. *IEEE Transactions on Power Delivery*, v. 20, n. 2, p. 1009–1016, 2005. Cited on page 32.

SINGHAL, A.; VU, T. L.; DU, W. Consensus control for coordinating grid-forming and grid-following inverters in microgrids. *IEEE Transactions on Smart Grid*, IEEE, 2022. Cited on page 20.

SOULTANIS, N. L.; PAPATHANASIOU, S. A.; HATZIARGYRIOU, N. D. A stability algorithm for the dynamic analysis of inverter dominated unbalanced lv microgrids. *IEEE Transactions on Power Systems*, IEEE, v. 22, n. 1, p. 294–304, 2007. Cited on page 19.

TALAPUR, G. G. et al. A reliable microgrid with seamless transition between grid connected and islanded mode for residential community with enhanced power quality. *IEEE Transactions on Industry Applications*, v. 54, n. 5, p. 5246–5255, 2018. Cited on page 49.

TARRASÓ, A. et al. Synchronous power controller for distributed generation units. In: IEEE. *2019 IEEE Energy Conversion Congress and Exposition (ECCE)*. [S.l.], 2019. p. 4660–4664. Cited on page 19.

Typhoon HIL. *Typhoon HIL*. Typhoon HIL. <https://www.typhoon-hil.com/>. Acessado em 10/05/2022. Cited 8 times on pages 11, 22, 35, 57, 58, 59, 72, and 97.

Typhoon HIL Documentation. *Typhoon HIL Documentation*. IEEE DC4B Exciter. <https://www.typhoon-hil.com/documentation/typhoon-hil-software-manual/References/ieee_dc4b_exciter.html>. Acessado em 10/05/2022. Cited on page 42.

Typhoon HIL Documentation. *Typhoon HIL Documentation*. Three Phase Synchronous Machine. <https://www.typhoon-hil.com/documentation/typhoon-hil-software-manual/References/three_phase_wound_rotor_synchronous_machine.html>. Acessado em 10/05/2022. Cited on page 41.

UNAMUNO, E.; BARRENA, J. A. Hybrid ac/dc microgrids—part i: Review and classification of topologies. *Renewable and Sustainable Energy Reviews*, Elsevier, v. 52, p. 1251–1259, 2015. Cited 2 times on pages 10 and 26.

WANG, X.; BLAABJERG, F.; WU, W. Modeling and analysis of harmonic stability in an ac power-electronics-based power system. *IEEE transactions on power electronics*, IEEE, v. 29, n. 12, p. 6421–6432, 2014. Cited on page 33.

Appendices

A Renewable Energy Sources Data

A.1 Battery Energy Storage System

Table A.1 – Nominal Data and Storage System Control Parameters

Parameters	**data**	**Parameters**	**data**
Nominal power	1 MVA	Following I_d (K_p)	0.347
Nominal voltage	480 V	Following I_d (k_i)	347.22
DC link voltage	1000 V	Following I_q (k_d)	0.34
Frequency	60 Hz	Following I_q (k_i)	347.22
Switching frequency	10 kHz	Forming I_{dref} (K_p)	10
Filter-inductance	0.250 mH	Forming I_{dref} (k_i)	10
Resistor-inductance	$1e^{-6}$ Ω	Forming I_d (k_p)	0.83
Filter-capacitor	2.7 mF	Forming I_d (k_i)	833.33
Resistor-capacitor	$15e^{-3}$ Ω		

Table A.2 – BESS DC/DC Parameter

Parameters	**data**	**Parameters**	**data**
Battery type	Lithium - Ion	Nominal voltage	800 V
Capacity	1000 Ah	Initial SOC	80 %
Capacitor DC	20 mF	Carrier frequency	5 kHz
Voltage controller K_p	0.25	Voltage controller K_i	50
Upper saturation limit	1000	Lower saturation limit	0
Current controller K_p	0.005	Current controller K_i	10

A.2 Diesel Generator 250 KVA and 50 KVA

Table A.3 – Nominal Data and 250 KVA gas generator System Control Parameters

Parameters	**data**	**Parameters**	**data**
Nominal Power	250 KVA	Governor-Box time (T_1)	$1e^{-4}s$
Nominal Voltage	480 V	Governor-Box time (T_2)	$1e^{-6}s$
Frequency	60 Hz	Governor-Box time (T_3)	$0.5001s$
Exciter-Time constant	$2e^{-6}$	Governor-Actuator time (T_4)	$25e^{-3}s$
Governor-Actuator time (T_5)	$9e^{-4}s$	Governor-Actuator time (T_6)	$5.74e^{-3}s$
Engine time delay	$24e^{e-3}s$	Exciter K_p	0.025
Exciter k_i	0.007	Exciter gain K_a	1
Exciter time constant T_a	$2.0e^{-3}$	Exciter time constant T_e	$1.0e^{-8}$
Exciter gain K_e	1	feedback gain k_f	0.01
feedback time constant T_f	$2.0e^{-6}$		

Table A.4 – Nominal Data and 50 KVA gas generator System Control Parameters

Parameters	**data**	**Parameters**	**data**
Nominal Power	50 KVA	Governor-Box time (T_1)	$1e^{-4}s$
Nominal Voltage	480 V	Governor-Box time (T_2)	$1e^{-6}s$
Frequency	60 Hz	Governor-Box time (T_3)	$0.5001s$
Exciter-Time constant	$2e^{-6}$	Governor-Actuator time (T_4)	$25e^{-3}s$
Governor-Actuator time (T_5)	$9e^{-4}s$	Governor-Actuator time (T_6)	$5.74e^{-3}s$
Engine time delay	$24e^{e-3}s$	Exciter K_p	0.025
Exciter k_i	0.007	Exciter gain K_a	1
Exciter time constant T_a	$2.0e^{-3}$	Exciter time constant T_e	$1.0e^{-8}$
Exciter gain K_e	1	feedback gain k_f	0.01
feedback time constant T_f	$2.0e^{-6}$		

A.3 Photovoltaic System

Table A.5 – Nominal Data and 337 KWp Photovoltaic System Control Parameters

Parameters	**data**	**Parameters**	**data**
Nominal Power	337 KWp	voltage V_{kp}	15
Nominal voltage	220 V	voltage V_{ki}	3
Frequency	60 Hz	Current I_{kp}	3
Switching frequency	10 kHz	Current I_{ki}	30
DC Nominal voltage	1000 V	Filter-inductor	$79.8e^{-6}$H
Pv efficiency	20%	Filter-capacitor	$2.7085e^{-3}$F
PV plant area	1666.66 m^2		

Table A.6 – Nominal Data and 88 KWp Photovoltaic System Control Parameters

Parameters	**data**	**Parameters**	**data**
Nominal Power	88 KWp	voltage V_{kp}	15
Nominal voltage	220 V	voltage V_{ki}	3
Frequency	60 Hz	Current I_{kp}	3
Switching frequency	10 kHz	Current I_{ki}	30
DC Nominal voltage	1000 V	Filter-inductor	$3e^{-3}$H
Pv efficiency	20%	Filter-capacitor	$20e^{-6}$F
PV plant area	440 m^2		

Table A.7 – Nominal Data and 128 KWp Photovoltaic System Control Parameters

Parameters	**data**	**Parameters**	**data**
Nominal Power	128 KWp	voltage V_{kp}	15
Nominal voltage	220 V	voltage V_{ki}	3
Frequency	60 Hz	Current I_{kp}	3
Switching frequency	10 kHz	Current I_{ki}	30
DC Nominal voltage	1000 V	Filter-inductor	$3e^{-3}$H
Pv efficiency	20%	Filter-capacitor	$20e^{-6}$F
PV plant area	640 m^2	Filter-inductor grid	$4e^{-6}$H

Table A.8 – Nominal Data and 200 KWp Photovoltaic System Control Parameters

Parameters	data	Parameters	data
Nominal Power	200 KWp	voltage V_{kp}	15
Nominal voltage	220 V	voltage V_{ki}	3
Frequency	60 Hz	Current I_{kp}	3
Switching frequency	10 kHz	Current I_{ki}	30
DC Nominal voltage	1000 V	Filter-inductor	$79.8e^{-6}$H
Pv efficiency	20%	Filter-capacitor	$2.71e^{-3}$F
PV plant area	1000 m^2	Filter-inductor grid	$9.6e^{-6}$H

A.4 Typhoon HIL Control Center

Typhoon HIL Control Center is one of the advanced methods in the rapidly growing field of ultra-high-fidelity Hardware-in-the-Loop (HIL) controller testing for power electronics, microgrids, and distribution networks (Typhoon HIL, Typhoon HIL). Typhoon provides tools for modeling, simulation, and testing. In addition, (Typhoon HIL, Typhoon HIL) provides a detailed description of all the features available in the Typhoon HIL software toolk it, including the Schematic Editor, which provides tools for model development, and HIL SCADA, which allows you to interact with the simulation in real-time, from the model that was created in the Schematic Editor. Figure A.1 shows the Typhoon HIL Control Center Software initialization window.

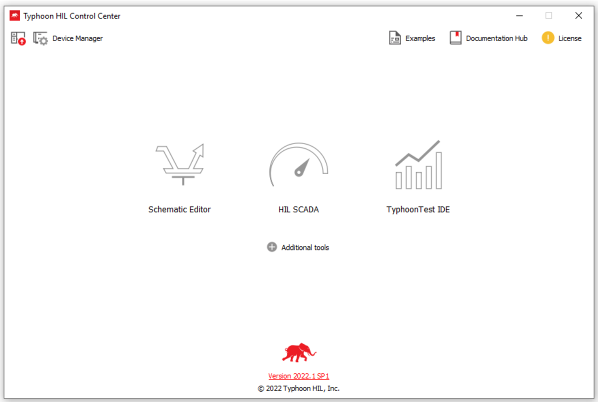

Figure A.1 – Typhoon HIL Control Center

A.4.1 Schematic Editor

The Typhoon HIL schematic editor is designed to acquire a number of power electronics components and blocks that can be used as building blocks to model power electronics systems in real-time. Schematic Editor allows you to create high-fidelity models of the power stage for your real-time simulations. For detailed information about the schematic editor library, see Typhoon documentation. The Scheme Editor interface is shown in Figure A.2.

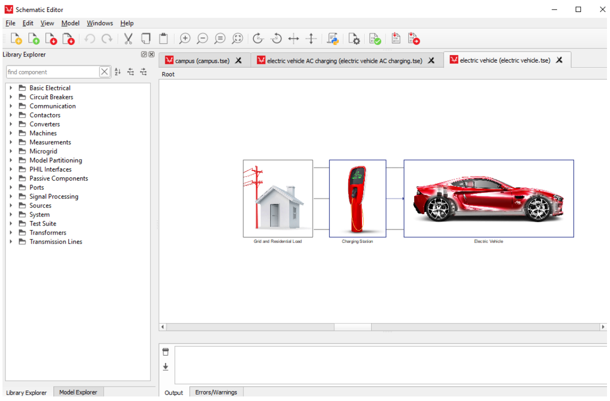

Figure A.2 – Typhoon HIL Scheme Editor

A.4.2 HIL SCADA

Typhoon HIL SCADA is a simple and easy-to-use graphical environment that allows you to create your own specific interface with your real-time model. With the HIL SCADA widgets, combined with the power of Python macro and expression scripts, you can control and observe not only your HIL simulation but also your own external device(s). The HIL SCADA application has two basic functions: to download simulation models to the HIL platform and to control the emulation process, parameters and outputs. Figure A.3 shows the graphical interface of the HIL SCADA.

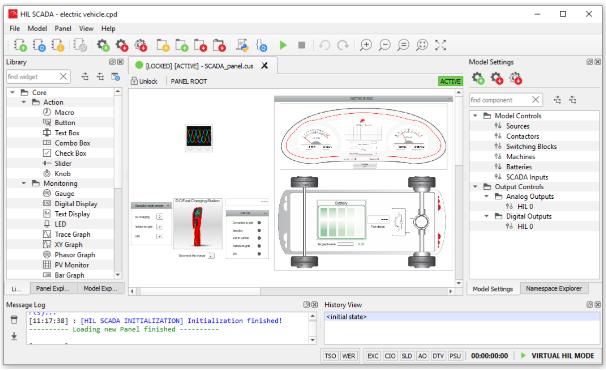

Figure A.3 – Typhoon HIL SCADA

A.5 Clark and Park transforms

A.5.1 Clarke's transformation

The α β transformation, also known as the Clarke transformation, is a very useful tool for the analysis and modeling of three-phase electrical systems. This tool reduces the order of the mathematical model from three to two stationary dimensions when the three-phase system is balanced. There are three modes for this transformation, Clarke's Variant Power - Original, Variant Power - Uniform, and Invariant Power (BUSO; MATTAVELLI, 2015). To explain its operation we can consider a three-dimensional vector shown in Figure A.4 that can represent any electrical variable of the system, voltage, or current.

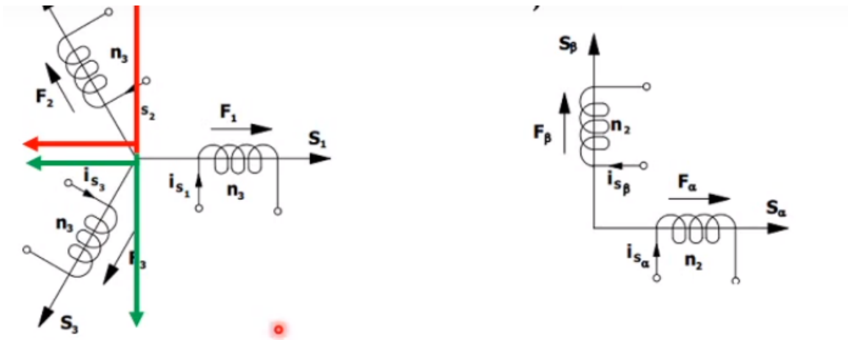

Figure A.4 – Graphical representation of the $T_{\alpha\beta}$ coordinate transformation (BUSO; MATTAVELLI, 2015)

Figure A.4 shows a three-phase system in the three axes offset by 120° (S_1, S_2, S_3) with their respective coils (n_1, n_2, n_3). Likewise, these produce a force in the three axes (F_a, F_b, F_c) when current (i_a, i_b, i_c) passes through the coils. In this context applying the α β transform, and considering that S_1 and S_α are in phase. The components F_b and F_c are decomposed on the xy axes, obtaining eq. A.1 and A.2.

$$F_\alpha = F_a + F_b.cos\frac{2\pi}{3} + F_c.cos\frac{4\pi}{3} \tag{A.1}$$

$$F_\beta = 0 + F_b.sen\frac{2\pi}{3} + F_c.sen\frac{4\pi}{3} \tag{A.2}$$

ordering in matrix form we get eq. A.3

$$\begin{bmatrix} F_\alpha \\ F_\beta \end{bmatrix} = \begin{bmatrix} 1 & -\frac{1}{2} & -\frac{1}{2} \\ 0 & \frac{\sqrt{3}}{2} & -\frac{\sqrt{3}}{2} \end{bmatrix} \cdot \begin{bmatrix} F_a \\ F_b \\ F_c \end{bmatrix} \tag{A.3}$$

the forces in the $\alpha\beta$ and abc axes are produced by the current passing through the winding as described in eq.A.4. Likewise, eq.A.5 describes the relationship between the currents $\alpha\beta$ and abc.

$$\begin{bmatrix} F_\alpha \\ F_\beta \end{bmatrix} = N_2. \begin{bmatrix} i_\alpha \\ i_\beta \end{bmatrix} \; e \; \begin{bmatrix} F_a \\ F_b \\ F_c \end{bmatrix} = N_3. \begin{bmatrix} i_a \\ i_b \\ i_c \end{bmatrix} \tag{A.4}$$

$$\begin{bmatrix} i_\alpha \\ i_\beta \end{bmatrix} = \frac{N_3}{N_2} . \begin{bmatrix} 1 & -\frac{1}{2} & -\frac{1}{2} \\ 0 & \frac{\sqrt{3}}{2} & -\frac{\sqrt{3}}{2} \end{bmatrix} . \begin{bmatrix} i_a \\ i_b \\ i_c \end{bmatrix} \tag{A.5}$$

for eq. A.5 to be invertible, the transformation matrix must be square, that is why the current i_0 was proposed and we obtain eq. A.6. However, to determine the Clark transformation matrix eq. A.7, the variables k and $\frac{N_2}{N_3}$ must be found.

$$\begin{bmatrix} i_0 \\ i_\alpha \\ i_\beta \end{bmatrix} = \begin{bmatrix} T_{\alpha\beta} \end{bmatrix} . \begin{bmatrix} i_a \\ i_b \\ i_c \end{bmatrix} \tag{A.6}$$

$$\begin{bmatrix} T_{0\alpha\beta} \end{bmatrix} = \frac{N_3}{N_2} . \begin{bmatrix} k & k & k \\ 1 & -\frac{1}{2} & -\frac{1}{2} \\ 0 & \frac{\sqrt{3}}{2} & -\frac{\sqrt{3}}{2} \end{bmatrix} \tag{A.7}$$

applying the identity property of matrices I, we obtain the values of k and $\frac{N_2}{N_3}$ shown in eq.A.9 and A.10.

$$\begin{bmatrix} T_{0\alpha\beta} \end{bmatrix} . \begin{bmatrix} T_{0\alpha\beta} \end{bmatrix}^T = I \tag{A.8}$$

where are they obtained

$$3(\frac{N_3}{N_2})^2 . k^2 = 1 \Rightarrow k = \frac{1}{\sqrt{2}} \tag{A.9}$$

$$\frac{3}{2} . (\frac{N_3}{N_2})^2 = 1 \Rightarrow \frac{N_3}{N_2} = \sqrt{\frac{2}{3}} \tag{A.10}$$

this coordinate transformation is known as the Clarke transformation

Power invariant eq.A.11

$$\begin{bmatrix} T_{0\alpha\beta} \end{bmatrix} = \sqrt{\frac{2}{3}} . \begin{bmatrix} \frac{1}{\sqrt{2}} & \frac{1}{\sqrt{2}} & \frac{1}{\sqrt{2}} \\ 1 & -\frac{1}{2} & -\frac{1}{2} \\ 0 & \frac{\sqrt{3}}{2} & -\frac{\sqrt{3}}{2} \end{bmatrix} \tag{A.11}$$

Amplitude invariant eq. A.12

$$\begin{bmatrix} T_{0\alpha\beta} \end{bmatrix} = \frac{2}{3} . \begin{bmatrix} \frac{1}{2} & \frac{1}{2} & \frac{1}{2} \\ 1 & -\frac{1}{2} & -\frac{1}{2} \\ 0 & \frac{\sqrt{3}}{2} & -\frac{\sqrt{3}}{2} \end{bmatrix} \tag{A.12}$$

A.5.2 Park's transformation

The Park transform has been widely used in the study of the dynamics of synchronous machines. Performs a transformation from a stationary reference frame where the currents are sinusoidal to a rotating reference frame in continuous values (BUSO; MATTAVELLI, 2015), shown in Figure A.5. This makes it extremely easy for the controller to control the machine or inverter via a PI or PID control loop.

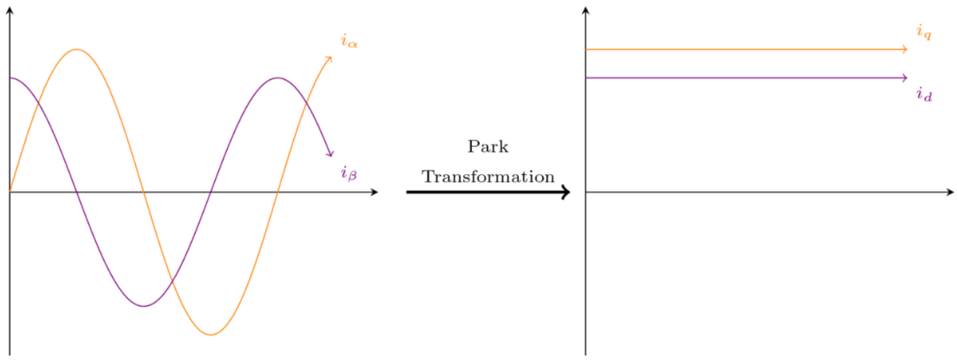

Figure A.5 – Park transformation

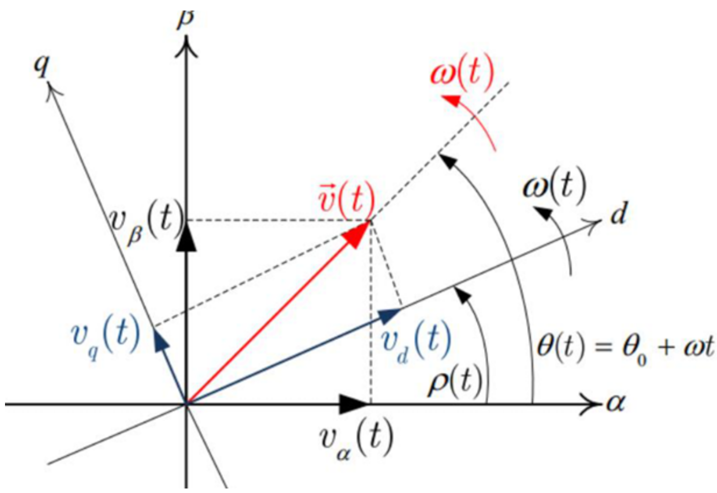

Figure A.6 – Vector diagrams for Park's transformation.

The Park transform defines a new set of reference axes, called d and q, shown in Figure A.6. These axes rotate about the static reference frame $\alpha\beta$ at a constant angular reference ω.

We can now show the mathematical formulation of Park's transformation. Considering Figure A.6, it is easy to demonstrate that this is given by the following matrix A.13:

$$\begin{bmatrix} v_d \\ v_q \end{bmatrix} = \begin{bmatrix} cos\rho & sen\rho \\ -sen\rho & cos\rho \end{bmatrix} \cdot \begin{bmatrix} v_\alpha \\ v_\beta \end{bmatrix} \tag{A.13}$$

where $\rho = \omega t$, so that the matrix of eq. A.13 is invertible, a current io is inserted and shown eq. A.14.

$$\begin{bmatrix} i_0 \\ i_d \\ i_q \end{bmatrix} = \begin{bmatrix} 1 & 0 & 0 \\ 0 & cos\rho & sen\rho \\ 0 & -sen\rho & cos\rho \end{bmatrix} . \begin{bmatrix} i_0 \\ i_\alpha \\ i_\beta \end{bmatrix} \tag{A.14}$$

substituting the current matrix α, β in equation A.14, we get:

$$\begin{bmatrix} i_0 \\ i_d \\ i_q \end{bmatrix} = \frac{2}{3}. \begin{bmatrix} \frac{1}{2} & \frac{1}{2} & \frac{1}{2} \\ cos\rho & -\frac{1}{2}cos\rho + \frac{\sqrt{3}}{2}sen\rho & -\frac{1}{2}cos\rho - \frac{\sqrt{3}}{2}sen\rho \\ -sen\rho & \frac{1}{2}cos\rho + \frac{\sqrt{3}}{2}sen\rho & \frac{1}{2}cos\rho - \frac{\sqrt{3}}{2}sen\rho \end{bmatrix} . \begin{bmatrix} i_a \\ i_b \\ i_c \end{bmatrix} \tag{A.15}$$

However, in practice it is preferable to perform two transformations ($abc \Rightarrow \alpha\beta 0$ and $\alpha\beta 0 \Rightarrow dq0$), due to the lower computational effort, this is because in this case only two trigonometric functions are calculated.